BIONICS & SPACE SYSTEM DESIGN (AO/1-4469/03/NL/SFe)
CASE STUDY 2 – Asteroid Micro-Penetrator with Biomimetic Drill

SURREY
SPACE CENTRE

ESA STUDY CONTRACT REPORT

No ESA Study Contract Report will be accepted unless this sheet is inserted at the beginning of each volume of the Report.

ESA CONTRACT No **AO/1-4469/03/NL/SFe**	SUBJECT **BIONICS & SPACE SYSTEMS DESIGN CASE STUDY 2 – ASTEROID MICRO-PENETRATOR WITH BIOMIMETIC DRILL**		CONTRACTOR **UNIVERSITY OF SURREY**
* ESA CR( )No	* STAR CODE	No of volumes 1 This is Volume No 1	CONTRACTOR'S REFERENCE

ABSTRACT:

This document is Case Study 2 Technical Report for the Bionics & Space Systems Design study jointly authored by the University of Surrey (prime), University of Bath, and EADS Astrium.

This case study presents a biomimetic drill based on working mechanism of wood wasp ovipositor for sampling planetary subsurface material. The ovipositor drill concept represents a novel approach of reciprocating drilling and can be used as a payload for a generic space mission. It also has technology transfer applications within the terrestrial environment. To provide a complete mission design, an asteroid micro-penetrator is considered as the mission scenario and design platform. This study outlines a micro-penetrator concept with a mass target of 5-10 kg that is suited for planetary deployment to asteroids and in-situ investigation of their chemical (astrobiologically relevant signatures) and physical properties. Such a biomimetic drill/microprobe may be deployed for the exploration of terrestrial-type planets and other small bodies of the solar system with the minimum of modifications.

This project indicates some of the enhanced utility that may be incorporated into engineered systems inspired from biological systems. Such enhanced utility is critical for space missions where premium is placed on mass, volume, power and data handling which drive the mission design. Biological systems are similarly constrained making biomimetic technology uniquely suited as a model of miniaturised systems.

The work described in this report was done under ESA contract. Responsibility for the contents resides in the author or organisation that prepared it.

Names of authors: Dr Alex Ellery, Dr Yang Gao

** NAME OF ESA STUDY MANAGER Dr Mark Ayre, Dr Carol Menon DIV: Advanced Concepts Team DIRECTORATE:	** ESA BUDGET HEADING

This page is left intentionally blank

BIONICS & SPACE SYSTEMS DESIGN AO/1-4469/03/NL/SFe

Case Study 2
Asteroid Micro-Penetrator with Biomimetic Drill

Version: 1.0

Date: 1 June 2005

Prepared by:

Dr. Alex Ellery
Surrey Space Centre
School of Electronics and Physical Sciences
University of Surrey
Guildford
Surrey GU2 7XH
UK
Tel: +44 1483 683882
Fax: +44 1483 689503
Email: a.ellery@surrey.ac.uk

Dr. Yang Gao
Surrey Space Centre
School of Electronics and Physical Sciences
University of Surrey
Guildford
Surrey GU2 7XH
UK
Tel: +44 1483 686001
Fax: +44 1483 689503
Email: yang.gao@surrey.ac.uk

This page is left intentionally blank

List of Contributing Authors

Dr. Alex Ellery Surrey Space Centre School of Electronics and Physical Sciences University of Surrey Guildford Surrey GU2 7XH, UK Tel: +44 1483 683882 Fax: +44 1483 689503 Email: a.ellery@surrey.ac.uk	Dr. Yang Gao Surrey Space Centre School of Electronics and Physical Sciences University of Surrey Guildford Surrey GU2 7XH, UK Tel: +44 1483 686001 Fax: +44 1483 689503 Email: yang.gao@surrey.ac.uk
Professor Julian Vincent Centre for Biomimetic and Natural Technologies Department of Mechanical Engineering The University of Bath BA2 7AY, UK Tel: +44 1225 386596 Fax: +44 1225 386928 Email: j.f.v.vincent@bath.ac.uk	Mr. Steven Eckersley Mission Systems Department EADS Astrium Ltd. Gunnels Wood Road Stevenage Hertfordshire SG1 2AS, UK Tel: +44 1438 773301 Email: Steven.ECKERSLEY@astrium.eads.netMr
Mr. Gregory P. Scott Surrey Space Centre School of Electronics and Physical Sciences University of Surrey Guildford Surrey GU2 7XH, UK Tel: +44 1483 683418 Fax: +44 1483 689503 Email: g.scott@surrey.ac.uk	Mr. M. Jaddou Department of Mechanical Engineering The University of Bath BA2 7AY, UK Email: en1mj@bath.ac.uk

List of Applicable Documents

[AD1]	Invitation to Tender	IMT-CTM//SFe/2003.960
[AD2]	Bionics & Space System Design: Statement of Work (Appendix 1)	GSP-03/L27
[AD3]	Draft contract (Appendix 2)	AO/1-4469/03/NL/Sfe
[AD4]	Special Conditions of Tender (Appendix 3)	AO/1-4469/03/NL/Sfe
[AD5]	General Conditions of Tender for ESA Contracts	ESA/C/290 rev 5
[AD6]	Biomimicry – A Review	ESA pdf publication (Mark Ayre)
[AD7]	Bionics & Space Systems Design – Technical Note 1	ESA pdf publication (Mark Ayre)
[AD8]	Bionics & Space Systems Design – Technical Note 2	ESA pdf publication (Mark Ayre)
[AD9]	Bionics & Space Systems Design – Technical Note 3	ESA pdf publication (Mark Ayre)

List of Reference Documents

Allen, W. A., Mayfield, E. B. and Morrison, H. L., (1957) Dynamics of a Projectile Penetrating Sand, J. Appl. Phys. 28(3), 370-376.

Anderson, W. W., Ahrens, T. J., Gibson, A., Scott, R. and Suzuki, K., (1996) Emplacement of Penetrators into Planetary Surfaces, *J. Geophys. Res.*, 101(E9), 21137-21149

Anttila, M., (2004) "Concept study for the subsurface sampling system for the Pasteur payload of the ExoMars mission", *Proc. of ESA Workshop on Advanced Space Technologies for Robotics and Automation*, Noordwijk, Netherlands, 93-100

Bar-Cohen, Y., et. al. (2001), "Ultrasonic/sonic/drilling/coring (USDC) for planetary applications", *Proc. Of SPIE International Symposium on Smart Structures and Materials*, Newport, CA, USA, 4327-4355

Ball, A.J. and Lorenz, R.D., (1999) "Penetrometry of extraterrestrial surfaces: a historical overview", *Proc. of the International Workshop on Penetrometry in the Solar System*, Graz, Austria, 3-23.

Binzel, R. P., Bus, S. J., Burbine, T. H. and Sunshine, J. M. (1996) Spectral properties of near-Earth asteroids: Evidence for sources of ordinary chondrite meteorites, *Science*, 273, 946-948.

Britt, D. T., Yeomans D., Housen K., and Consolmagno, G. (2002) Asteroid Density, Porosity, and Structure, In *Asteroids III*, ed. William F. Bottke, Alberto Cellino, Paolo Paolicchi, and Richard P. Binzel, Univ. of Arizona Press, Tucson.

Byers, R. K., Yarrington, P. and Chabai, A. J., (1978) Dynamic penetration of soil media by slender projectiles, *Int. J. Engng. Sci.*, 16, 835-844

Dickert, F. L., Hayden, O., (1999), *Trends in analytical chemistry*, 18, 192-199

Dickinsheets, D., *et al* (2000) *J Raman Spectros*, 31, 633-635

Ellery, A., *et al.* (2003). Astrobiological instrumentation for Mars – the only way is down. *Int. J. Astrobiology*, 1(4): 365-380.

Forrestal, M. J. and Luk, V. K. (1992) Penetration into soil targets, *Int. J. Impact Engng*, 12, 427-444.

Heuze, F. E. (1989) An overview of projectile penetration into geological materials, with emphasis on rocks, in L. E. Schwer, N. J. Salamon and W. K. Liu (Eds), *Computational Techniques for Contact, Impact, Penetration and Perforation of Solids*, AMD, American Society of Mechanical Engineers, New York, 103, 275-308.

Hutt, L. D., Glavin, D. P., Bada, J. L. and Mathies, R. A. (1999) Microfabricated Capillary Electrophoresis Amino Acid Chirality Analyzer for Extraterrestrial Exploration, *Anal. Chem.*, 71, 4000-4006

Israel, E., et al (1997) *J Geophys Res* (*Planets*) 102, 28705-28716

Kawaguchi, J., Uesugi, T., Fujiwara, A., and Matsuo, H., (1996) "The MUSES-C, world's first sample and return mission from near earth asteroid: Nereus", *ACTA Astronautica*, 39(1-4), 15-23

Kochan, H., Hamacher, H., Richter, L., Hirschmann, L., Assanelli, S., Nadalini, R., Pinna, S., Gromov, V.V., Matrossov, S., Yudkin, E.N., Coste, P., Pillinger, C.T., Sims, M.R., and Ng, T.C., (1999) "The mobile penetrometer (Mole): a tool for planetary sub-surface investigations", *Proc. of the International Workshop on Penetrometry in the Solar System*, Graz, Austria, 213-243

Lognonne, P., Clevede, E., and Kanamori, H. (1998) Computation of seismograms and atmospheric oscillations by normal-mode summation for a spherical Earth model with realistic atmosphere. *Geophys. J. Int.*, 388-406

Lorenz, R.D. and Ball, A.J. (1999) "Review of impact penetration tests and theories", *Proc. of the International Workshop on Penetrometry in the Solar System*, Graz, Austria, 25-39

Lorenz, R.D., Hathi, B., Leese, M.R., Garry, J.R.C., and Zarnecki, J.C., (1999) "The Huygens SSP penetrometer: an update", *Proc. of the International Workshop on Penetrometry in the Solar System*, Graz, Austria, 99-108

Lupishko, D.F., and Martino, M. Di, (1998) Physical properties of near-Earth asteroids, *Planet. Space Sci.*, 46, 47-74

McSween, H. Y. (1999) Meteorites and Their Parent Planets, Cambridge University Press

Menichella, M., Paolicchi, P. and Farinella, P. (1996) The mainbelt as a source of near-Earth asteroids, *Earth, Moon and Plane*, 72, 133-149

Merchant, M. E. (1945) *J. appl. Phys.* 16, 267(a) and 318(b)

Mizutani, H., Fujimura, A., Hayakawa, M., Tanaka, S., and Shiraishi, H., (1999) "Lunar-A penetrator: its science and instruments", *Proc. of the International Workshop on Penetrometry in the Solar System*, Graz, Austria, 125-13

Morrison, D. (ed.) (1992) Report of the NASA International Near-Earth-Object Detection Workshop, Jan. 25

Murphy, J. P., Reynolds, R. T., Blanchard, M. B. and Clanton, U. S. (1981) Surface penetrators for planetary exploration: science rationale and development program, *NASA Technical Memorandum 81251*, 54 pages

Piispanen, V. (1948) *J. appl. Phys.* 19, 876

Rabinowitz, D. L., Bowell, E., Shoemaker, E. and Muinonen, K. (1994) The population of Earth-crossing asteroids, In *Hazard Due to Comets and Asteroids*, ed. T. Gehrels, Univ. of Arizona Press, Tucson, 185-312

Skelley, A. M., Scherer, J. R., Aubrey, A. D., Grover, W. H., Ivester, R. H. C., Ehrenfreund, P., Grunthaner, F. J., Bada, J. L., Mathies, R. A., (2005), "Development and evaluation of a microdevice for amino acid biomarker detection and analysis on Mars", *PNAS*, 102(4), 1041-1046

Smrekar, S., Catling, D., Lorenz, R., Magalhães, J., Moersch, J., Morgan, P., Murray, B., Presley, M., Yen, A., Zent, A., Blaney, D., (1999) "Deep Space 2: The Mars Microprobe Mission", *J. Geophys. Res.*, 104(E11), 27013-27030

Simmons, G. J., (1977) Surface penetrators – a promising new type of planetary lander, *J. British Interplanetary Society*, 30, 243-256

Sims, M. R., Cullen, D. C., Bannister, N. P., Grant, W. D., and Jones, R., (2003), "A life marker chip for the specific molecular identification of life experiment", *Proc. III European Workshop on Exo-Astrobiology*, 293-294

Surkov, Yu. A., Kremnev, R. S., (1998) Mars-96 Mission: Mars exploration with the use of penetrators, *Planet. Space Sci.,* 46(11/12), 1689-1696

Thiel, M., Stocker, J., Rohe, C., Hillenmaier, O., Komle, N.I., and Kargl, G., (1999) "The Rosetta lander anchoring harpoon: subsystem and scientific instrument", *Proc. of the International Workshop on Penetrometry in the Solar System*, Graz, Austria, 137-150

Vincent, J. F. V. and Marcus, J. K. (1995), The mechanism of drilling by wood wasp ovipositors, *Biomimetics*, 3(4), 1995

Yew, C. H., and Stirbis, P. P. (1978) Penetration of projectile into terrestrial target, *J. Eng. Mech. Am. Soc. Civ. Engrs.*, 104(EM2), 273-286

Young, C. W. (1972) Empirical equations for predicting penetration performance in layered Earth materials for complex penetrator configurations, *Sandia Laboratories Report SC-DR-72-0523*

Young, C. W. (1997) Penetration equations, *Sandia Laboratories Report SA-ND-97-2426*

List of Figures

List of Tables

Table of Contents

I.   INTRODUCTION

1.   CONVENTIONAL SPACE DRILLS

Growing interest in extraterrestrial subsurface exploration has prompted an examination of advanced penetration and drilling technologies to sample geophysical data. Various penetration and drilling methods for autonomous sample acquisition has been attempted in missions to celestial bodies such as Mars, Moon, comets, and asteroids. Appendix A provides a summary of previous and forthcoming space missions involving automated penetration, drilling and sampling activities.

The drill with sampler is a commonly seen instrument equipped within landers and penetrators. It helps to drill deeper into extraterrestrial subsurface, take the samples, and thereafter perform further *in situ* experiments. Table 1 gives detailed information of the space drills appeared in Appendix A. They provide a reference model for the biomimetic drill in this case study.

Based on the type of force applied, drilling can be classified as follows:

- Shaped charges with metal liners eject a jet of molten metal to create a borehole - this method eliminates contextual data and physically/chemically corrupts the environment.

- Non-traditional drilling using power source of laser, electron beam, or microwave, etc - this method requires high power that is a scarce resource on outer space.

- Melting tip drilling - this method requires high powers and corrupts the environment by forming a glass casing. This type of drilling is eminently suitable for penetrating into ice such as the comet surfaces, Martian polar caps or European ice shell.

- Rotary drilling - This is the most common terrestrial approach to sub-surface penetration. It is an extremely versatile method capable of penetrating cohesive and non-cohesive soils and rock. It requires two motors (or a linked gearing single motor) to provide rotary action and vertical thrust. Terrestrial systems use extensive land support structures of high mass, though this can be dispensed with for modest depths. Rotary drilling suffers from bit dulling/breaking, bit jamming, high axial forces at drill initiation, the potential for drill walk and high power requirements. The Rosetta Lander will use a rotary coring tool (i.e. SD2) based on a helical auger to extract samples from 25 cm depth of ice. The 0.9 W electric rotary drill in DS2 microprobe operating at 10 rpm was to drill up to 1 cm within a 6-minute extraction cycle to extract 100 mg soil for a 160 ml ceramic sample cup. The cancelled Champollion DS4 lander was designed to reach 10 m depth and required the automated construction of the drill string from multiple segments. The Micro-Rosa payload cab employs a similar approach to the autonomous construction of multiple drill segments into a growing drill string for a depth of 2 m - it requires three separate motors. It suffers from the need to autonomously assemble the drill string beyond penetration depths of

1m. The combination of the need for autonomous drill string assembly and the problem of coping with dust offers a potentially hazardous situation for rotating parts which suggests that rotary drilling to high depths is a unreliable option. Honeybee Robotics Inchworm Deep Drilling System (IDDS) is an advanced design for penetrating depths 1~10 km. It is composed of a fore and aft section which uses a rotating drill bit at each end and braking shoes to provide reaction. The IDDS comprises two symmetrical segments each with a rotating drill bit at each end. A set of three braking shoes is mounted onto each segment to anchor to the walls of the borehole as the opposing segment pushes downwards. The two segments were connected by an extendible linkage powered by a linear actuator. Rotating helical flights on each segment pushed all cuttings to the rear of the vehicle. It was fully reversible capable of drilling downwards and returning to the surface by virtue of its symmetric design. IDDS was 1m in length by 10~15 cm in diameter with initial deployment via a launch tube. It was self-contained carrying its own power in the form of an RTG system to enable it to reach 1~10 km depth. It may incorporate a coring sleeve and/or GCMS analyser. This type of device would require a significant power rating to drive three braking shoes, the linear actuator and rotating drill bit at any one time. Furthermore, a GCMS package would impose an even higher power requirement and mass overhead. The high power requirement precludes miniaturisation of such a vehicle.

- Percussive drilling - This method is the most viable in terms of power consumption. But it has a low penetration rate and has difficulty with cuttings transport. Percussive drilling does not require drill fluid and utilise short length drill strings. Drilling mud should not be used as they can potentially destroy the integrity of the borehole environment. Examples include the Beagle 2 Mole, the Ultrasonic/Sonic Drilling/Coring device (USDC), NASA Mars Sub-Surface Explorer (SSX), etc. The USDC is based on a piezoelectric ceramic driven ultrasonic horn. It can drill through granite without blunting and it has low mass (0.5 kg) and a low power requirement (5 W). However, it has a relatively low rate of penetration (~10^{-4} m/s) and a small penetration depth. The use of detachable, self-propelled moles such as the Beagle2 Mole eliminates the need for long drill strings. Moles can penetrate into compacted regolith, though rock penetration is not possible. The Beagle2 Mole has a mass of 0.5 kg and a power requirement of 2~5 W. An electric motor restrains a percussive sliding hammer against a spring that is released once every 5 s. It draws power and data from a tether to the mounting vehicle minimising its mass. It has a relatively low penetration rate with a capability of 1 cm/min in sand or 1 mm/min in hardened regolith to a maximum depth of 5 m. NASA has developed a variant of the Beagle2 Mole - the 5 kg SSX - which utilises a spinning hammer on a screw thread. It requires 30-50 W to penetrate at 5 m/d in hardened regolith. The SSX, rated to depths of 200 m, is a mole that uses liquid carbon dioxide compressed from the Martian atmosphere and pumped from the surface through a thin tube to act as drilling mud. There is the possibility of using liquid Xe as drilling mud and/or epoxy fluids to extrude a solidifying hole casing. The use of fluids however introduces potential difficulties, as they require complex fluid handling capabilities such as pumps, valves and hydraulics.

Table 1: Referenced space drills

Spacecraft/Drill	DS2/drill	Beagle 2/Mole	Rosseta/SD2
Mass	<50 g (sample collection system); <10 g (instrument electronics); 1 g (diode laser assembly)	0.4 kg	3.6 kg
Size	~11 cm³ (sample collection system); ~4.8 cm³ (instrument electronics); 0.3 cm³ (diode laser assembly)	~2 cm diameter, ~32 cm long	10 cm diameter, 75 cm long (drill-sampler);
Drilling method	Rotary	Percussive	Rotary
Drilling depth	~ 1 cm	2 m (max)	23 cm
Sample dimension	<100 mg	50 mg x 3	3 mg or 20 mm³
Power	1.5 W (peak)	2 W (mean); 5 W (max)	1 W (standby); 4~12 W (drilling)
Experiments	Existence of ice	Search for chemical evidence of extinct microbial life	Evolved gas analyser; Ptolemy evolved gas analyser; imaging system

2. A NOVEL BIOMIMETIC DRILL

I.2.1. Wood wasp ovipositor

Sirex Noctilio, a type of wood wasp, uses its ovipositor to drill holes into trees in order to lay its eggs The ovipositor uses a reciprocating motion to drill into the wood and has a series of different teeth to cut and remove the wood and sawdust. As shown in Figure 1, the wood wasp ovipositor is about 0.26 mm in diameter, 10 mm in length, and in cross-section can be split into two significant halves: one side is the cutting teeth and the other is the pockets for the sawdust to be carried away from the hole.
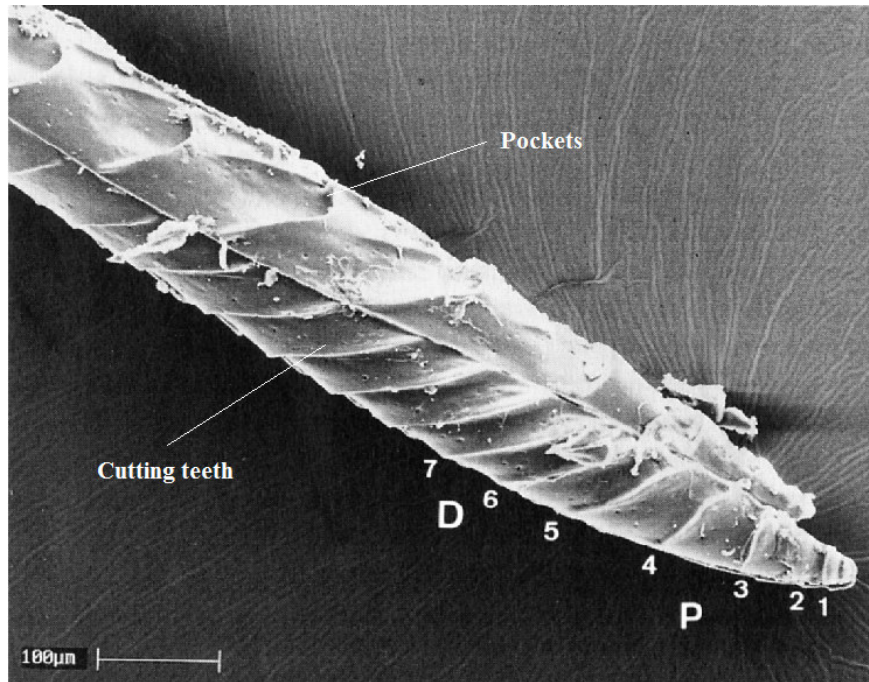
Figure 1: Sirex ovipositor: Teeth 1 to 4 point proximally (D) and are "pull-teeth"; teeth 6, 7 and higher point distally (P) and are "push teeth" [Vincent and Marcus, 1995]
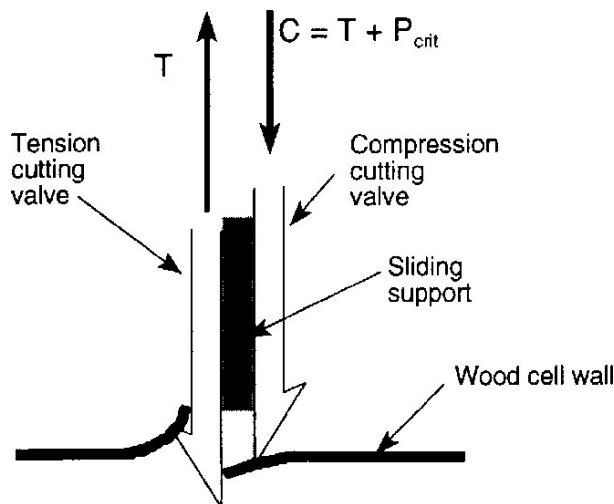
Figure 2: Model of ovipositor drill: the left valve pulls on a piece of wood cell with force T; the right valve adds this to the compressive force limited by the critical Euler buckling load, giving a total force for penetration of T+P_{crit} [Vincent and Marcus, 1995]

The wasp first stabs the surface of the wood in order to stabilize the ovipositor, which doubles the critical load. The initial cut is done by the small proximally facing teeth at the base of the ovipositor, which breaks the cell wall in tension (see Figure 2). The rate of drilling remains low until the ovipositor is well supported in the narrow hole. Once this is achieved the push teeth can be used to cut the wood in compression without the fear of buckling. The push teeth are arranged in a staggered pattern in order to even out the forces required in cutting. The sawdust from the cutting teeth is deposited into the pockets that then carry it to the surface on the upstroke. Two sides repeat this process in a reciprocating motion. The wasp cuts at a rate of around 1 mm/min in the initial stage and 1.5 mm/min in the later stages.

I.2.2.   <u>Reciprocating drill, novelty & advantages</u>

The ovipositor drill uses reciprocating rather than rotary motion. The drill bit is composed of two valves that can slide against each other longitudinally as depicted in Figure 3. Rather than the helical sculpturing of a rotary drill, the reciprocating drill has backward-pointing teeth that present little resistance to being moved downwards but engage with the surrounding substrate to resist being moved in the opposite direction. Once the teeth are engaged, the tensile force that can be resisted, tending to pull the drill out of the substrate, allows the generation of an equal and opposite force in the other valve tending to push it further into the substrate. The drilling force is generated between the two valves and there is no net external force required. The drill does not need to be forced into the substrate; it actively pulls itself into it. The limit to the drilling ability is the balance between the force required to pass through the rock, the degree of purchase that the teeth can obtain on the substrate, and the bending strength of the teeth when they are engaged with the substrate.

Another intriguing aspect of the reciprocating is how the drilling debris is disposed. At a slight glance, the pockets are formed alongside the cutting teeth. As the adjacent valves of the ovipositor drill are reciprocated, the debris from the cutting blade is transferred to the corresponding pocket, unclogging the cutting teeth ready for the next move. Since the two valves are moving in opposite directions, the debris is moved up the hole rather than deeper into it.

As aforementioned, conventional rotary drills (e.g. Rosetta/SD2) work on compression, which suffers from big mass, buckling problems, high power requirements and bit dulling/breaking/jamming. Another major limitations of drilling and sampling on low gravity environment like the asteroid is the need for high axial force when using conventional drills. This will again add penalty in terms of design complexity and mass. Though percussive drills (e.g. Beagle 2/Mole, USDC) may offer low power consumption, their drilling rate is slow. Section II.4.3 will demonstrate that the biomimetic drill outperforms the conventional drills in terms of power/drilling speed ratio.

Novelty and advantages of the reciprocating drill over conventional drills can be summarized as follows:

- No reactive external force and mass

- No restriction on the digging depth, since the drill requires no external components

- Minimize jamming

- Flexible in redesign, as the drill can be deployed independently of any other machinery
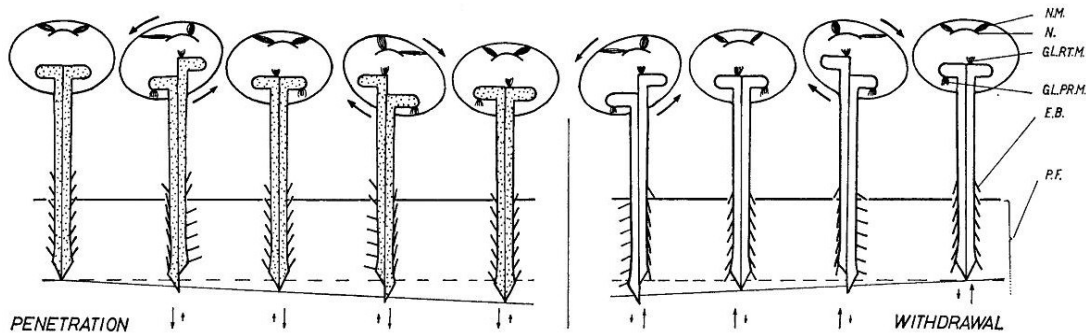
Piercing process during the first phase (perforation of the skin) and second phase (penetration into the pulp). (Diagrammatic; explanations on pp. 75 and 79). *C.ST.* = compressed stipes; *E.B.* = erectile barb; *GL.PR.M.* = galea protractor muscle; *GL.RT.M.* = galea retractor muscle; *GL.P.* = galea under pressure; *N.* = neck; *N.M.* = neck musculature; *P.F.* = pulp of the fruit; *S.F.* = skin of the fruit; *O.M.* = oblique muscle.

Figure 3: Biological reciprocating drill

The biomimetic drill concept indicates some of the enhanced utility that may be incorporated into engineered systems inspired from biological systems. Such enhanced utility is critical for space missions where premium is placed on mass, volume, power and data handling which drive the mission design. Biological systems are similarly constrained making biomimetic technology uniquely suited as a model of miniaturised systems.

II.   FEASIBILITY STUDIES OF BIOMIMETIC DRILL

1.   DRILL BIT DESIGN

To minimize power for effective drilling, structure and geometry are two factors to be considered in the design of drill bit. Figure 4 shows a few design options for the drill bit. These drill bits are constructed from half cones (increasing in diameter) and the edges of the cones carry out the griping and cutting action. The above-mentioned designs could suffer from inefficient grip and large stroke length. One solution is to use sharp pins or shims attached on the griping edge as shown in Figure 5. However, this design is difficult to manufacture, as the pins have to be pushed into the holes and fixed using lock-tight glue. This design is also too good in terms of gripping that operation at high velocity is required to unhook the pins out of the workpiece. Consecutive drilling may cause the hooks/pins to buckle and snap off gradually.

2.   SAMPLER DESIGN

Design of the sampler is inspired by barley-head. Placing a barley-head in between two hands, an oscillatory motion both backward & foreword will induce forward motion of the barley head (see Figure 6).

This method can work in reciprocating motion (i.e. one plate moves up and the other moves down with the same amplitude and frequency), which perfectly copes with the biomimetic drill bits. Once a particle is trapped between the angled bristles at the bottom of the plates, the bristle at one side lifts it and transports it to the opposite plant. Consequently the particles can be collected in between the bristles and transport to collection chamber placed on top of the plates (refer to Figure 7 and Figure 8).
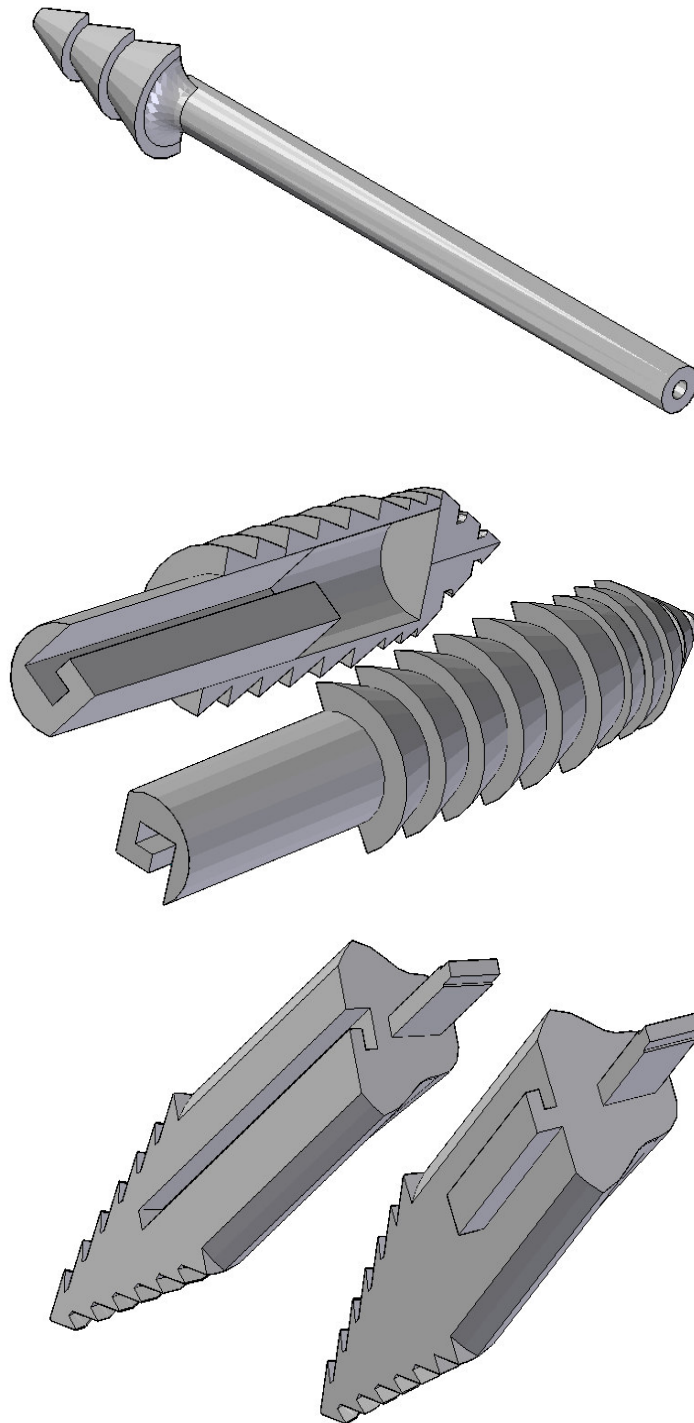
Figure 4: Design options of the drill bit: conical (above) and interlock (middle & bottom)
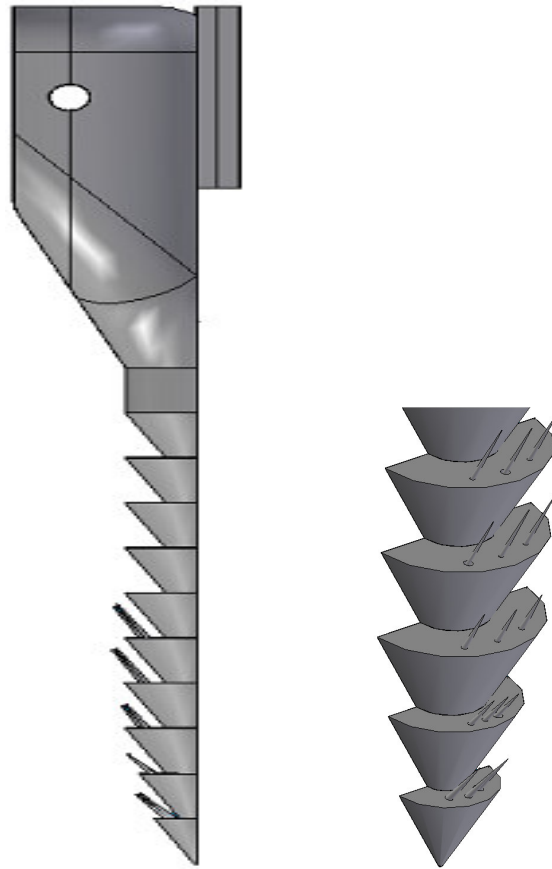
Figure 5: 2D and 3D view of the hooked drill bit

Figure 6: Barley-head (left) & motion of barley-head in hand (right)

2 Plates with angled fibres   Placed together   Particles at the bottom   Moving one side up & down moves the particls up, ejecting it to the side
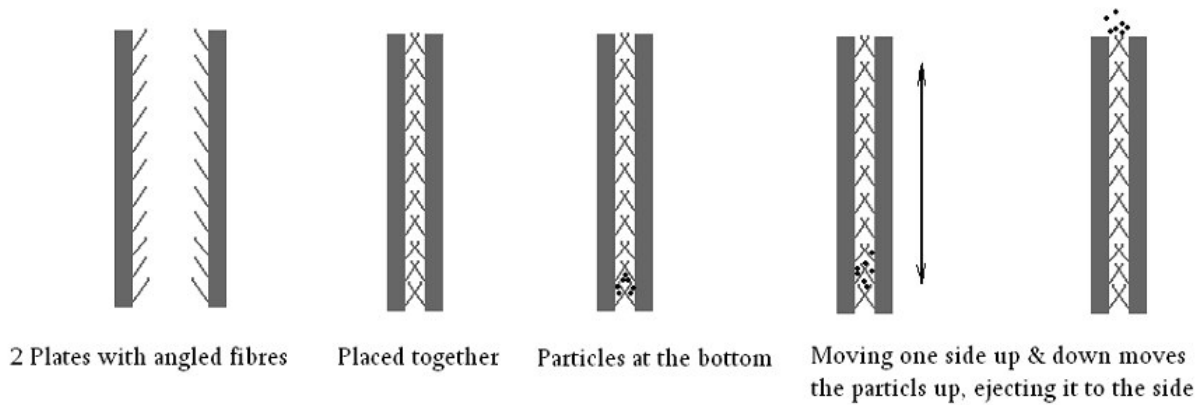
Figure 7: Removing sample from a hole
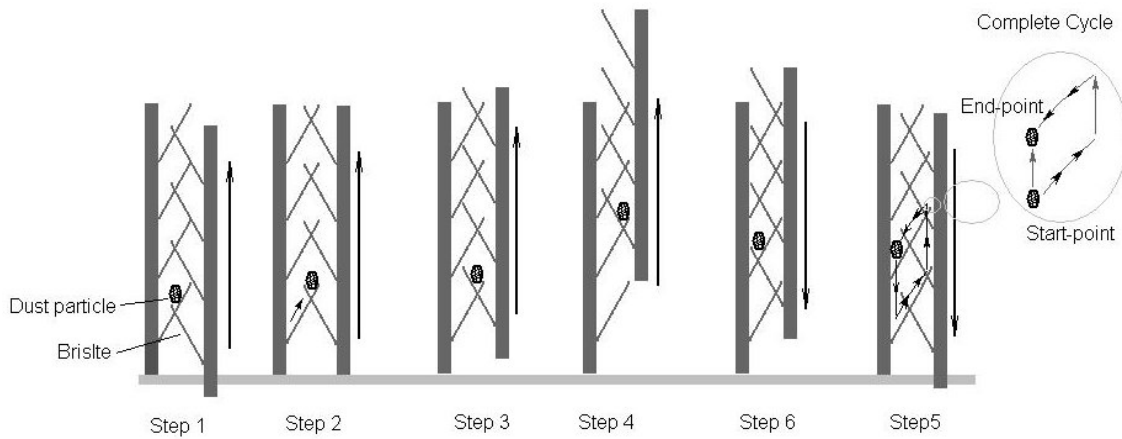
Figure 8: Sample extraction mechanism

3.   DRIVE MECHANISM

The following section illustrates various alternatives of drive mechanism that can be applied for this drilling problem.

II.3.1.   Dragon fly click mechanism

Design Features (see Figure 9):

■   Simple, minimum number of parts

- Mechanism automatically rids saw dust whilst digging

- Can be very small miniature in size

- Incorporates the use of latest technology, memory shape alloys

- Light weight

- Requires low power ~ 0.5 – 5W
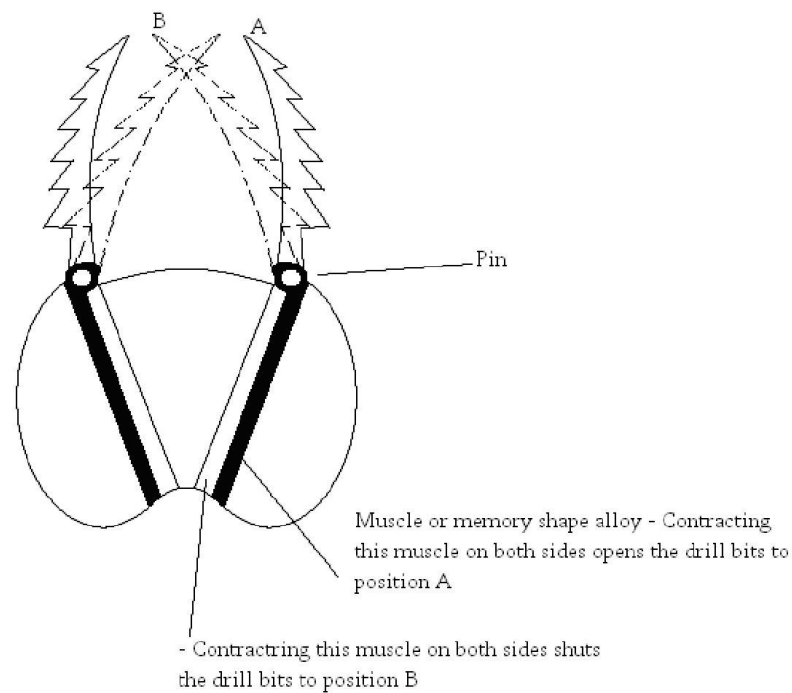
Figure 9: Dragon fly click mechanism

II.3.2. Helicopter rotary disc mechanism

Design Features (see Figure 10):

- Complex Design

- Possible jamming difficulties

Upper plate tilts or moves up, such that the drill bits can dig in sideways or move deeper into surface.
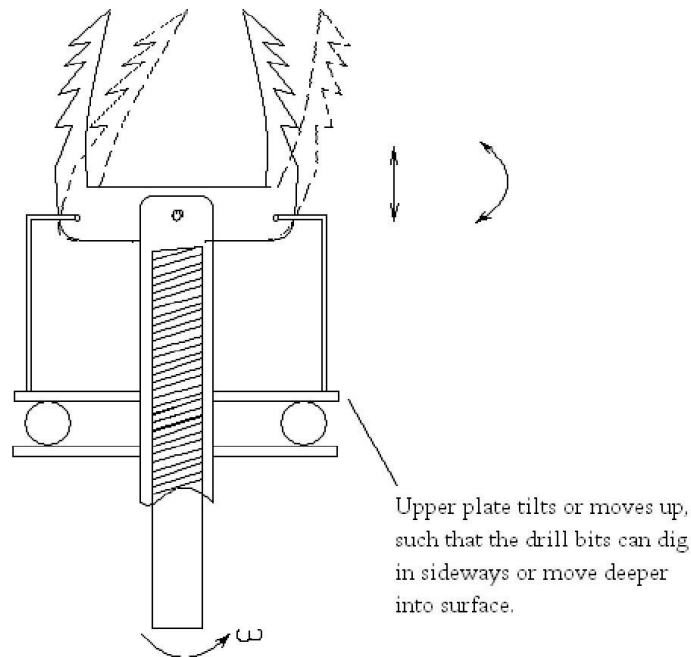
Figure 10: Helicopter rotary disc mechanism

II.3.3. Cam mechanism

Design Features (see Figure 11):

- Simple Design
- Can be bulky
- Requires moderate power

II.3.4. Grove in shaft mechanism

Design Features (see Figure 12):

- Complex Design
- Possible Difficulties in manufacturing
- Design can incorporate many drill bits depending on the shaft diameter
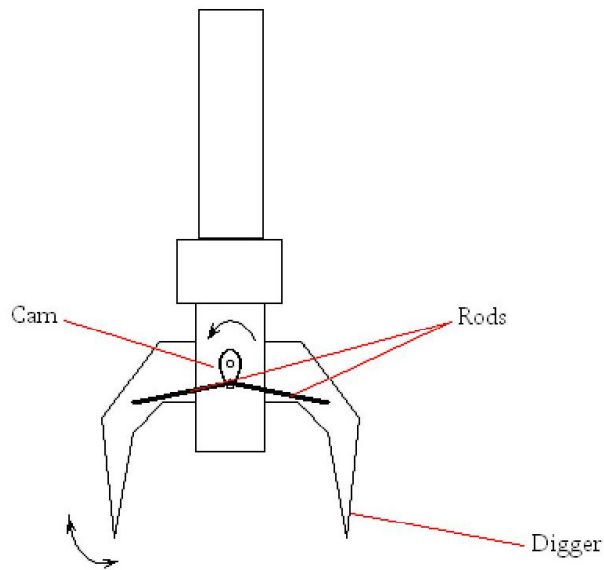
Cam rotation drives the diggers to
swing into the substrate via a rod

Figure 11: Cam mechanism
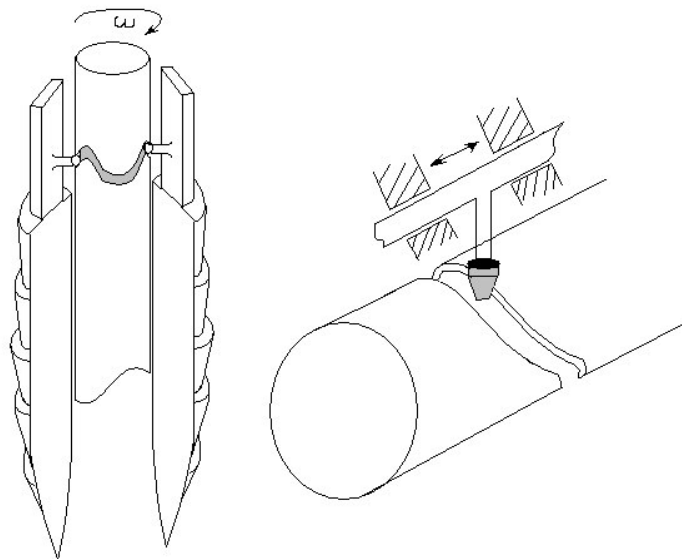
Grove in shaft, shaped such that the insert of the drill bit
is driven up and down following the path of the grove.

Figure 12: Grove in shaft mechanism

II.3.5. Chosen cam mechanism – pin & crank

Design Features:

- Simple Design

- Possible difficulties in manufacturing

- Versatile design

Having been through various designs, the most promising solution is a cam mechanism. Cam mechanism can be versatile and almost any arbitrary specified motion can be obtained. Cam mechanism offers the simplest and most compact way to transform motions. Figure 13 illustrates the recommended design.
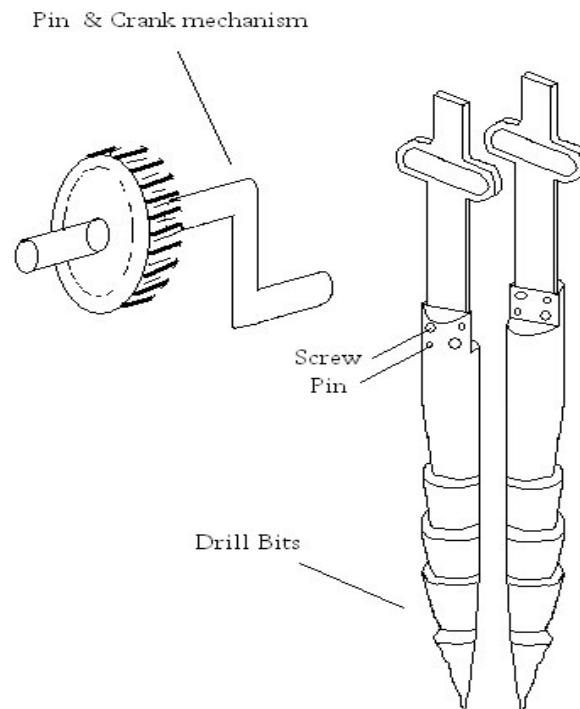
Figure 13: Chosen cam mechanism – pin & crank

II.3.6. Actuation method

In order to meet the major design requirement in terms of size, weight and power, the choice of actuation source is restricted. Normal electromagnetic motors tend to incorporate heavy metal components, have slow response and slack with power. However one choice of actuation source is a

piezoelectric motor. Piezoelectric motor show superior torque and response time relative to existing magnetic motors of their low profile shape. Piezoelectric Actuators can generate forces of several 10,000 N over a range of more than 100 µm with sub-nanometer resolution. Other advantages of piezoelectric actuators include:

- Electrical energy is converted directly into motion, absorbing electrical energy during movement only. Static operation, even holding heavy loads, consumes virtually no energy.

- The piezoelectric effect is related to electric fields. PZT actuators do not produce magnetic fields nor do they affect them. Piezo-devices are especially well suited for applications where magnetic fields cannot be tolerated.

- A piezo-actuator has neither gears nor rotating shafts. Its displacement is based on solid-state phenomena and exhibits no wear and tear.

4.   EXPERIMENTS & RESULTS

II.4.1.   Test model and apparatus

A 2D test model is illustrated in Figure 14. The overall apparatus consists of:

- Triple Power Supply Circuit (Supplying 15V)
- A/C Speed Controller
- Voltmeter
- Transducer Circuit
- Transducer
- Drill
- Force balance
- Workpiece

An existing jigsaw type design is used to actuate the test model and produce the desired system. Figure 15 and Figure 16 illustrate the actuation system. Figure 17 demonstrates the apparatus set up that is used to record measurements of the cutting forces.

II.4.2.   Calculation of cutting speed

A/C speed controller is used to tune down the voltage supply to the drill such that variable drill speed can be achieved. The speed of the cutting process is obtained via a transducer that is attached to the gearbox. The transducer reads the number of teeth on the motor-gear that pass its sensor per minute, dividing this frequency by the number of teeth on the motor-gear gives the RPM of the motor. The pin

and crank design within the gear box (illustrated in Figure 14) means that every half revolution the blade travels through one stroke, hence the cutting speed V of the blade is given by RPM/2, i.e.

$$V = \text{Stroke length} * \text{Revolutions in a stroke} * (\text{Frequency} / \text{Number of teeth}) / 2$$

Equation 1

The transducer circuit reads the frequency of the motor-gear teeth passing by the sensor and gives the output reading as a voltage (red via a voltmeter). The circuit is programmed such that the output voltage from the transducer is proportional to the output frequency of the gear teeth. By calibrating the maximum voltage to give maximum frequency and zero voltage to give zero frequency, a relationship between the voltage and frequency is generated such that variable motor speed gives variable output voltage via the transducer, which corresponds to a cutting frequency, i.e. maximum voltage of 10 V corresponds to max frequency of 2360 Hz and minimum voltage of 0 V corresponds to maximum frequency of 0 Hz. Linear proportionality gives Frequency = 236 * Voltage.

II.4.3. <u>Experiments on different rake angles</u>

In this experiment, the drill bit was manufactured with different rake angles (refer to Appendix C), and the main aim of this experiment was to measure forces (in the x and y direction) required to cut through the workpiece. The drill bits were designed using a CAD software called "Solid Edge" and because of its complex geometry the drill bit cannot be machined from a solid metal, hence for testing purposes the drill bit are to be manufactured using a Dimension "STRATASYS" Rapid Prototype (RP) machine. The RP machine uses ABS plastic to manufacture the drill bits and thus that restricts the choice of workpiece. Tests at this stage were conducted on condensed polystyrene. Four different drill bits are tested with rake angles of 10, 20, 30, and 40 degrees. The horizontal and side cutting forces were measured using a force balance for each drill bit, at variable stroke velocities.

Test results are illustrated in following figures, where polynomial trend line is used based on 10 sampling data to accommodation potential measuring errors. In this test, cutting velocity operates within a range of 0~0.4 m/s. Figure 18 shows that lower force is required to cut through the workpiece as the cutting velocity increases. Output power constraint of the drill can put a limit on the cutting speed (refer to Figure 19). Cutting velocity decreases as the rake angle of the drill bit increases within an output power limit (e.g. 2.5 W). Consequently, drill bit with rake angle of 10 deg has a wider cutting velocity range of about 0~0.09 m/s, while a 40 deg drill bit has a narrower range of about 0~0.05 m/s. Hence beyond cutting velocity of about 0.3 m/s the power requirement for the 4 different rake angles drops down to the power constraint region.
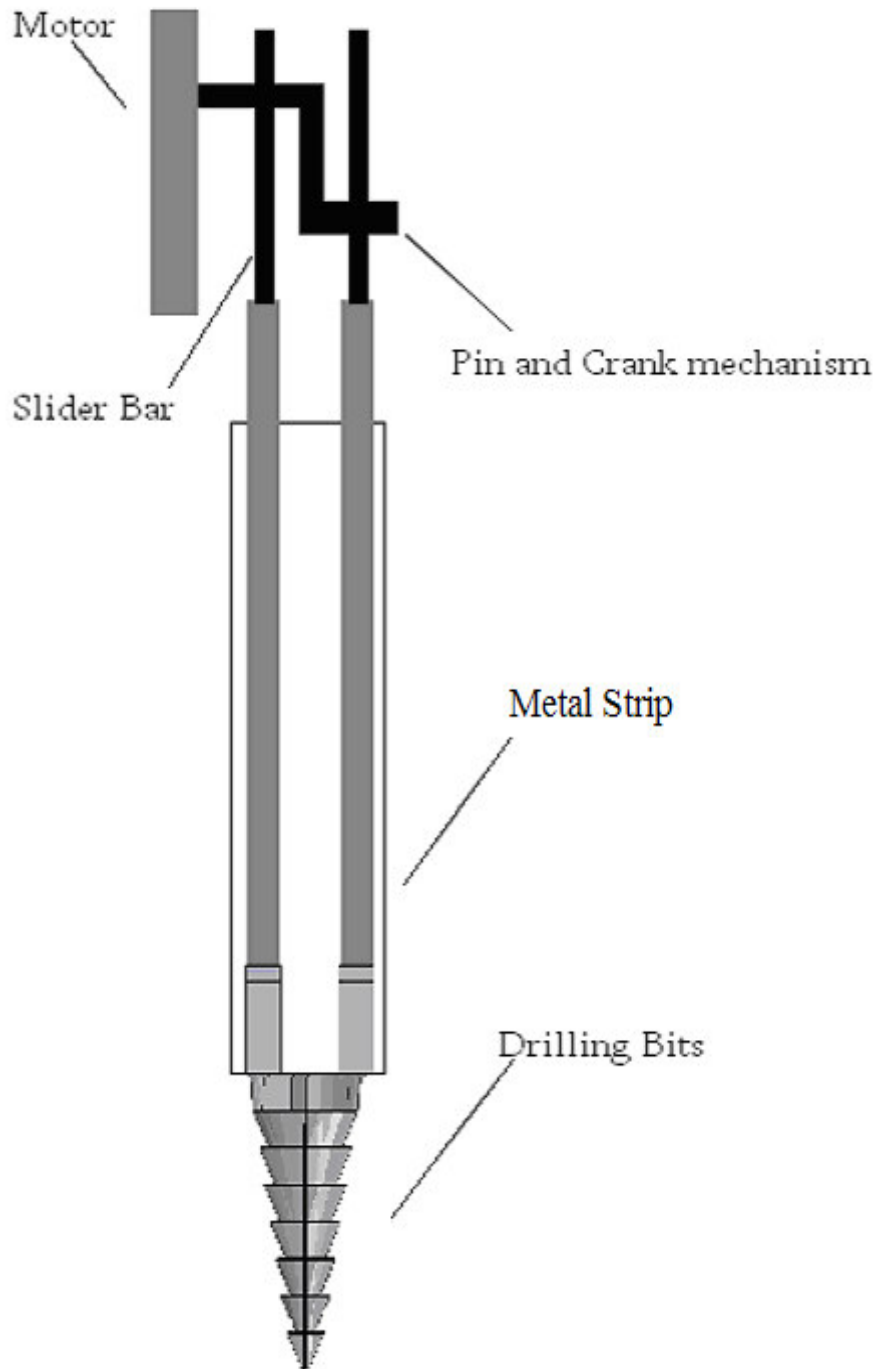
Figure 14: 2D test model
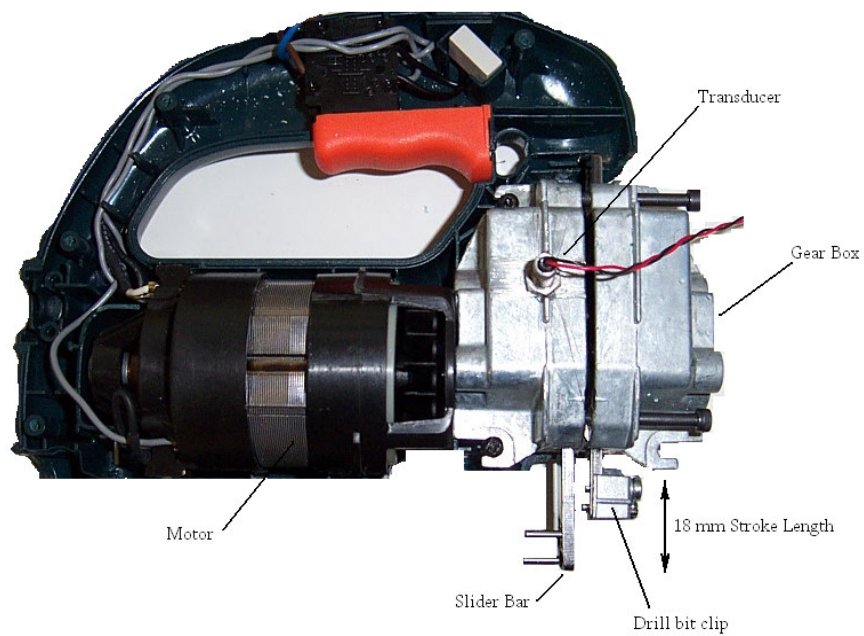
Figure 15: Side view of actuation
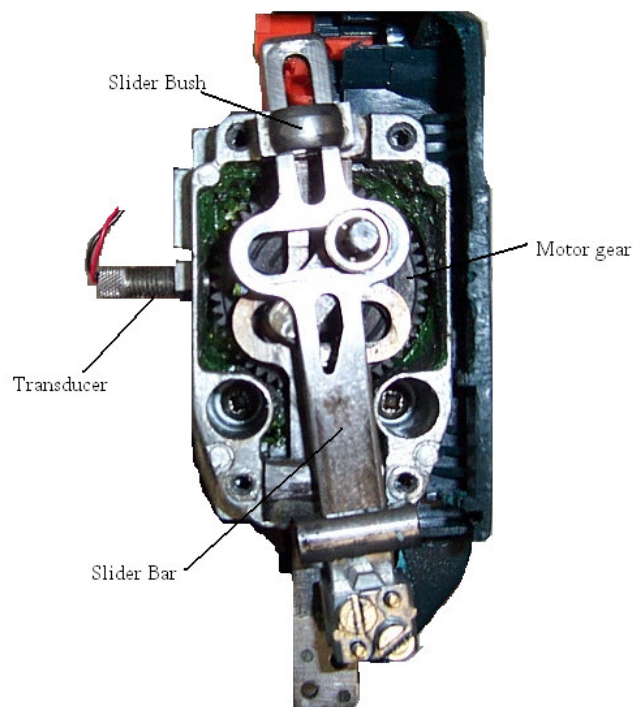
Figure 16: Front view of actuation
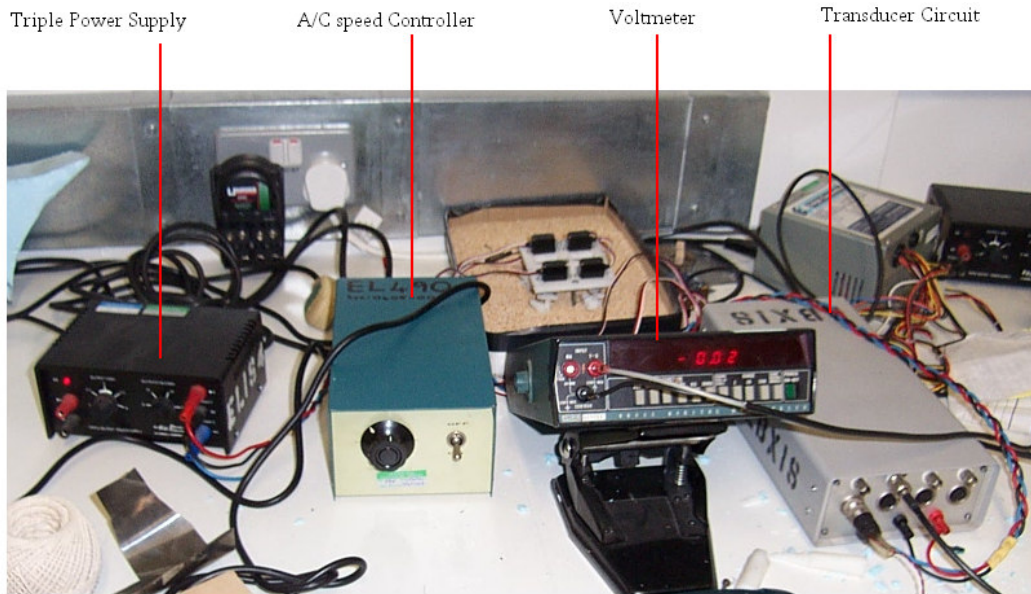
Figure 17: Apparatus set up

Figure 20 illustrates the energy consumption of the drill tip. It can be seen that as the rake angle of the drill bit increases the energy consumption increases as well. For same rake angle, the energy consumption seems to decrease gradually with increasing velocity. At high velocities of about 0.35 m/s 20-degree rake angle starts to have lower energy consumption than that of the 10 degree. This indicates that at low velocities, low rake angles are advantageous; however at high cutting velocities high rake angles become favourable due to their low energy consumption.

Figure 21 demonstrates the breakdown of energy consumption for a 10-degree drill bit. The graph shows that the majority of the energy is consumed due to shearing, which is nearly 40-60 % of the total energy consumption.
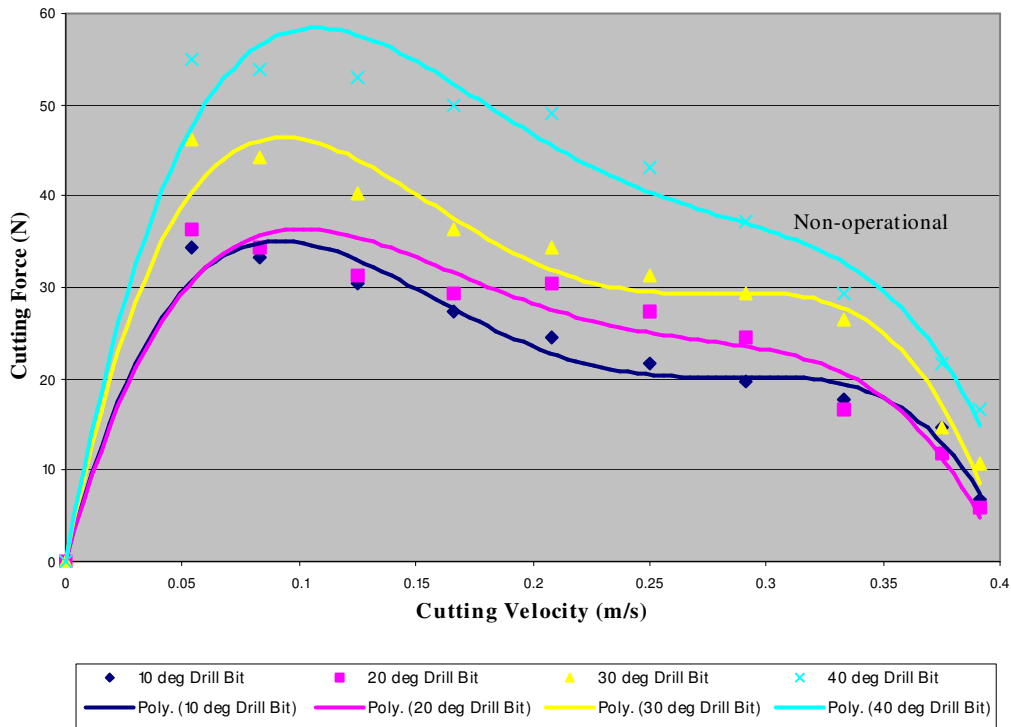
Figure 18: Cutting velocity versus cutting force
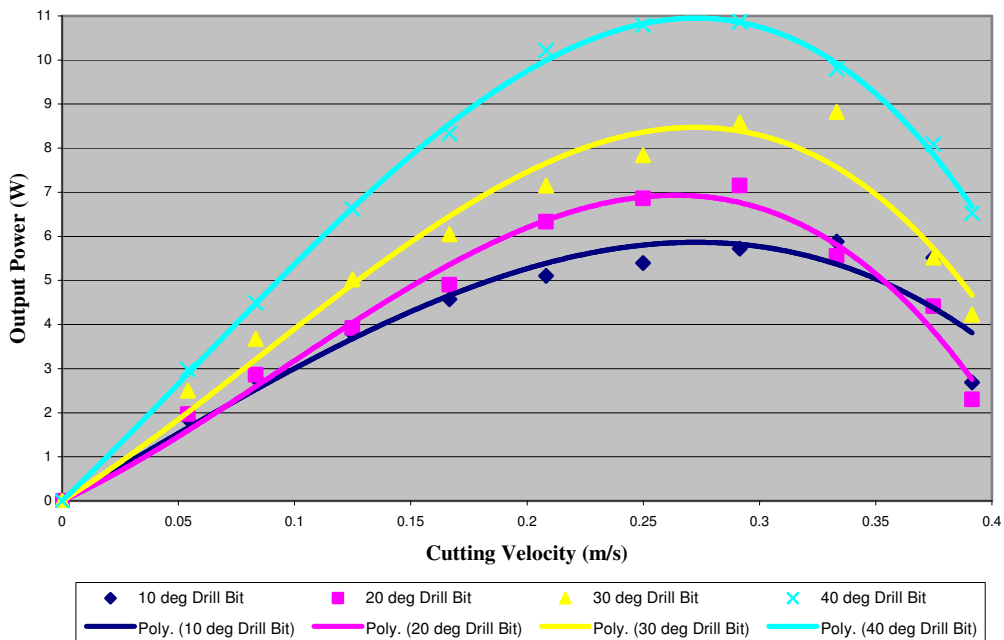
Figure 19: Cutting velocity versus power
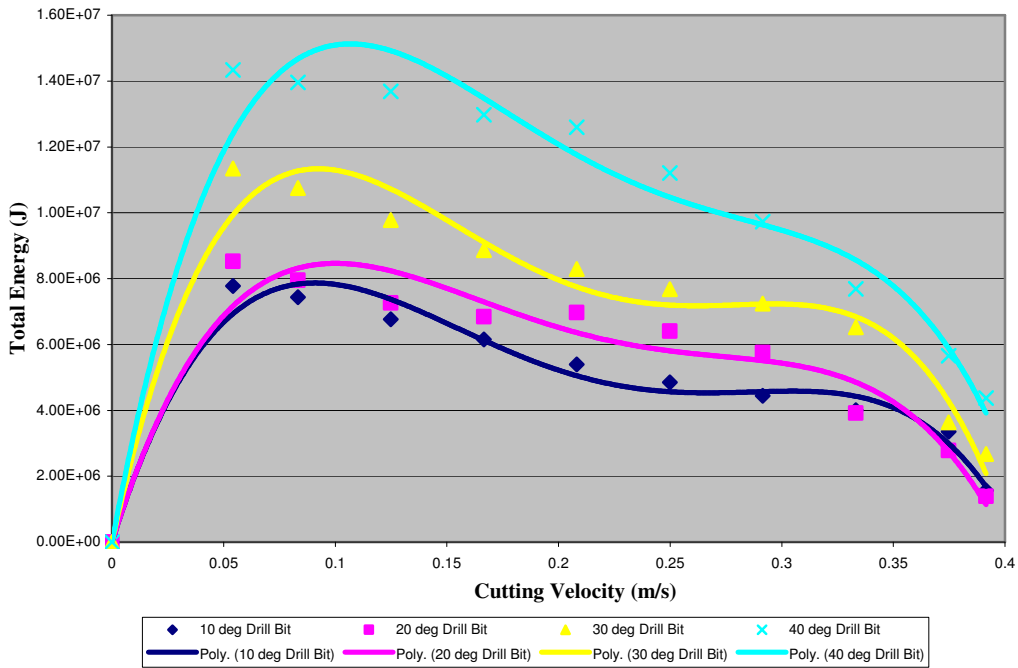
Figure 20: Cutting velocity versus total energy
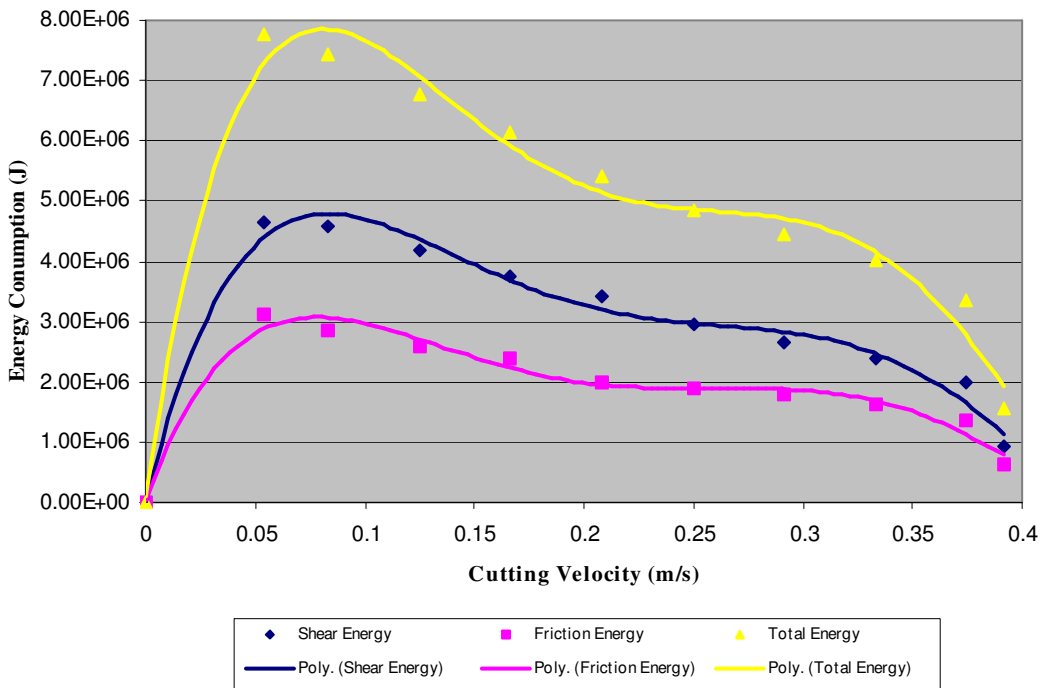
Figure 21: Cutting velocity versus energy for 10-degree rake angle

II.4.4. Experiments on different substrates

In this experiment, the dill bit was manufactured from metal so that it withstands testing on a tougher substrate. The idea is to use off-the-shelf coach screws with the right diameter, which are machined to cope with the drill prototype designed previously. This was done on a milling machine and the resulting drill bit is shown in Figure 22.

The drill bit was tested on 3 different substrates: condensed chalk, lime mortar and none-fired clay (see Table 2 for their physical properties). A range of voltage from 0 to 3 V (9 sampling data for each test), i.e. input power from 0 to 10 W, was input to the drill to generate a range of cutting speed from 0 to 0.375 m/s. Time was recorded using a stopwatch for drilling two holes of 0.018-m diameter and 0.025-m/0.05-m deep, where predrilled holes were formed to allow initial griping. Figure 23 records the time for drilling into three substrates at two different depths. Harder material like clay (blue lines) takes longer time to drill into than softer materials such as mortar (yellow lines) and chalk (pink lines).

Figure 22: Metal drill bit

Table 2: Physical properties of tested substrates

Substrates	Density (kg/m³)	Compressive strength (MPa)
Condensed chalk	1500	0.65
Lime mortar	1560	0.95
None-fired clay	1769	4.8

Drilling time versus drilling depth at different input power is illustrated in Figure 24 (chalk), Figure 25 (mortar), and Figure 26(clay). The test results tend to show that the drilling speed increases as the drill digging deeper. This could due to the fact that as drilling deeper the substrate starts to form cracks and hence becomes easier to be chipped off. However, we take a worse case by linearizing the test data to approximate drilling speed at different input power. Slope of the lines indicates the approximated drilling speed, which reasonably increases as the input power increases. Figure 27 plots the approximated relationship between drilling speed and input power in terms of power functions for different test substrates. Given input power budget of 3 W, drilling speed is approximated to be 9.4×10^{-5} m/s (chalk), 7.6×10^{-5} m/s (mortar), and 3.9×10^{-5} m/s (clay). Drilling speed with respect to the substrate compressive strength can be broadly predicted for 3W input power (shown in Figure 28).
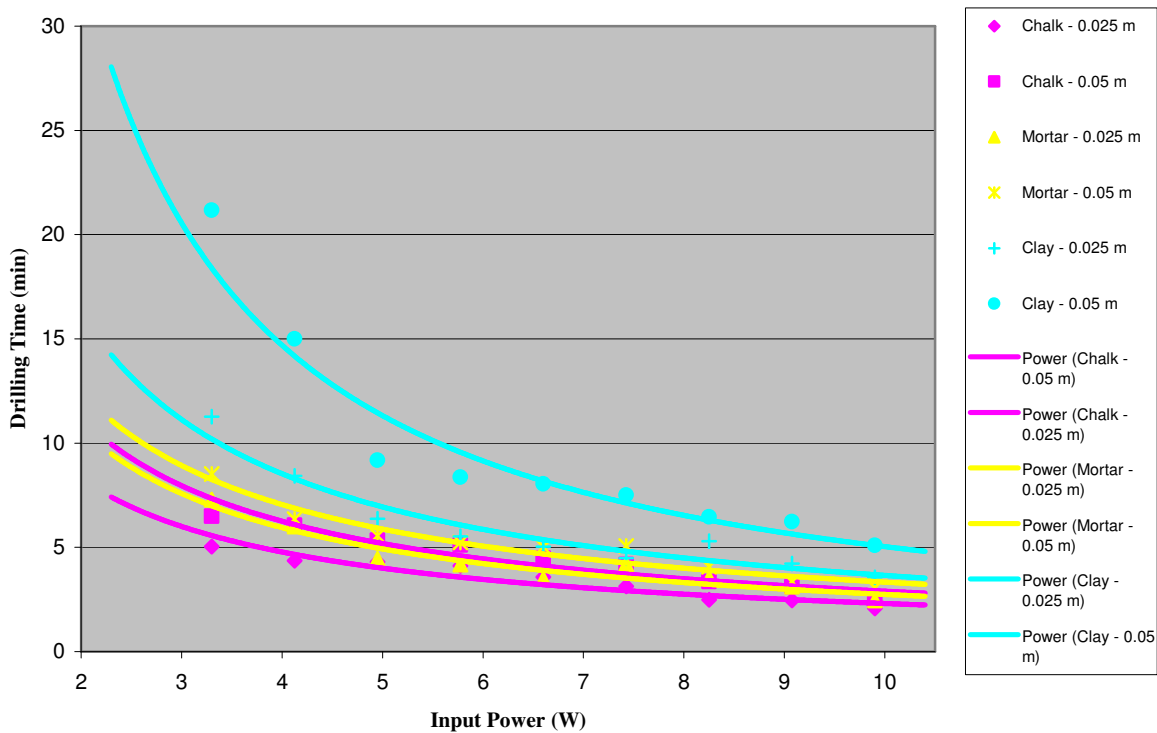
Figure 23: Power versus drilling time of 0.025 m/0.05 m depth
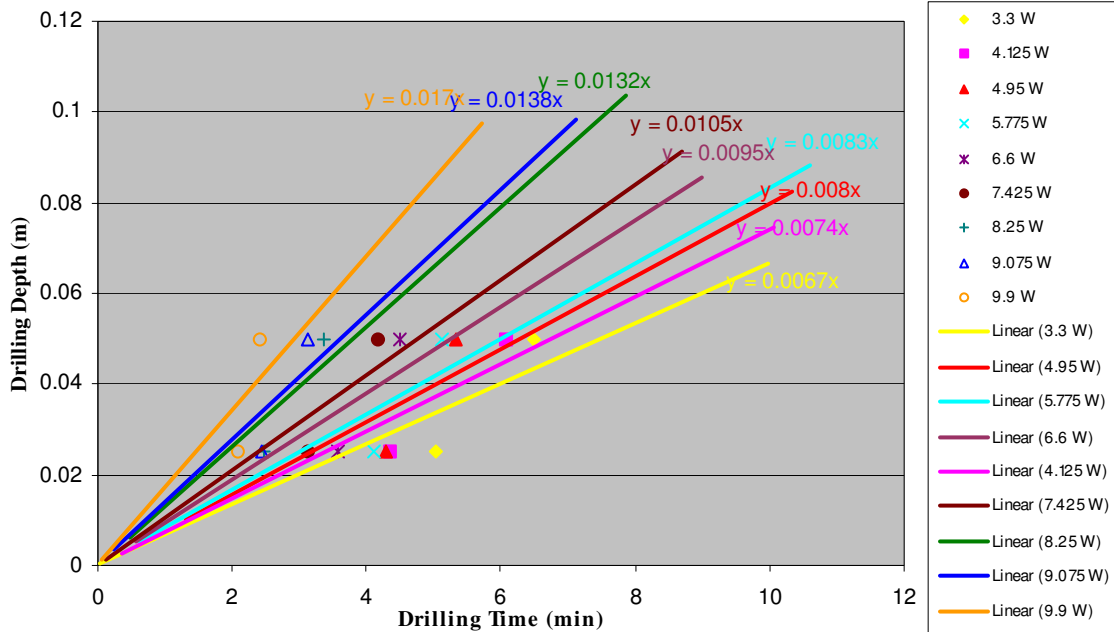
Figure 24: Drilling time versus drilling depth for chalk
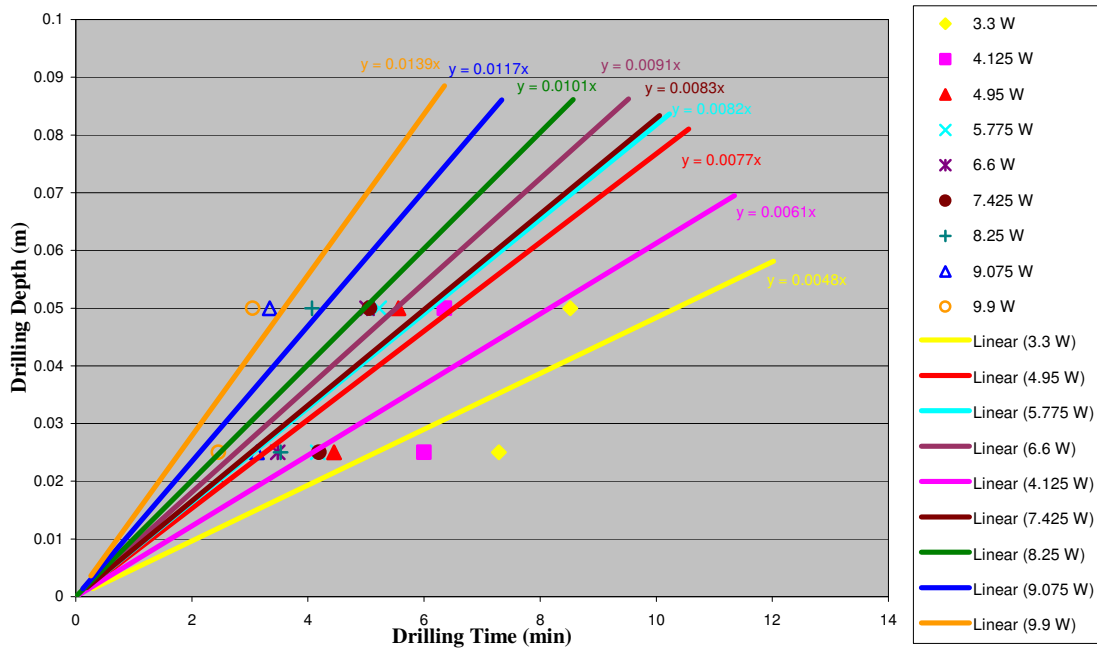
Figure 25: Drilling time versus drilling depth for mortar
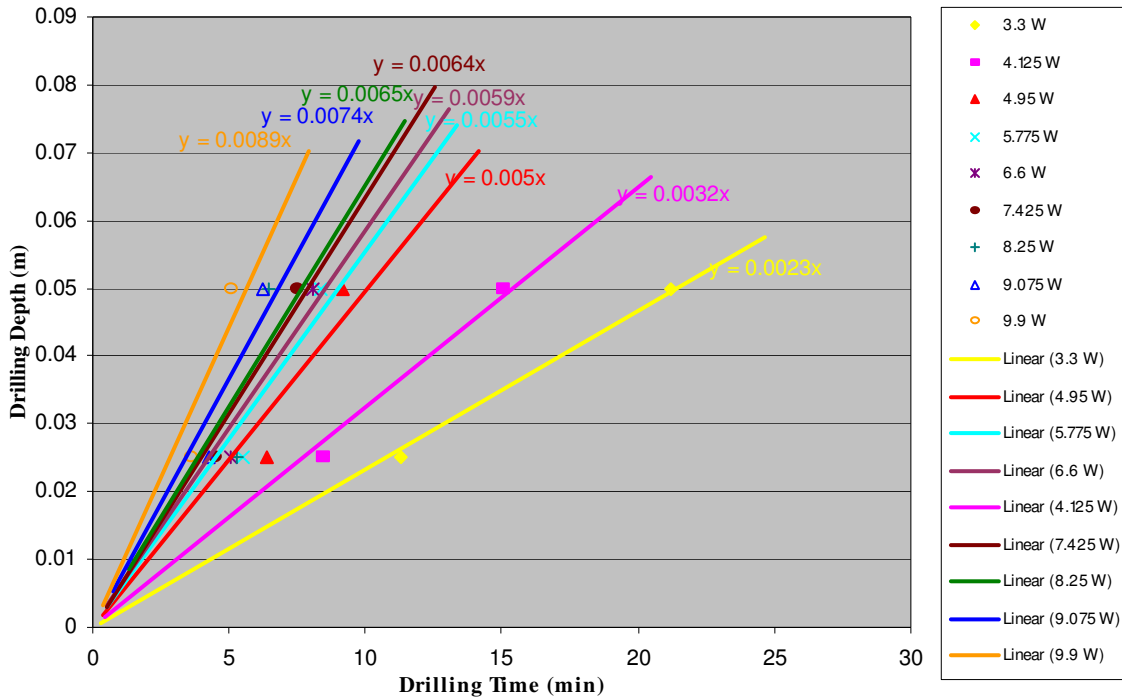
Figure 26: Drilling time versus drilling depth for clay
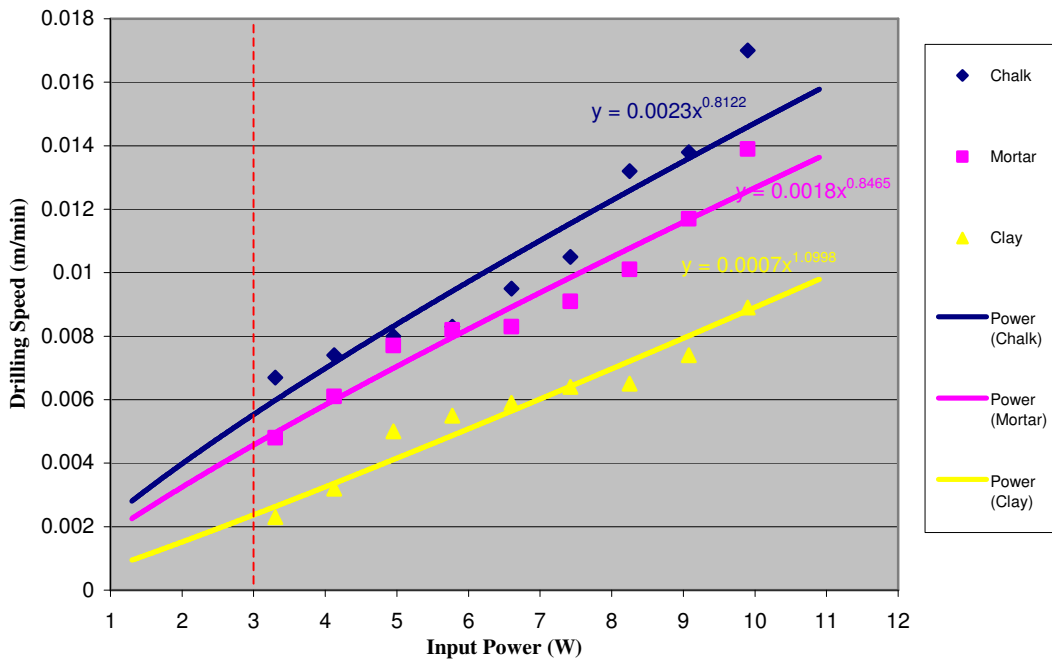
Figure 27: Approximated drilling speed versus input power
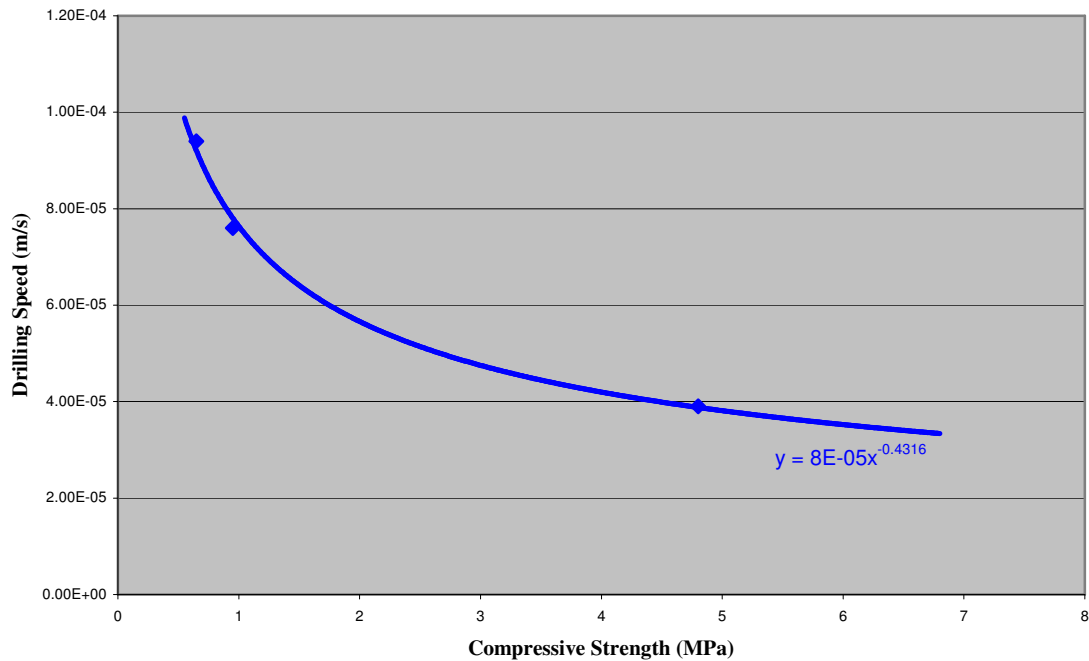
Figure 28: Predicted drilling speed versus compressive strength at 3W input power

Ratio of power over material removal rate, i.e. P/Q, provides a bold measure of the drilling efficiency in terms of power consumption and drilling speed. Smaller value of the ratio implies better efficiency of the drill. Table 3 compares the biomimetic drill with two space percussive drills. The proposed biomimetic drill provides comparable performance especially for handling harder substrates. For conventional rotary drills with similar performance would require high axial force of ~10^2 N.

Table 3: Comparison of different drills

	Biomimetic drill	Beagle 2/Mole [Kochan et al, 1999]	USDC [Bar-Cohen et al, 2001]
Drill diameter (m)	0.018	0.02	0.003
Power (W)	3 (max)	5(peak)	5
Drilling speed (m/s)	$\sim 10^{-4}$ (soil) $\sim 3 \times 10^{-5}$ (rock)	$\sim 2 \times 10^{-4}$ (soil)	$\sim 10^{-4}$ (rock)
Q (m³/s)	$\pi \times 0.009^2 \times 10^{-4}$ (soil) $\pi \times 0.009^2 \times 3 \times 10^{-5}$ (rock)	$\pi \times 0.01^2 \times 2 \times 10^{-4}$ (soil)	$\pi \times 0.0015^2 \times 10^{-4}$ (rock)
Power/Q (J/m³)	11.7×10^7 (soil) 3.9×10^8 (rock)	6.4×10^7 (soil)	7.07×10^9 (rock)

III.   ASTEROID MISSION PROFILE

1.   MISSION RATIONALE & OBJECTIVES

The primary objective of this mission is to investigate chemical composition of the asteroid, particularly biomarker molecules such as amino acids. Physical properties (such as interior structure, strength, density and heat flux) of the asteroid are of great interest as well.

A major goal of future space missions by ESA and NASA is to search for chemical signatures that might reveal the presence of extraterrestrial prebiotic and biotic signatures. What molecules should be looked for that will unambiguously answer whether those molecules are of biological origin? It has been argued that amino acids (with an emphasis on chiral forms) are the biomolecules to be looked for because of their essential role in biochemistry and because they are readily synthesized under plausible prebiotic conditions. To investigate their existence in asteroids would be of great scientific interest, as asteroids are known to be the remnant debris from the solar system formation process some 4.6 billion years ago (refer to Appendix B). In addition, organics have been identified in the meteorite analog of some types of asteroids. Although both sample return and *in situ* analyses can address these goals, the rapid development of microfluidic lab-on-a-chip systems, the complex logistics of sample return compared with *in situ* missions, and back-contamination issues suggest that *in situ* analysis is an approach that must be seriously considered [Hutt 1999].

As generally suggested, surface penetrator provides modest cost solution to such *in situ* astrobiological analysis. One advantage of the penetrator is that it imposes minimal mass overheads in comparison with other robotic devices. Furthermore, they can provide data on base rock composition by penetrating through regolith – this is of critical importance given the postulated regolith blanket on asteroids which shield base rock from remote sensing orbital instrumentation. For this asteroid mission, a micro-penetrator/drill package (not heavier than 10 kg) has been chosen by virtue of the general deployability at low cost. A similar package could be developed for multiple use such as missions to comets, Mars, Europa, etc. The additional drill serves the purpose of drilling deeper into the subsurface and taking samples. The micro-penetrator is likely to reach about 0.5~1 m depth through regolith/compacted regolith. Due to turn-over on asteroids and even Mars, the surface layers will not permit survival of organic material which decays on UV/oxidant exposure over aeons to carbon dioxide and other residues. We need to get below the oxidized layer to access organic material (e.g. on Mars, this layer is estimated at 2~3 m thick [Ellery *et al.*, 2003]. For the asteroids, we would assume this layer is about 1.5 m thick), hence the drill is able to provide the additional 1 m.

In summary, specific goals of this mission are:

- To determine the existence of amino acids inside asteroid
- To determine the interior structure of the asteroid

- To determine the strength properties and density of the asteroid

- To determine the thermal physics of the asteroid subsurface

- To increase understanding of the origin, evolution, and current state of the asteroid

2.   CHOICE OF TARGET ASTEROID

Based on the mission objectives and research interests, we have a few primary criteria for choosing a target asteroid:

- NEA (refer to Section VIII.1.1): we are interested in the NEA particularly due to its potential hazard to the Earth and ESA's present interests in NEO-missions

- C, D or P –type (refer to Section 0): their meteorite analogues contain organics

- 1~20 km in diameter: asteroids in such a size have porosity range of 20%~70% (refer to Section VIII.1.3); it implies comparable tensile strength over compressive strength, which is feasible for the biomimetic drill to operate; besides, larger asteroids have greater potential danger to the Earth

- Similar orbit as the Earth – it makes the asteroid easier to reach

Table 4 provides a list of potential target NEAs that fulfil the selection criteria. Properties of these NEAs were primarily estimated and obtained from previous studies [http://earn.dlr.de/nea/table1_new.html;http://arnold.usno.navy.mil/murison/asteroids/OrbitalElements.html; Lupishko & Martino 1998].

Further ranking of the target asteroids can be done based on preferences of the criteria. One example of using four criteria is as follows:

- Type, i.e. Apollo or Amor: where Apollo is preferable

- Diameter: a larger diameter is preferable

- Delta V: a lower Delta V is preferable

- Aphelion: a lower aphelion is preferable for reasons such as thermal and mission duration

Presuming the latter three criteria have higher weights over the first one (as they are more important), asteroid 1996 FG3 will rank the highest that is followed by Nereus, 1998 UT18, etc.

Table 4: Properties of potential target asteroids

Number/ Name/ Destination	Type	Diameter (km)	Group	q (AU)	Q (AU)	a[1] (AU)	e[2]	i[3] (deg)	Delta V (km/s)
1580 Betulia	C	3.9-7.08	AM	1.12	3.27	2.20	0.49	52.09	17791.22
3552 Don Quixote	D	13.25-18.7	AM	1.22	7.25	4.23	0.71	30.83	13070.34
4660 Nereus	C,E,P	0.4-1.5	AP	0.95	2.02	1.49	0.36	1.43	5365.61
5370 Taranis	C	4.4	AM	1.23	5.46	3.34	0.63	19.04	11897.95
14402 1991 DB	C	0.60-1.43	AM	1.03	2.41	1.72	0.40	11.42	8662.24
16064 1999 RH27	C	2.6	AM	1.22	4.55	2.89	0.58	4.40	9676.29
65706 1992 NA	C	1.9-2.9	AM	1.05	3.73	2.39	0.56	9.76	9502.46
85774 1998 UT18	C	0.9-1.04	AP	0.94	1.87	1.40	0.33	13.59	8858.96
1996 FG3	C	1.5	AP	0.69	1.42	1.05	0.35	1.99	5819.42
2000 PG3	D	4.2-4.5	AP	0.40	5.25	2.83	0.86	20.46	13875.12
2000 QN130	C	1.85	AM	1.24	4.55	2.90	0.57	2.56	9459.35
2000 YO29	C	2.05	AP	0.55	3.07	1.81	0.69	54.52	20592.76
2001 HA8	C	2.71	AM	1.12	3.65	2.38	0.53	11.55	10008.62
2001 RB18	C	1.43	AM	1.07	3.62	2.35	0.54	4.18	8526.96

---

[1] Semi-major axis in AU

[2] Orbital eccentricity

[3] Orbital inclination with respect to J2000.0 ecliptic in degree

3.   SYSTEM OVERVIEW

III.3.1.   Micro-penetrator

This design outlines a micro-penetrator probe concept (with a mass target of 5-10 kg) that aims to be deployed to asteroids and provide in-situ investigation of physical and chemical properties of asteroids. Such a micro-penetrator is suited for planetary deployment of terrestrial-type planets and small bodies of the solar system with the minimum of modifications. Instrumentation includes a novel biomimetic drill inspired by wood wasp ovipositor for sampling subsurface material, as well as various scientific instruments.

III.3.2.   Biomimetic drill

The biomimetic drill concept is inspired by wood wasp ovipositor, which drills into trees to lay the wasp eggs. The novelty of the ovipositor drill is to use reciprocating rather than rotary motion. The drill bit is composed of two components that can slide against each other longitudinally: in the wasp they are morphologically identical and move rather like the two parts of a *Ziplock* closure mechanism on a polythene bag. Rather than the helical sculpturing of a rotating drill, the ovipositor drill has backward-pointing teeth that present little resistance to being moved downwards but engage with the surrounding substrate to resist being moved in the opposite direction. Once the teeth are engaged, the tensile force that can be resisted, tending to pull the drill out of the substrate, allows the generation of an equal and opposite force in the other component tending to push it further into the substrate. Thus the drilling force is generated between the two components and there is no net external force required. The drill does not need to be forced into the substrate; it actively pulls itself into it. Thus there is no need for any reactive external mass, nor there is any restriction on the depth to which the drill can dig, since it requires no external components. The drill can be deployed independently of any other machinery. The limit to the drilling ability is the balance between the force required to pass through the rock, the degree of purchase that the teeth can obtain on the substrate, and the bending strength of the teeth when they are engaged with the substrate.

III.3.3.   Scientific instruments

We will further consider a sensor suite to maximise the scientific return within the engineering constraints of low mass, low volume and low power requirements. It is important that the surface elements of a space mission provide complementary data to orbiter instruments. Generally, this will maximise the quality of the scientific data so we make certain assumptions about typical orbiter instruments. Most planet or small body orbiters include the following mapping-based instruments:

- CCD visible imager for optical mapping

- Visible/IR spectrometer for thermal mapping (0.4-4µ)

- Ground-penetrating radar for sounding

- Radio science experiments

To achieve the mission objectives, a few scientific instruments will be taken on board and provide *in situ* experiments:

- Biomarker detector – to identify organic molecules
- Seismometer – to measure seismic activity
- Accelerometer - to measure impact deceleration
- Thermometer - to measure heat flux

4.   SYSTEM REQUIREMENT & SPECIFICATION

- Penetration depth: 0.5~1 m
- Impact velocity: 100~150 m/s
- Overall mass budget: 10 kg
- Overall size budget: 20 cm (diameter) and 50 cm (length)
- Overall power budget: 20 W
- Drilling depth: 1 m
- Drill mass: 0.5 kg
- Drill power: 3 W

IV.   DESIGN OF MICRO-PENETRATOR & BIOMIMETIC DRILL

1.   BACKGROUND

In 1974, the Space Science Board of the USA National Academy of Sciences recommended that surface penetrators should be considered as standard tools for exploration of the solar system. A penetrator, penetrating into the extraterrestrial surface by falling from orbit, is essentially a hollow cavity that allows the accommodation of scientific instruments and supporting subsystems. Several independent groups have considered the penetrator concept and led to conclusion that they are necessary and feasible tools of planetary exploration [Murphy et al 1981;Simmons 1977]. The final report of the *Ad Hoc* Surface Penetrator Science Committee submitted on 12 August 1976, stated in part:

> *"We firmly believe that penetrators represent a valuable and necessary platform for the conduct of certain essential in situ experiments in the exploration of a majority of solid solar system bodies"*

> *"Penetrators are superior to other landing devices (i.e. hard and soft landers), for some measurements, principally because they penetrate overburden material into underlying rock units. The concept offers a unique exploration tool capable of acquiring prime planet during one relatively low cost mission."*

> *"The Committee is convinced that penetrators can play a significant role in the exploration of the Moon, Mars, asteroids and the Galilean satellites"*

A penetrator system would provide a modest cost exploration tool capable of providing information on the characteristics of the solid body properties of a planet chemical composition and internal structure. Without penetrators, this fundamental information must be obtained by very expensive soft landers or partially inferred from remote sensing measurements. As shown in Appendix A, penetrators proposed in space missions include Mars 96 penetrators, DS2 microprobe Lunar A penetrators, etc. Table 5 provides detailed information of these penetrators. We use DS2 micro-penetrator as the baseline of our design.

A surface penetrator is an adaptation of the terradynamic vehicles to planetary landers. It is a self-sufficient space probe equipped with control systems and other devices to ensure its motion after separation from the spacecraft, descent into the atmosphere, penetration into the rock, subsequent measurements, and transmission of scientific information to the orbiter for relay to Earth. The penetrator consists of two main parts: the penetrating part (forebody) and the afterbody, which remains on the surface. A cable connects the two parts.

For most applications, the penetrator will be passively controlled to arrive at the surface in an attitude and with a velocity that will result in the terradynamic vehicle penetrating the surface. The forebody of the penetrator, which is cylinder-shaped and hollow to accommodate the principal science and electronics, moves the penetrator centre of gravity as far forward as possible. The aerodynamic fins and drag surface on the afterbody provide stability while the projectile is falling through the air. As the

forebody penetrates below the surface, the separable afterbody containing the antenna and a transmitter and command receiver, as well as some science packages, is left behind on the surface. This afterbody remains connected to the penetrator with a multiconnector umbilical that is paid out from the aft section of the forebody during the penetration. A sequence of science experiments is then conducted during the life of the penetrator and the data stored in an onboard memory until it can be transmitted to an orbiting spacecraft for relay to Earth.

Table 5: Referenced surface penetrators

Penetrators	Mars 96	DS2	Lunar-A
Mass	45 kg	3.572 kg: 0.67 kg (forebody),1.74 kg (afterbody),1.165 kg (aeroshell)	13 kg
Size	10~15 cm diameter (forebody); ~ 80 cm diameter (afterbody)	3.5 cm diameter,10.56 cm long (forebody); 13.6 cm diameter,10.53 cm long (afterbody)	14 cm diameter 90 cm long
Scientific Instruments	Seismometer, accelerometer, thermometer, neutron detector and alpha-proton-X-ray spectrometer (forebody); Gamma-ray spectrometer, thermometer, meteorology sensors, magnetometer, TV camera, transmitter (afterbody)	Temperature sensors, drill apparatus, 1-axis impact accelerometer (forebody); Primary batteries, pressure sensors, descent accelerometer, communications equipment (127mm high antenna) (afterbody)	Two-component seismometer, heat flow probe, tiltmeter, accelerometer, radio transmitter, antenna
Expected penetration speed	~80 ms^{-1}	~200 ms^{-1}	250~300 ms^{-1}
Expected penetration depth	4~5 m	0.3~1 m	1~3 m
Battery type and lifetime	1 year	9-11 V Li-thionyl; ~2 weeks	Li-SOCL2 (super lithium); 1 year

When the penetrator first impacts the surface as in Figure 29(a), the nose slices into the surface material, driving the material away from the penetrator and forming a shallow crater with a small amount of ejecta. At this time, the projectile's velocity is at its maximum (for the penetration event) and the deceleration, point W in Figure 29(d), is usually also high. As the penetrator continues to penetrate, the aftbody impacts the surface and shears free from the forebody as in Figure 29(b)(c). This event can frequently be seen as a deceleration spike, point Z in Figure 29(d).
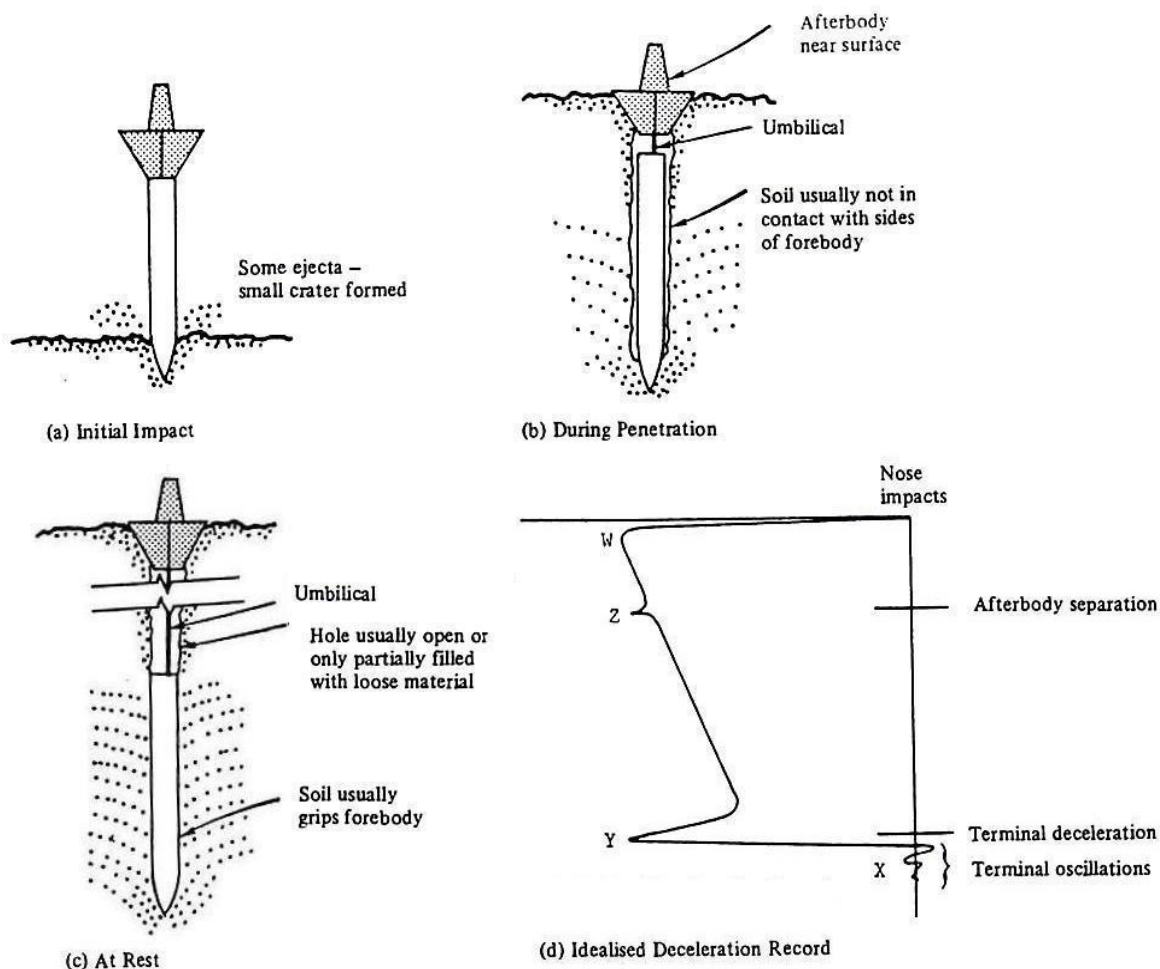
Figure 29: Penetration sequence for a separable penetrator

When the projectile has penetrated well into the subsurface but is still travelling at a substantial velocity, the penetration takes place mostly by the slicing action of the nose interval between points W and Y in Figure 29(d). This action shears and compresses a thin zone of soil/rock around the projectile and pushes the soil/rock particles away from the passing nose with considerable lateral velocity. During the intermediate part of the penetration event, this imparted lateral velocity drives the soil/rock particles well

away from the main projectile body. At all but the lowest of velocities the body has moved past before the soil/rock particles have commenced to rebound. As a result, only minor skin friction acts on the projectile body during the major part of the penetration event: usually, the paint on the penetrator afterbody is only slightly scratched during the entire penetration sequence. The soil/rock particles do, however, rebound somewhat after the projectile has passed and the resulting trajectory hole is typically smaller than the projectile that made it. During the terminal portion of the penetration event, the vehicle velocity becomes low enough that the rebounding soil/rock grips the penetrator as it comes to rest. In some cases, this gripping action leads to the highest decelerations, point Y in Figure 29(d), experienced during the entire penetration sequence, and frequently a terminal oscillation (point X) is observed as the penetrator is stopped by the elastic grip of the surrounding material [Young 1972].

2.   MICRO-PENETRATOR CONFIGURATION

A brief description of the penetrator size and weight budget has been given in Section III.4. After careful consideration of design alternatives, the 2D and 3D configuration concept shown in Figure 31-Figure 33 is a compromise of the myriad design factors involved. It is in some ways similar to the DS2 microprobes, but is more complex in terms of having on-board propulsion and control systems due to lack of atmosphere and gravity on asteroids (refer to Section V for details). An envelope of about 15 cm (diameter) x 45 cm (length) is currently envisaged for the entire penetrator, which is within our design constraints.

IV.2.1.   Forebody

The forebody target is of length 20 cm and width 5 cm. Starting at the nose, the conic shape has an aspect ratio (i.e. length to diameter) of 2:1 to provide an initial low resistance to penetration. The nose is blunted with half of the original length removed to improve ricochet resistance and prevent the penetrator from bouncing back. From the nose segment includes the drill and sampler subsystem. The forward diameter of the penetrator shaft is 5 cm to accommodation all scientific instruments, including biomarker detector (chip only), seismometer, accelerometer, and thermometer. The biomarker detector is envisaged to split between the forebody and aftbody, with the major electronics in the aftbody. The forebody is not foreseen to be subject to major size variation.

IV.2.2.   Aftbody

Aftbody is the conical terrabrake, which extends to a station 25 cm aft of the forebody with a base diameter of 15 cm, designed to arrest and absorb the impact in the surface materials of intermediate to high penetrability. At the back end of the terrabrake is sufficient volume to place the propulsion, power, data handling, and communication subsystems. By positioning these subsystems around the periphery of the base, the spin moment of inertia is maximized (this is desirable for stability purposes). The solid motor is largely driving the size of the aftbody, though the AOCS stability analysis will determine stable configurations.
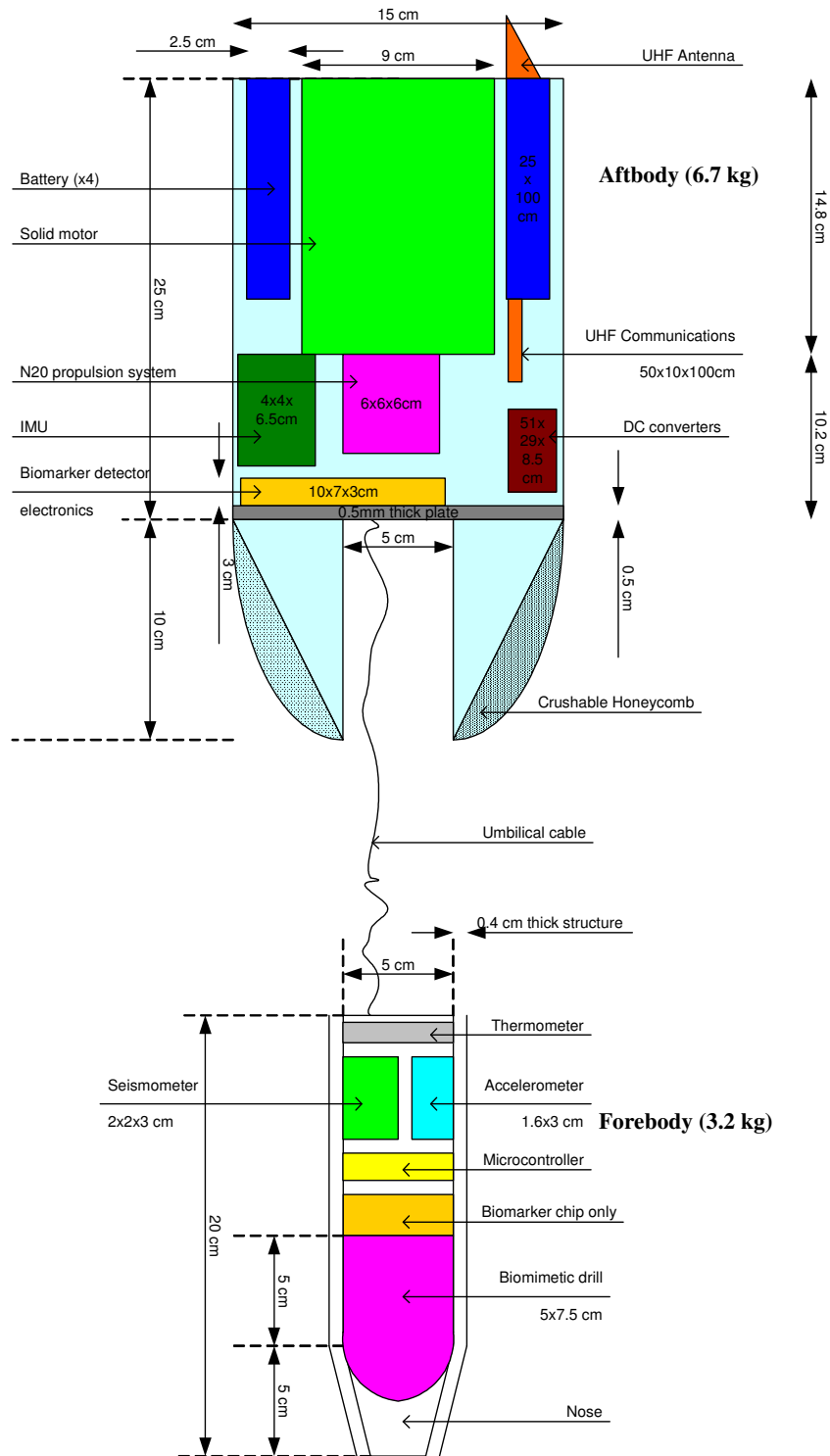
Figure 30: 2D schematics of the micro-penetrator
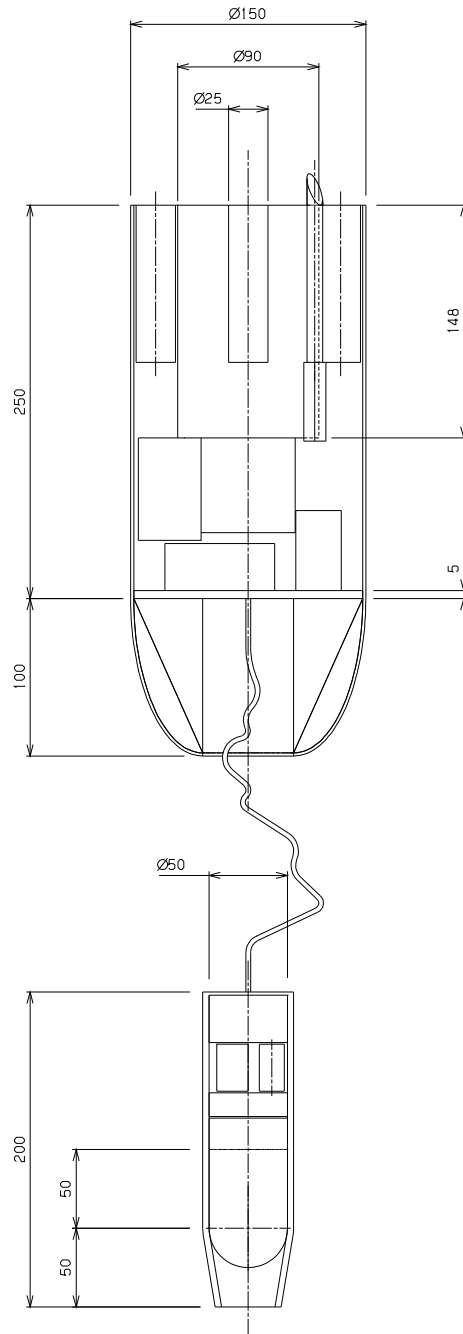
Figure 31: 2D engineering diagram of the penetrator
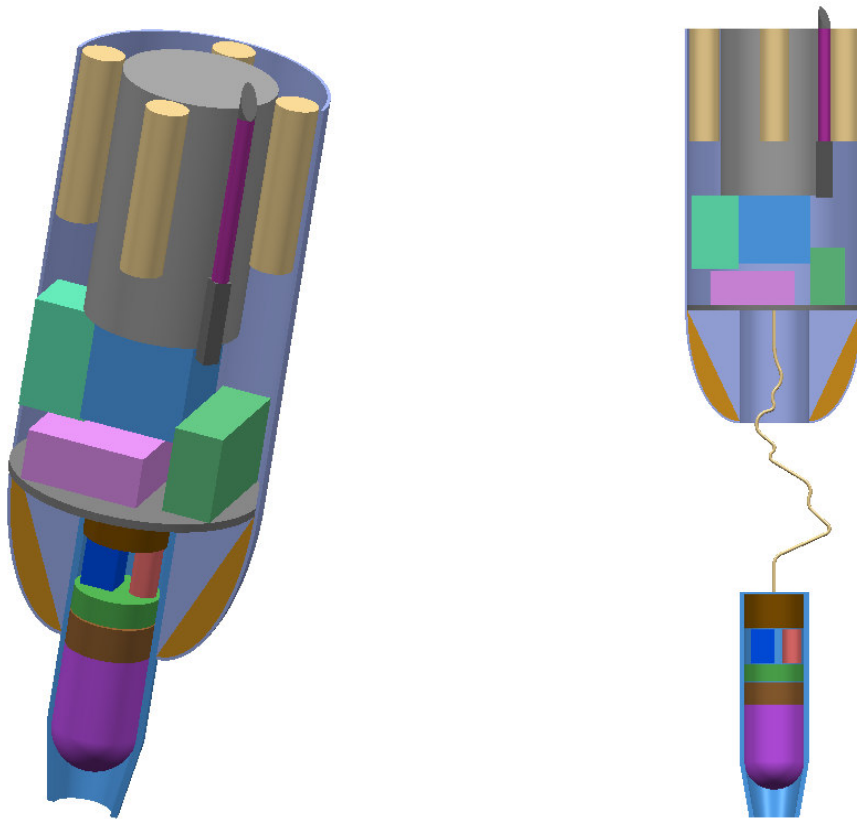
Figure 32: 3D views of the penetrator (1)

IV.2.3. Flexible cabling

To help reduce mass the volume and to survive the hard impact conditions, the probes contain very few wires. Instead, system electrical cabling is implemented using a flexible interconnecting system, also known as the umbilical cable. This flexible interconnect material is also used for the tether that connects the forebody and aftbody (see Figure 34).
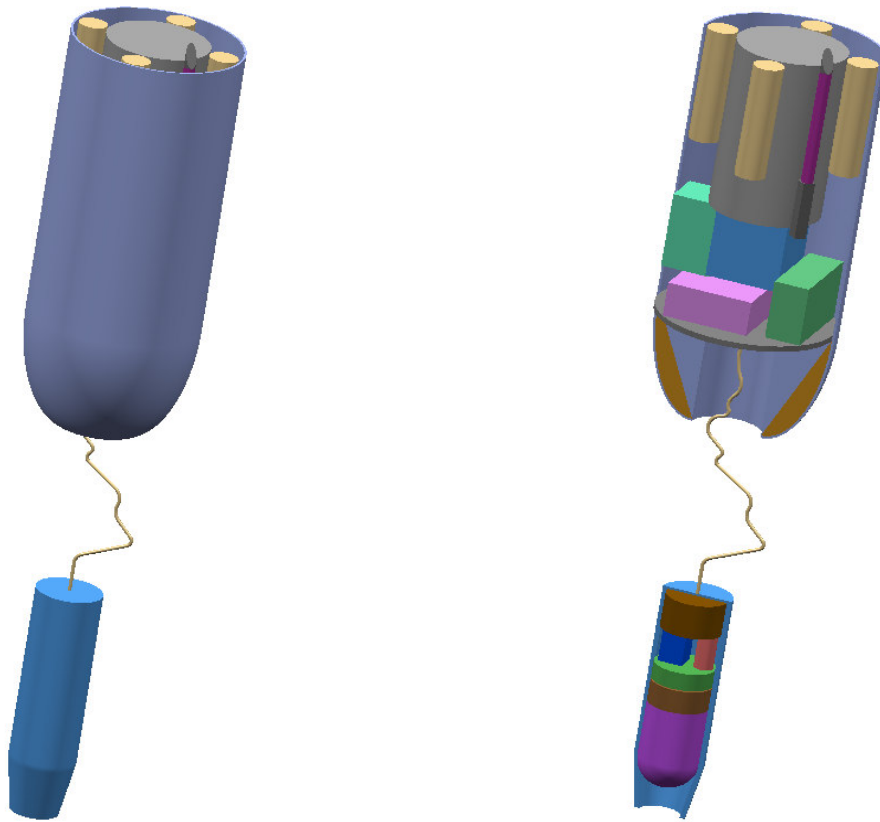
Figure 33: 3D views of the penetrator (2)

Figure 34: Umbilical cable

3. BIOMIMETIC DRILL

IV.3.1. Design constraints & specifications

- Target cylinder shape of 5 cm in diameter and 5 cm in length

- Target weight of 0.5 kg

- Target power consumption ~3 W

- Target drill depth of 1 m

- Target sample collection of a few milligrams

- Substrate material consists of carbon-rich rock with >20% porosity

- Ambient operating temperature < 0 ºC

IV.3.2. Drill & sampler subsystem design

The overall subsystem is housed within a cylinder-shaped capsule of 5 cm in diameter and 7.5 cm long (shown in Figure 35).

Crank-Pin Mechanism

Metal Strip Reel-Housing

pre- or post-deployment
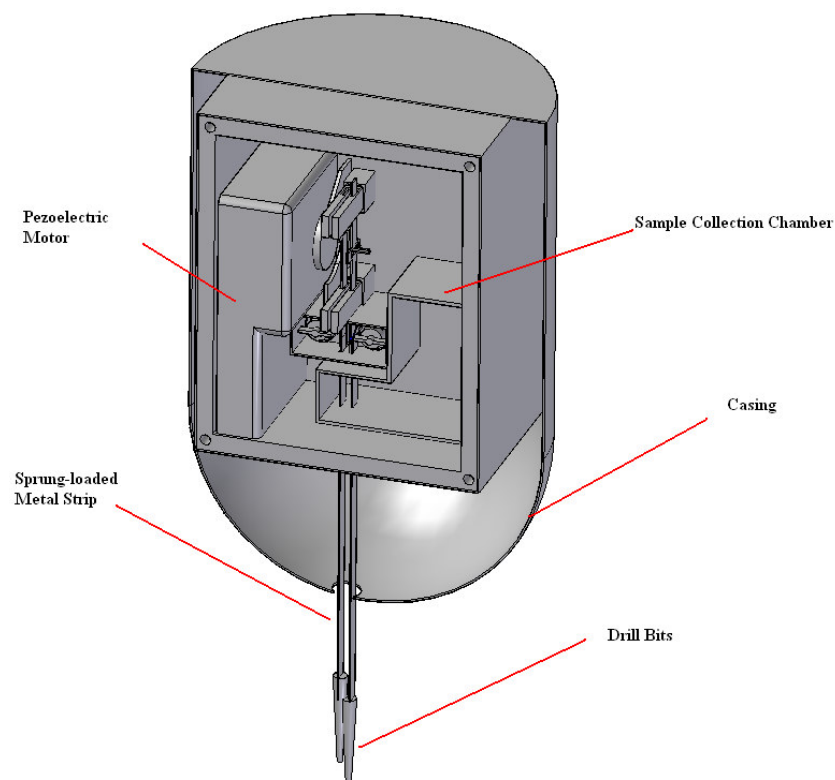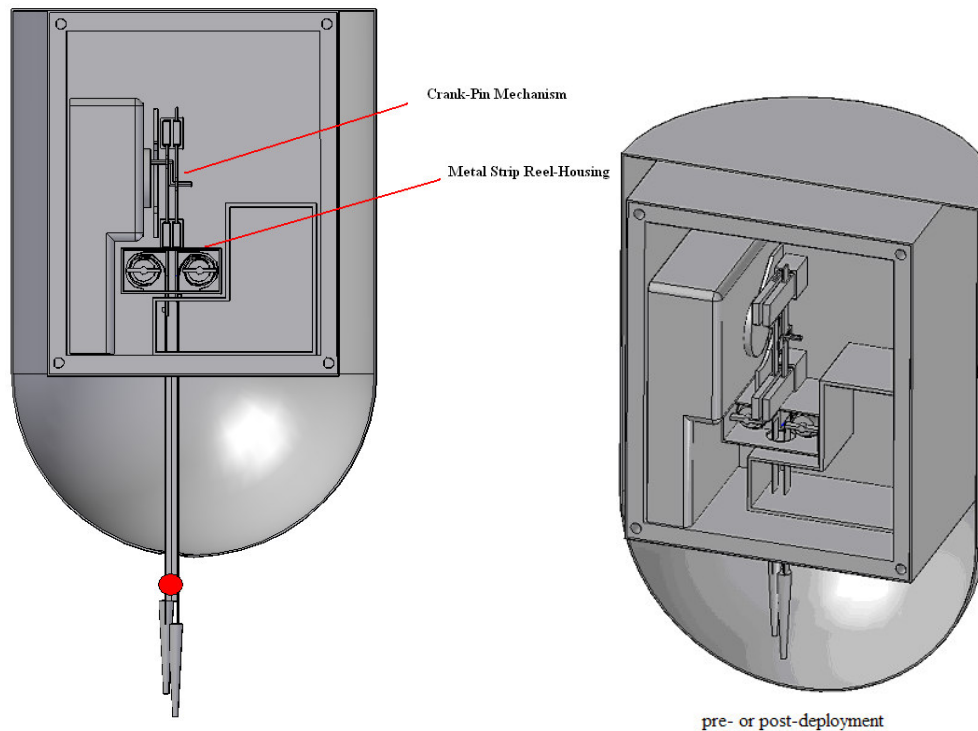
Figure 35: Drill and sampler subsystem

Drill bits are attached to a sprung-loaded metal strips, which is reeled into a housing. The design of the sprung-loaded metal strips is similar to a tape measure design, whereby the metal strip is wound into a reel. Upon reciprocation of the slider bars, the metal strip slides out of reel and housing. A guide way ensures that the metal strip is curved whilst the joint to the slider bar ensures the strip remains curved (shown in Figure 36). The curved metal strip is free to slide against the slider bar thus extending.

As the drill digs into the substrate, sample particles will move up to the sample collection chamber as aforementioned and a hole will be created. Once the drill bits are deployed the solenoid is activated to push the clip onto the metal strip that press onto the slider bar. This allows the slider bar to pull the metal strip back out of the hole.
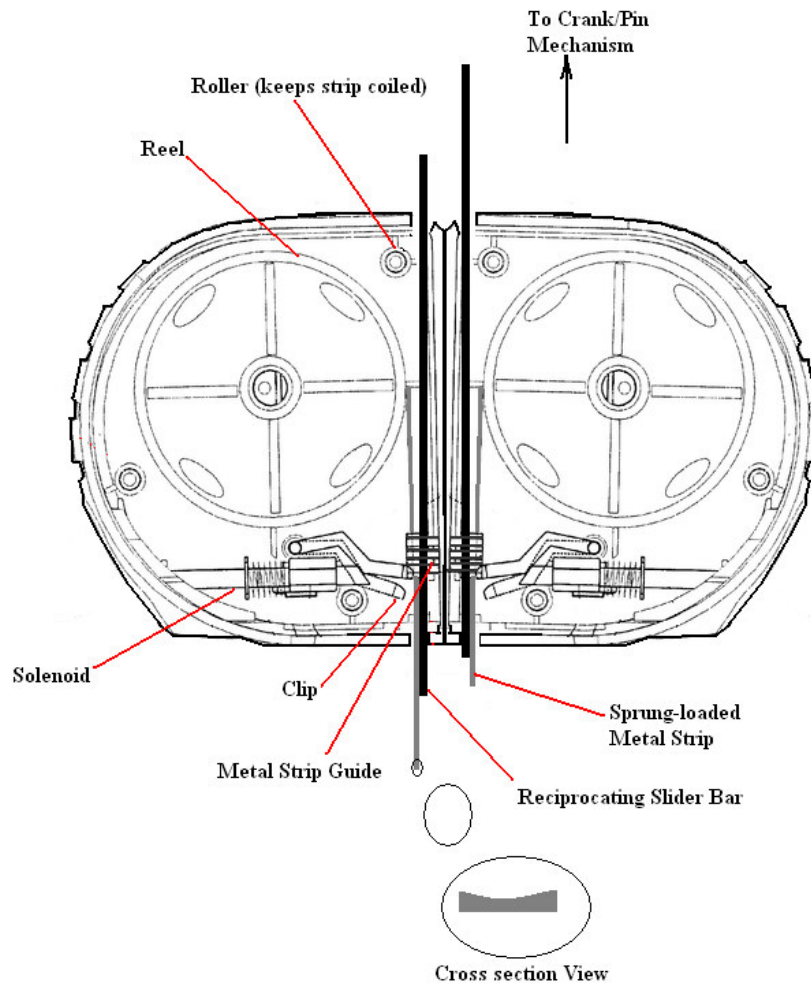
Figure 36: Metal trip reel housing

4.   SCIENTIFIC INSTRUMENTS & EXPERIMENTS

Irrespective of how novel the micro-penetrator/drill package may be or how challenging the engineering task of designing an asteroid penetrator system, the only justification for such a concept is how well it serves as a platform for the conduct of high priority science. For this particular asteroid mission, the scientific goals are clearly described in Section III.1. To maximise the scientific return within the engineering constraints, we have considered a complete sensor suite as shown in Table 6 to facilitate *in situ* measurements and experiments.

IV.4.1. <u>Biomarker detector</u>

Over the last decade, the drive to miniaturize common laboratory techniques has produced systems that are relevant for astrobiological research and solar system exploration, to name a few, microfluidics, microarray, and probe design. This has enhanced the feasibility and capabilities of *in situ* biomarker detection on extraterrestrial planets. Given mass and power requirement, three existing biomarker detectors are chosen as potential candidates for our penetrator. They include two biomarker chips and one laser Raman spectrometer: 1) Microfabricated organic analyzer by UC Beckley, JPL and UCSD, USA [Skelley et al, 2005]; 2) life marker chip by Leicester and Cranfield Universities, UK [Sims et al, 2003], and 3) Confocal Microscope and Raman Spectrometer (CMaRS) by Montana State University, USA [Dickinsheets, 2000].

Table 6: Scientific experiments and instruments of the micro-penetrator

No	Scientific instruments	Scientific experiments	Problems to be investigated
1	Biomarker detector (three options)	To determine existence of organic molecular, i.e. anomic acid, in the substrate	Chemical signatures that might reveal the presence of extinct or possibly extant extraterrestrial life forms
2	Broadband seismometer (by Microdevices Laboratory, JPL)	To measure seismic activity	Internal structure and dynamics
3	Piezoelectric accelerometer (ENDEVCO 2271AM20)	To determine physical and mechanical properties	Endogenic and exogenic crust formation processes
4	Thermometer	To measure the heat flux	Internal structure and thermal history

IV.4.1.1. *Microfabricated organic analyzer (MOA)*

The MOA is a microfabricated capillary electrophoresis (CE) instrument for sensitive amino acid biomarker analysis. The microdevice consists of a four-wafer sandwich combining glass CE separation channels, microfabricated pneumatic membrane valves and pumps, and a nanoliter fluidic network. The portable MOA instrument integrates high voltage CE power supplies, pneumatic controls, and fluorescence detection optics necessary for field operation. The amino acid concentration sensitivities range from micromolar to 0.1 nM, corresponding to part-per-trillion sensitivity.

IV.4.1.1.1. *Materials and Methods*

For the multilayer microdevice, 10-cm-diameter D263 glass wafers (Precision Glass and Optics, Santa Ana, CA) were patterned as indicated in Figure 37 and developed. The pattern is etched 20 μm deep for the separation channel and fluidic features and 70 μm deep for the manifold features. Both folded separation channels are 21.4 cm long and 110 μm wide, with 1.2-cm-long, 70-μm-wide cross-injection channels. The manifold wafer is blank on the bottom and patterned with the pneumatic manifold features for vacuum pressure lines and displacement chambers on the top. The fluidic wafer contains discontinuous channels patterned on its bottom surface to form valves. Vias and electrical, fluidic, and pneumatic access ports were drilled with diamond-tipped drill bits. The channel and manifold layers were aligned and thermally bonded to form the all-glass separation channels. Holes were punched through the 254-μm-thick polydimethylsiloxane (PDMS) membrane for vias and electrical reservoirs. The bonded wafer stack and PDMS membrane were UV–ozone cleaned, and the activated face of the PDMS membrane was applied to the top of the stack, sealing the manifold features. The fluidic layer was then aligned and fixed to the inactivated surface of the PDMS membrane. The sipper was coupled to the fluidic wafer by gluing a NanoPort to the sipper reservoir.

IV.4.1.1.2. *Design and Operation*

The microdevice shown in Figure 37 contains an array of 34 membrane valves and eight pumps. The valves comprise an etched displacement chamber on the top surface of the manifold wafer, a PDMS membrane layer, and a discontinuous channel structure on the bottom of the fluidic wafer. Applying a vacuum to the displacement chamber draws the membrane down, allowing connection of the fluidic channels. By placing three individually addressed valves in a row, a self-priming pump is created. The microfabricated valves are also used to create a bus for routing fluids to the sample reservoir. For example, by appropriate pneumatic actuation of lines 3, 6, and 8, fluid can be pumped from the fluidic reservoir out through the capillary sipper to the sample entry point. Actuation of lines 5, 6, and 8 pumps the sample back into the bus, where it can be diluted or directed to the separation channel for analysis.

IV.4.1.1.3. *Instrumentation*

The portable CE instrument is shown in Figure 38 along with a close-up schematic of the optical diagram and the chip manifold. The functions integrated within the MOA instrument include the laser excitation and optical detection system, production and control of electrophoresis potentials, actuation of the microfluidic valves and pumps, and control of the electrophoresis temperature.
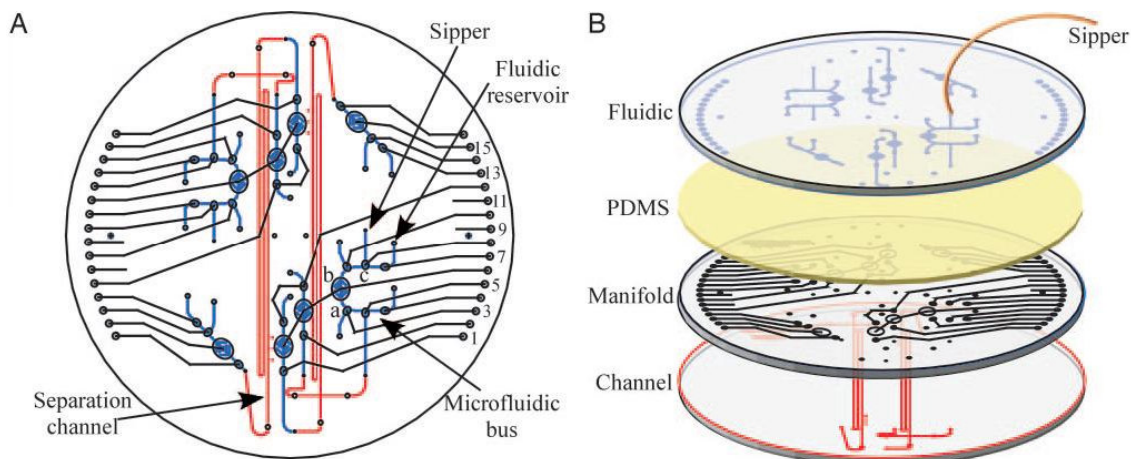
Figure 37: Microdevice for amino acid analysis: (A) Top view showing registration of the CE channel (red), pneumatic manifold (black), and fluidic bus wafers (blue); (B) Expanded view showing the microfabricated device assembly. The channel features are formed by thermally bonding the etched glass channel and manifold wafers. The manifold and fluidic wafers are held together by the PDMS membrane to create on-chip valves, pumps, and reservoirs.

Optical excitation is accomplished by directing the output of a 400-nm diode laser (CrystaLaser, Reno, NV) through a 430-nm dichroic beam splitter to an objective lens (Figure 38*B*). The planar face of the composite objective with a numerical aperture of ≈0.9 is placed against the bottom of the microchip, and the excitation light is focused 0.7 mm from the interface to form a 10- to 20-μm spot in the channel. The fluorescence is gathered by the objective, reflected by the dichroic, and passed through 430-nm long-pass and 522-nm band-pass filters. Confocal detection is accomplished by focusing the output into a 100-μmdiameter fiber-optic-coupled photomultiplier.

The instrument also contains power supplies, pneumatic components to control the valves and pumps, and a thermoelectric cooler (TEC) for keeping the separation channel at 8°C. Three miniature high-voltage power supplies provide the -15 kV and -3 kV electrophoresis potentials, and one HV solid-state switch enables floating the anode. A bank of 16 computer-controlled solenoids uses two rotary pumps to provide pneumatic pressure and vacuum that is routed. The manifold shown in Figure 38*C* clamps the microdevice to the instrument and provides electrical and pneumatic connections. Four insulated HV lines connect to the CE electrodes, which extend into 0.318-cm-thick PDMS moats for the cathode, anode, sample, and waste reservoirs. A tubing ribbon that extends from the bank of solenoids to the external manifold achieves pneumatic control. The external manifold also supports the removable TEC and fans.

At current stage, the instrument (includes chip, electronics, laser, optical detection and pneumatic controls) is about 35.6 x 30.48 x 10.2 cm, weighs 11 kg and has a peak power usage of 15W. These numbers are for the terrestrial version. For a flight version with electronics integration, the volume could be reduced to 1/3 to ¼ of this size, the mass should come down to 2-3 kg and the power usage lower since much of this is consumed in AC to DC conversion. In addition, this is for a system that would detect multiple channels and do a number of sample analyses. Further reductions are likely for detection of a single channel or a few samples. Here, a simplified and disintegrated version of MOA system can be used for amino acid analyses. The MOA chip shall be put in the forebody of the micro-penetrator, while the remaining electronics can be kept in the aftbody.
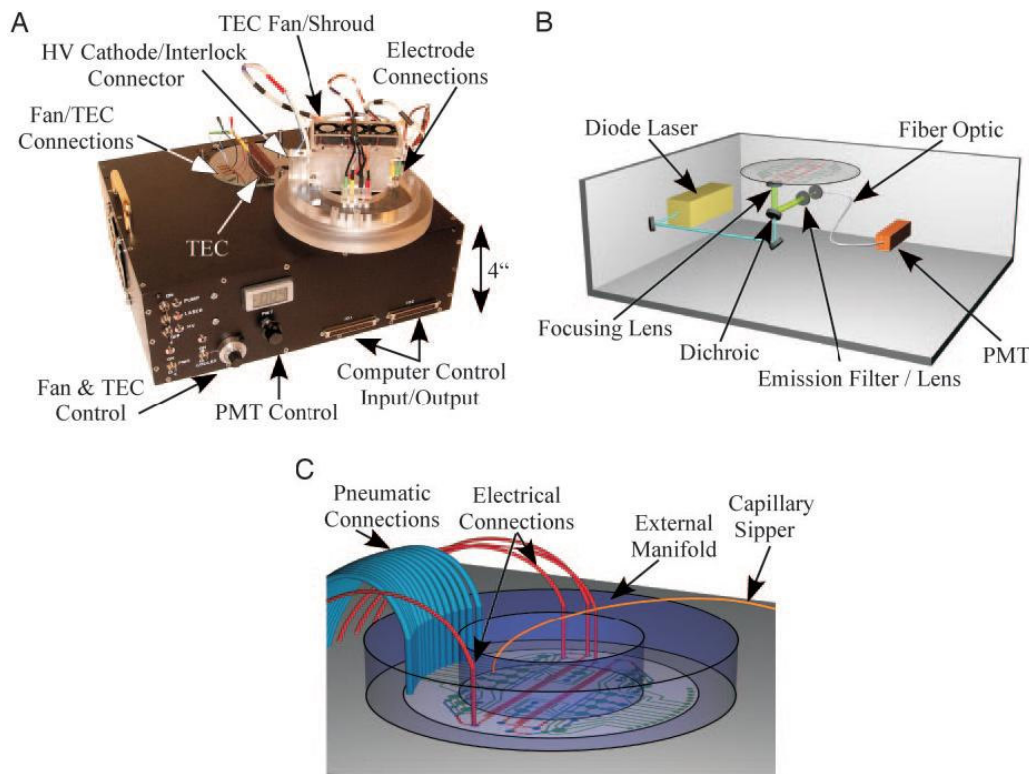
Figure 38: Instrument for amino acid analysis: (A) The MOA instrument contains electrophoresis power supplies, laser-induced fluorescence detection, a TEC for temperature control, and pneumatic actuation solenoids; (B) Schematic of the instrument showing confocal excitation and detection optics. (C) Close-up of the external manifold. Pneumatic and electrical connections extend out the bottom of the external manifold to interface with the microchip. The sipper extends out the top of the device for sample introduction.

IV.4.1.2.   Life marker chip

The major components of the life marker chip are: i) robust artificial molecular receptors comprised of Molecular Imprinted Polymer (MIP) recognition systems and ii) a sensor array comprised of both optical and electrochemical sensor elements. These fundamental components will be integrated together at the device level using ink-jet printing technology coupled with *in situ* photo-polymerization of the MIPs. The molecular receptor array in which large numbers of receptors are deposited on the measurement plane of an imaging interferometer (also forming the basis of an UV-NIR imaging Fourier spectrometer), read out by an imaging detector, enabling many molecular targets to be measured simultaneously. Target molecules include organic biomarkers, molecules exhibiting chiral partitioning, and hereditary macromolecules (DNA/RNA) along with organic control molecules of non-biogenic origin.

IV.4.1.2.1.   Molecular imprinted polymers (MIPs)

MIPs are synthetic receptors offering potential advantages over biologically based receptors including improved resilience to extreme conditions. They are compatible with most envisaged exobiology molecular biomarkers and can be wholly synthetic, eliminating the risk of contamination from terrestrial biomolecules. MIPs function as well, if not better, than traditional biological receptors ip non-aqueous environments. They are made by synthesizing highly cross-linked polymers from a mixture of functional monomers in the presence of a particular biomarker, resulting in self-assembly of the monomers around the template prior to polymerization. After extraction of the biomarker template (Dickert and Hayden, 1999), the polymer acts as a selective binding medium for the biomolecules or structurally related compounds.

IV.4.1.2.2.   Sensor array

The sensor array platform comprises both optical and electrochemical sensor elements with an emphasis on simple fabrication methods. For example, a micro-fabricated sensor array comprising 16 optical surface plasmon resonance and 16 impedance sensors on a 2 x 2 cm^2 support (see Figure 39). The two forms of sensing elements to be included are i) front or rear illuminated optical evanescent refractive index sensors based upon surface plasmon resonance on gold- coated diffraction structures etched into the glass and ii) inter-digitated gold electrodes for electrical admittance/impedance measurement.
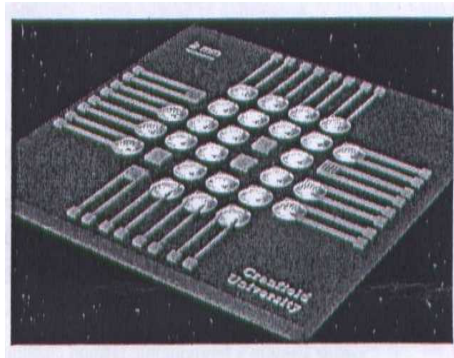
Figure 39: MIP-array chip technology demonstrator comprising 16 optical surface plasmon resonance (central gold pads) and 16 impedance (peripheral inter-digitated electrodes) sensors, most coated with MIPs, on a 2x 2 cm² support

IV.4.1.2.3.   Molecular receptor array

The molecular receptor array is based around receptors immobilised to the planar surface of a transducer array which includes an optical chip that is interrogated by an imaging interferometer, for detection and readout of Surface Plasmon Resonance (SPR), and fluorescence (for labelled assays). Readout is via a CMOS or similar solid state imaging detector such as a CCD. The surface of the optical chip contains microelectrodes for electrochemical detection, readout and transduction of binding to the molecular receptors. The optical system also forms the basis of an UV-NIR imaging Fourier spectrometer for mineralogy studies, sharing the same detector and readout electronics. The system presents a planar surface to which a spatially- resolved array of different molecular receptors (MIPs and antibodies) would be immobilized. Approximately 100 array elements are accommodated on a platform with an area of a few cm², enabling many molecular targets to be simultaneously measured within a given sample. The imaging system eliminates complex interconnections required for high-density electrochemical transduction sensor arrays. Binding of biomarkers to receptors will be readout via i) refractive index changes caused by the presence of bound analytes via SPR, ii) fluorescence, using fluorescently-labelled markers, and iii) electrochemical readout via impedance measurements.

The interferometer is a proprietary design of Cambridge Consultants and is shown schematically in Figure 40. Light from a source is divided into measurement and reference beams via reflection from the front and rear face of the beam splitter. These beams enter the prism and are reflected from adjacent regions of its horizontal face. After reflection they pass through adjacent facets of a bi-prism that introduces a small angular shear between the wavefronts, resulting in the formation of a linear fringe field when reference and measurement components recombine. An imaging detector is used to detect the fringe field from which the SPR, fluorescence and spectral images are extracted. The system contains

no moving parts and is intrinsically stable. Since the FE spectrometer can be installed in an adjacent aperture of the interferometer, mass and volume are minimized by adopting dual functionality,

Samples are delivered using flow cell transport. Molecular binding is detected by using the interferometer to form a phase image of the light reflected from the prism planar surface under SPR conditions. The input beam is derived from a collimated, spectrally narrow band source. The planar surface is coated with a ~50nm layer of dielectric medium (i.e. gold) upon which is deposited the binding chemistry. The interface between prism and dielectric is illuminated and viewed at the critical resonant angle, and the phase of the reflected light varies linearly in response to small changes in refractive index at the surface induced by molecular binding to the MIP layer. The binding sites are deposited within the measurement zone of the interferometer, and the phase image obtained by measuring the phase of light reflected from these sites relative to that from an adjacent reference area. Measurement of the spatial phase variation enables molecular binding in an array of sites to be measured.
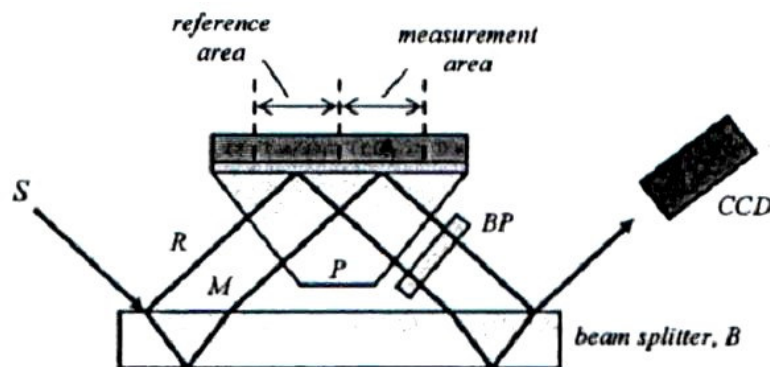
Figure 40: SPR configuration of the interferometer

Molecular samples can be fluorescently tagged or combined with fluorescently tagged tracers as part of the extraction process. Where binding to a receptor occurs, the analyte will be characterized by the presence of fluorescent light emission when molecules are illuminated at the fluorescent excitation wavelength. This technique requires that only the emission of fluorescent light localized to the surface be detected - achievable by either confocal imaging of the surface at the fluorescent wavelength, or evanescent wave excitation of fluorescence in the surface layer. The system may be designed to accommodate either configuration; the emitted fluorescence may be detected by using confocal optics, or the generation of evanescent excitation by illuminating the immobilization surface at the critical angle through the prism. Optical fluorescence is then detected in the beam refracted out of the prism. This approach exploits a generic feature of the optical design and eliminates the need for confocal imaging optics.

The spectral imaging system uses an adjacent section of the interferometer with non-resonant total internal reflection at the planar prism surface. Input optics enables the spectral image of a linear array of pixels to be obtained by transforming each pixel into a linear image slice in the fringe localization plane of the interferometer. The interferogram corresponding to each image slice maps into the corresponding linear section of the 2D fringe field. The spectral distribution of the light at each pixel is derived from the Fourier Transform of the corresponding section of the fringe field. Using optical fibers, the system can be made suitable for remote, multi-channel spectral analysis.

At current stage, the life marker chip has an estimated mass of 1 kg (based on two reaction plates), global dimensions of about 15 x 8 x 9 cm, typical power consumption of about 5 W with 10 W peak, total data load of 37.5 Mbits prior to compression, and typical measurement cycle time of 30 minutes. Similar to the MOA system, the life marker chip needs to be disintegrated and put into different locations of the micro-penetrator. For example, the sensor array can be housed inside forebody and the rest in the aftbody.

IV.4.1.3. Confocal Microscope and Raman Spectrometer (CMaRS)

IV.4.1.3.1. Benefit of Raman spectroscopy

The Raman effect is an inelastic light-scattering process. The Raman spectra can be used to characterize certain classes of bonds as well as to identify structural polymorphs of different organic and inorganic materials. It does, in general, require only minimal or no sample preparation and it can be applied to any optically accessible sample. The commonly used measuring technique in Raman spectroscopy is the point measurement, using in general a microscope setup. Spatial resolution for such measurements can go down to sub micrometer range but usually is in the range of 1 to 3 um. The identification of inorganic, organic, or biological compounds is the main benefit that Raman spectroscopy offers.

The Raman technique is ideally suited for the identification and characterisation of biomolecules such as amino acid. Although the nature of extraterrestrial life, if it exists or has existed in the past, is unknown, there are certain physical and structural constraints that dictate certain aspects of its nature. Most importantly, biomolecules associated with energy transduction require the ability to store electronic energy thereby dictating aspects of their physical molecular structure. The Raman band 200-4000cm^{-1} covers most vibration modes of biomolecules (including CH stretch near 3000cm^{-1}) and those of metal oxides in minerals including manganese oxide of terrestrial rock varnishes with broad Raman features at 590cm^{-1} and 640cm^{-1} that are characteristic biotic activity [Israel *et al*, 1997].

IV.4.1.3.2. Configuration of CMaRS

As shown in Figure 41, CmaRS (mass <1 kg) has small probe head (< 100 cm^3) containing the confocal microscope and Raman filters, fiber-coupled to the laser light source and spectrometer housed in an electronics bay. The confocal microscope (imaging at video rates of 30 frames per second) comprises a Silicon micro-electro-mechanical (MEMS) bi-axial scanning mirror, precision molded aspheric lenses and piezoelectric focus control. The light source for both components is an 852 nm distributed Bragg reflector diode laser. Rayleigh scattered light is detected to form the confocal image, while Raman shifted light is separated by a Raman filter set and detected with a dispersive CCD based compact spectrometer. Spectral resolution is 8 cm over a range from 400 cm to 1800 cm. Raman spectra may be obtained over a variable field-of-view by controlling scanning in the microscope, from a minimum spot size of 1 mm to full field of 250 mm $\times$ 250 μm . The 852 nm spectrum here was obtained while scanning a field measuring 60 μm $\times$ 100 μm with incident power of 20 mW for duration of 300 seconds and a total energy dose of 6 Joules.
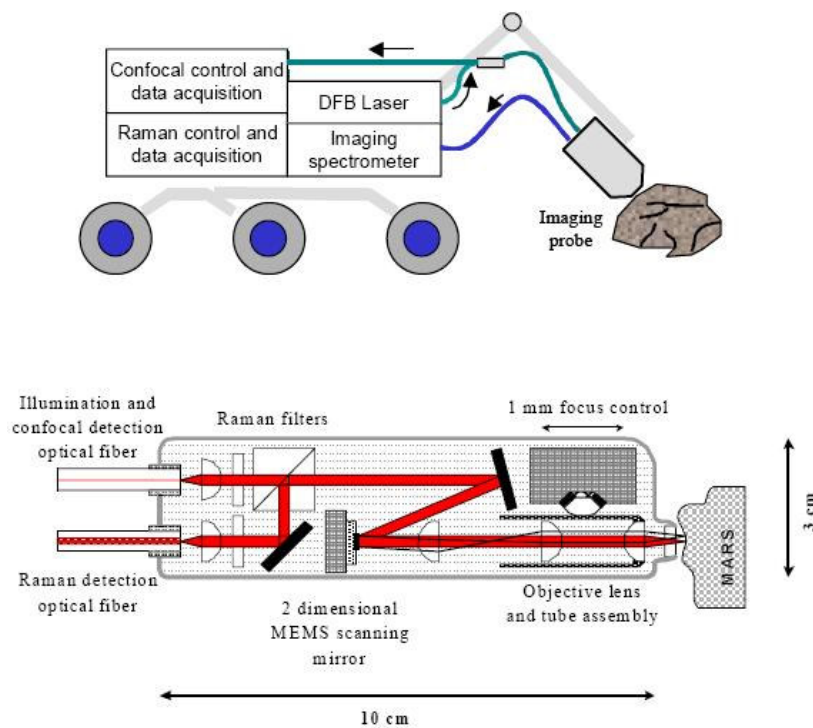
Figure 41: Miniature CMaRS

The great advantage of Raman is the disintegration between the sensor head and Raman filters at one end of the fibre optic and the transmitter/detector and associated optics and electronics at the other. The instrument can be accommodated inside the aftbody with the sensor head integrated into the

drilling mechanism such as the drill bit or alternatively the sample chamber. In general, it is desirable to employ a movable scanning mirror to move the Raman laser beam over the sample site.

IV.4.2. Broadband seismometer

Probably the best-matched science experiment to the penetrator is a passive seismic system. The subsurface emplacement allows a very good, low noise, seismic coupling of the sensors to the planetary bodies crustal material and the multiple-penetrator possible in a single mission permits the establishment of a seismic network. Surface landers are poor platforms for seismic measurements. A single broadband three-component seismometer could determine much about the stratification for an spherically symmetric body from a single large seismic event. As pointed out in Section VIII.1, asteroids are far from spherically symmetric. Hence, it is essential to emplace at least three, and optimally five, appropriately sited seismometers in order to simultaneously determine the time of origin of the event, its location (including depth of the epicentre) and the velocity structure between the source and the detector. With such a network it should also be possible to map the distribution of seismic sources and hence to locate tectonically active zones of the asteroid, to deduce a great deal about the asteroid structure, thermal profile and structural asymmetries. In short, it should be possible to do at least as much in a seismic survey of asteroids using penetrator emplaced seismometers, as has been possible on the Moon using the seismic network established during the Apollo programme. This presupposes the availability of three axis instruments of adequate sensitivity compatible with penetrator emplacement.

Seismic surveying provides time/distance cross-sections of the subsurface with depth. The velocity of seismic compression wave propagation in a material is given by:

$$v = \sqrt{\frac{K + 4/3G}{\rho}}$$

<div align="right">

Equation 2

</div>

where K=bulk modulus of material, G=shear modulus of material, and ρ=material bulk density.

This is also dependent of the porosity (and so water content) of the soil/rock:

$$\frac{1}{v} = \frac{n}{v_w} + \frac{(1-n)}{v_m}$$

<div align="right">

Equation 3

</div>

where n=porosity, v_w=propagation velocity of compression wave in water, and v_m=propagation velocity of compression wave in material. The velocity of compression wave propagation increases with increased water content. The seismic compression wave amplitude undergoes dissipation as it propagates to a depth x which is given by:

$$A = A_0 e^{-\alpha(f)x}$$

<div align="right">Equation 4</div>

where A_0=compression wave peak amplitude, $\alpha(f) = \dfrac{w/2}{Qv}$ =frequency-dependent attenuation coefficient, Q=frequency-independent attenuation coefficient, and $w=2\pi f$. High Q indicates low attenuation, e.g. the value of Q varies from 25-50 for sandstone to 70-150 for basalt/granite.

There are two types of seismology – reflection and refraction seismology. Reflection seismology involves measuring signals reflected from seismic boundaries (exhibited by high acoustic impedance differences related to density) as far as 6 km deep for local surveys. Seismic energy sources cause elastic disturbances to propagate through the Earth with interfaces between geological strata reflecting spreading wavefronts. Arrival times of singly reflected echoes at the surface receivers allow determination of depth and inclinations of reflecting interfaces at known velocities. Seismic data can be complicated due to multiple reflectors, such as sub-surface fractures, which essentially corrupt the data. Received signals are typically ~1-100 Hz frequencies with amplitudes ~10 dB. Distances to the subsurface reflectors are computed from observed travel times and known velocities. The wave velocity increases with depth generating depth-reflection time-distance curves with hyperbolic characteristics forming the basis of velocity-time relationships. The central signal processing techniques utilised include demultiplexing the signals and applying predictive deconvolution by digital Wiener filtering. For deep seismology, account must be taken of the variation in P and S wave velocities with temperature and pressure that can vary by 1% per 100 K temperature change. Reflection seismology is not suitable for local planet exploration, as it requires wide separations between multiple detectors unless these are deployed separately. Networks increase the sensitivity of seismometers and their area of coverage, e.g. Apollo Lunar Surface Experiment Package (ALSEP) network of four seismometer stations deployed by Apollo 12, 14, 15 and 16. Performance is critically dependent on a noise level that is more important then a real coverage. A network of four low-noise seismic stations can detect as much as 60% of global seismic events to a depth of 500-1000 km. A full geophysical network would require 20+ lander seismic stations.

Refraction seismology is based on the fact that seismic waves propagate with the speed of sound in rock depending on rock composition. Seismic waves have different velocities in different types of soil/rock and waves are refracted where they pass between boundaries between different types of soil/rock. If the spacing between the seismic waves and the seismometer is less than d, the depth D of the boundary between two strata is

$$D = \frac{d}{2}\sqrt{\frac{v_2 - v_1}{v_2 + v_1}}$$

Equation 5

Seismic vibrations in rock can build up 3D surveys of the sub-surface. Broadband accelerometers are better than geophones as detectors as they record a broad range of frequencies required in 3D reconstruction and can achieve resolutions ~2-20m. However, this technique requires multiple accelerometers connected by cable. Seismometer placement to ~1 cm depth would avoid surface disturbances from wind and dust storms and provide tether coupling to the bedrock/compact regolith - the Viking 2 seismometer results were contaminated by wind-induced vibrations rendering it near useless (the Viking 1 seismometer failed to deploy). Seismometers must thus be decoupled from the lander and protected from wind and thermal variations. This is not a problem for deployment within penetrators.

The lack of plate tectonics on other planets will yield much lower seismic activity than on Earth, e.g. Mars is generally reckoned to be a one-plate planet with a thick 150 km thick crust undergoing bulk thermo-elastic cooling. This suggests that there should be no more than 10 seismic events per year of moment crustal greater than 10^{16} Nm and no more than 250 seismic events per year of moment greater than 10^{14} Nm [Lognonne et al 1998]. However, there may be some regional tectonic activity associated with the Tharsis bulge that is extensively faulted and may be associated with a mantle plume. Seismometers can detect quakes to determine tectonic activity, local crust data and the incidence of meteoritic activity. Seismometer networks can determine bulk planetary properties and detect seismic discontinuities diagnostic of physical and chemical transitions. Active seismology (through the use of explosives or massive vibration pads) can obtain high resolution and high penetrations for local seismic data, but they are not accurate for shallow prospecting. They cannot generally be employed for planetary missions limiting such missions to low-frequency waves of limited resolution. The most effective means for maximising the quality of the seismic data is to deploy seismometers into boreholes, which the penetrators do.

A broadband three-component seismometer - similar to ALSEP seismometers but of much lower mass - was included on each of the two Mars 96 penetrators to detect natural oscillations in the frequency range 10-100 Hz. It had a mass of 0.3 kg with a power consumption of 0.02 W and a data rate requirement of 10 kbit per event. It used shared electronics and batteries (mass of 0.365 kg) with the accompanying magnetometer. The Mars 96 mission unfortunately failed its orbit insertion into a Mars intercept trajectory.

A more compact broadband seismometer based on MEMS technology is to be flown in each of the four Mars NetLander missions. The Netlander mission will deliver seismometers to a number of well-spaced sites on the planet's surface. By monitoring the arrival of seismic waves at the different sites, a model of

the interior structure of the planet may be deduced. This seismometer, which is being developed by the Microdevices Laboratory of JPL and Imperial College (http://www.ee.ic.ac.uk/optical/Sensors.htm), is designed to meet the constraints of extraterrestrial applications, in particular having very low mass, volume and power requirements (~0.2 kg, 2 x 2 x 3 cm, and 0.1 W, respectively, for a 3-axis sensor in Figure 42), while delivering performance comparable to that of a conventional terrestrial seismometer ($5x10^{-9}$ m/sec^2/$\sqrt{Hz}$ over a 0.05 to 100 Hz bandwidth). In fact, given that the seismometer is based on MEMS technology, we anticipate that the mass of such a device might reduce to significantly less than the stated 0.2kg from the 2001 reference paper, based on the small dimensions. However, for the purpose of this study, we still assume a mass of 0.2kg. The seismometer design uses a micro-machined mechanical structure consisting of a large proof mass supported by an elastic suspension system. The position of the mass is read by an interdigitated capacitance sensor, and then nulled by an electromagnetic force feedback system. The complete device is fabricated as a multilayer stack, with the mass and suspension being constructed by deep reactive ion etching (DRIE) right through the central wafer. Preliminary prototypes have had high out-of-plane stiffness and low cross-axis sensitivity. The low mass and volume of this seismometer is well suited for use in seismic arrays that are necessary for active seismic profiling. Therefore, we choose this seismometer for the micro-penetrator. It, along with the high intrinsic sensitivity of the instrument and the expected low-noise environment beneath surface, should allow greater depths of penetration than on the Earth for conventional seismic profiling. In addition, this device should provide a high-quality seismic measurement that should be capable of elucidating many of the fundamental questions concerning the subsurface of asteroids.
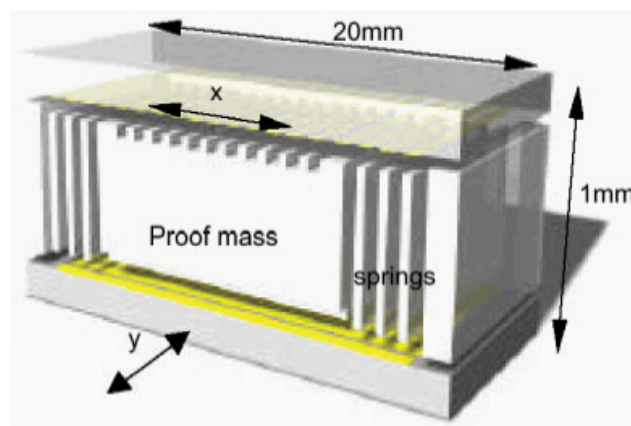
Figure 42: Cutaway geometry drawing of the seismometer by Microdevices Laboratory of JPL

IV.4.3.   Piezoelectric accelerometer

Accelerator data will provide a record of deceleration during the impact event. Double integration of this record with respect to time then provides penetrator position. The deceleration record will be evaluated

to investigate: 1) the depth of penetration (and the placement of the compositional and temperature instruments), 2) the strength properties of the subsurface, and specifically 3) the density and thickness of the mantle.

The most commonly applied device type is the piezoelectric accelerometer, where a small seismic mass is mounted on a piezoelectric ceramic (sometimes called a "crystal" – the earliest piezoelectric instruments, developed by the Curies, used a quartz crystal). Applied accelerations induce longitudinal or shear loads on the ceramic, which develops a proportional charge. This charge divided among the capacitances of the device itself and the cable to which it is attached, can be monitored as voltage, if an ideal charge amplifier is used. An ideal charge amplifier, with no leakage current, would be able to monitor near DC accelerations,. In the real world, the amplifier input current (and/or leakage elsewhere in the system) means the signal is somewhat high-pass filtered, and DC accelerations cannot be detected. This is usually not a problem for impact investigations.

A piezoelectric accelerometer in forebody can measure < 600 g impact deceleration forces to determine rock compressibility and bearing strength by resistance force/time, velocity/time and penetration depth profiles. Impact itself generates a stress wave whose amplitude is determined by the density of the material, impact velocity and sonic wave velocity (e.g. penetration into solid ice requires an impact pressure of 30 MPa). The impact accelerometer (GRUNT) of Mars 96 has a mass of 0.1 kg, a power consumption of 0.1 W, frequency range of 3~100 kHz, force measurement accuracy of 0.25 g, and data capacity of 1.2 kbit during penetration period.

One widely used type (due to its large signal) is ENDEVCO 2271AM20 piezoelectric accelerometer used on the Huygens Surface Science Package (see Figure 43). It is a wide-temperature-range piezoelectric accelerometer designed to measure vibration in cryogenic-temperature applications. The unit is hermetically sealed and is ideal for use in extreme environmental conditions such as outer space. It offers an unusually flat temperature response into a wide temperature range. The accelerometer is a self-generating device that requires no external power source for operation. ENDEVCO 2271AM20 has a mass of 27 g (diameter of 1.6 cm, length of 3 cm), and a range of 100 g that all survivable impacts should be covered.

Figure 43: ENDEVCO 2271AM20 piezoelectric accelerometer

IV.4.4.   Thermometer

Heat flux measurements are of major importance in determining the thermal evolution of the body under investigation. The Mars 96 penetrator carried high range Pt thermocouple thermometers to measure soil temperature with depth in 160-383 K range (accuracy 1 K) in a mass of 0.3 kg, power requirement of 4 W and data rate of 5 kbit/cycle (measure cycle is 5 min). Temperature sensors in the forebody of DS2 Mars microprobe were used to determine the thermal conductivity and thermal diffusivity of soil (with depth) by measuring cooling rate of forebody after impact.

Two thermometers mounted into the forebody and afterbody would allow heat flux measurements to be made. The thermal conductivity of the surface layers give an indication of the particle sizes – 0.02 W/mK indicate particle sizes ~30 μm while larger particles of 100-250 μm would give a thermal conductivity of 0.035-0.05 W/mK. A thermal probe array would have a typical mass of 0.3 kg and a power requirement of 0.8 W.

5.   PENETRATION MODELS

Penetration model may be divided into several categories, and are applied both to predict the penetration of a given vehicle in a specified target, and to infer the target properties from penetration measurements [Lorenz & Ball 1999].

IV.5.1.   Empirical models

The first category is the purely empirical – fits of penetration depth against projectile and target properties. The work of Young [Young 1972, 1997] is widely cited, although since it lacks a sound physical basis and dimensional consistence, is perhaps more distracting than useful for interpreting measurements. Latest Young's empirical equation, also known as the *Sandia equation*, is of the form [Young 1997]

For $V < 61$

$$D = 8 \times 10^{-4} \, SN (\frac{m}{A})^{0.7} \ln(1 + 2.15 \times 10^{-4} V^2) \quad \text{soil, rock \& concrete}$$

$$D = 2.4 \times 10^{-4} \, SN (\frac{m}{A})^{0.6} \ln(1 + 2.15 \times 10^{-4} V^2) \ln(50 + 0.29 m^2) \quad \text{ice \& frozen soil}$$

Equation 6

For $V \geq 61$

$$D = 1.8 \times 10^{-5} \, SN (\frac{m}{A})^{0.7} (V - 30.5) \quad \text{soil, rock \& concrete}$$

$$D = 4.6 \times 10^{-6} \, SN (\frac{m}{A})^{0.6} (V - 30.5) \ln(50 + 0.29 m^2) \quad \text{ice \& frozen soil}$$

Equation 7

where D is the penetration depth in metres, S is the penetrability index (typically 1~5 for hard targets like frozen soil, and 10 or more for loose soil), N is a nose performance coefficient, m is the mass of the penetrator in kg, A is the cross-sectional area in m^2 and V is the impact speed in m/s.

The modifications to Equation 6 and Equation 7 for lightweight penetrators are to multiply an appropriate coefficient K:

For soft targets

$$\text{If } 2 \, \text{kg} \leq m < 27 \, \text{kg} \quad K = 0.27 m^{0.4}$$
$$\text{Else} \quad K = 1$$

Equation 8

For hard targets

$$\text{If } 5 \, \text{kg} \leq m < 182 \, \text{kg} \quad K = 0.46 m^{0.15}$$
$$\text{Else} \quad K = 1$$

Equation 9

All above equations include a nose performance coefficient, N. Originally it was developed based on soil penetration data, and most of the data was from tests at relatively low impact velocity. It was later proven that the same coefficient applies when the target materials are rock, concrete, ice and frozen soil,

and further that there appears to be no velocity dependence. The following equations can be used to calculate N for tangent ogive and conic nose shapes:

For tangent ogive nose

$$N = 0.18L_n / d + 0.56 \qquad \text{not blunted}$$
$$N = 0.9(L_n + L_n^{'}) / d + 0.56 \quad \text{blunted}$$

<div align="right">**Equation 10**</div>

For conic nose

$$N = 0.25L_n / d + 0.56 \qquad \text{not blunted}$$
$$N = 0.125(L_n + L_n^{'}) / d + 0.56 \quad \text{blunted}$$

<div align="right">**Equation 11**</div>

where L_n and $L_n^{'}$ is the original and blunted nose length, respectively, and d is the penetrator diameter.

Give conditions of this asteroid micro-penetrator, the applied *Sandia equation* should be:

$$D = 4.86 \times 10^{-6} \, SN \frac{m^{1.1}}{A^{0.7}} (V - 30.5)$$

<div align="right">**Equation 12**</div>

Some modification has been made to the *Sandia equation* in Equation 12 for DS2 microprobe. The modified penetration model, which is catered for describing low mass penetrators, is described as follows:

$$D = 6.0 \times 10^{-8} \, S^{0.5} \left(\frac{m}{A} \right)^{0.7} V^2$$

<div align="right">**Equation 13**</div>

As mentioned in Section IV.2.1, forebody of the micro-penetrator is designed to have $m = 3.2$ kg, $A = 0.002$ m^2 (diameter of 5 cm) and $N = 0.935$ (using Equation 11). For the expected impact velocity of 130 m/s and for S range of 3~9, the analysis based on Equation 12 indicates that the forebody will be able to penetrate to a depth of 0.3779 to 1.336 m. The analysis based on Equation 13 indicates that the forebody will be able to penetrate to a depth of 0.3072 to 0.5322 m. The actual penetration depths of the micro-penetrator should be determined from the double integration of the accelerometer signals.

IV.5.2. <u>Physical models</u>

The second type of model is purely physical – by making an idealised model of the forces on the penetrator, the dynamic behaviour can be predicted. This type of model is in fact the oldest for which good record exist – the Robins-Euler, Poncelet and Résal equations dating from the 18th and 19th centuries are examples of these, with deceleration being related to a constant term, or a linear combination of a constant term and velocity raised to the first or second power, in the following basic form [Allen *et al* 1957]:

$$-\frac{dv}{dt} = \alpha v^2 + \beta v + \gamma$$

Equation 14

where v is the velocity, t is the time, $-dv/dt$ therefore gives the deceleration magnitude a, and α, β and γ are parameters that may be a function of penetration depth h at time t. The αv^2 is the dynamic resistance, analogous to a hydrodynamic drag force. The β is associated with viscosity and wave propagation in the material. The γ is the static force resisting penetration, a combination of friction between the material and the penetrator and strength of the material. The penetration depth h can be obtained by integrating a twice with respect to time.

The deceleration model in [Anderson *et al* 1996] is one of the easiest to apply, which assume $\beta = 0$:

$$a(t) = \frac{1}{m}\iint\limits_{Sw}(C_d P_d + \sigma_d)(\cos\theta + \mu_f \sin\theta)dS$$

Equation 15

where S_w is the surface in contact with the target material. θ is the angle between the normal to that surface and the direction of motion (see Figure 44). m is the mass of the penetrator. C_d is a stress concentration factor, somewhat like a drag coefficient, but resulting from the dynamic pressure being applied over the surface of the deflected flow and so concentrating a larger force at the surface of the penetrator. A typical value is $C_d = 2$. σ_d is the deviatoric stress component normal to the surface and thus is a measure of its strength - presumably some complex combination of compressive and shear strength that may also depend on the strain rate. μ_f is the coefficient of dynamic friction. P_d is the dynamic pressure given as

$$P_d = \frac{1}{2}\rho v^2(t)\cos^2\theta$$

Equation 16

where ρ is the bulk density of the target material.

During the penetration, three stages have to be considered as shown in Figure 44 (similar to Figure 29). Evaluation of the surface integral in terms of spatial coordinate h along the penetrator symmetry axis ($h = 0$ corresponds to the penetrator tip) is given as follows:

For stage 1, penetrator tip is not fully penetrated, i.e. $h \leq H_1$

$$a(t) = \int_0^h (c_1 v^2 + c_2) h dh$$

i.e. $\alpha = c_1 h^2, \gamma = c_2 h^2$

Equation 17

For stage 2, penetrator tip is fully penetrated but forebody not, i.e. $H_1 < h < L$

$$a(t) = \int_0^{H_1} (c_1 v^2 + c_2) h dh + \int_{H_1}^h c_3 dh$$

i.e. $\alpha = c_1 H_1^2, \gamma = c_2 H_1^2 + c_3 (h - H_1)$

Equation 18

For stage 3, penetrator forebody is fully penetrated, i.e. $L \leq h$

$$a(t) = \int_0^{H_1} (c_1 v^2 + c_2) h dh + \int_{H_1}^L c_3 dh$$

i.e. $\alpha = c_1 H_1^2, \gamma = c_2 H_1^2 + c_3 (L - H_1)$

Equation 19

where $\quad c_1 = \dfrac{2\pi}{m} C_d \dfrac{1}{2} \rho \cos^2 \theta (\cos \theta + \mu_f \sin \theta) \dfrac{\cos \theta}{\sin^2 \theta}, \quad c_2 = \dfrac{2\pi}{m} \sigma_d (\cos \theta + \mu_f \sin \theta) \dfrac{\cos \theta}{\sin^2 \theta} \quad$ and

$c_3 = \dfrac{2\pi}{m} \sigma_d \mu_f \dfrac{d}{2}$.

Values for deceleration $a(t)$, velocity $v(t)$ and penetration depth $h(t)$ can be obtained by solving the three differential equations Equation 17-Equation 19. Assuming $C_d = 2$, $\mu_f = 0.1$, $\sigma_d = 10\sim20$ MPa, $\rho = 1300$ kg/m³, $v_0 = 130$ m/s and given geometry of the penetrator in Section IV.2.1, $m = 3.2$ kg, $\theta = $ arc tan(4), $d = 0.05$ m, $H_1 = 0.05$ m, $L = 0.20$ m; the maximum deceleration magnitude and penetration depth can be approximated to be $a_{max} = 1.2162 \sim 2.3774 \times 10^4$ m/s² and $h_{max} = 0.4964 \sim 0.8433$ m.

Alternatively, a general analytical solution for differential Equation 14 can be used assuming α, β and γ are constants [Allen *et al*, 1957]. This condition applies to the penetration stage 3, where the contact surface does not change any more with increasing depth. Assuming $\beta = 0$ and v_0 is the impact velocity at target surface $s = 0$, we have deceleration $a(t)$, velocity $v(t)$ and penetration depth $h(t)$ as follows:

$$v(t) = \sqrt{\frac{\gamma}{\alpha}} \tan[\tan^{-1}(v_0\sqrt{\frac{\alpha}{\gamma}}) + \frac{1}{v_0}\sqrt{\frac{\gamma}{\alpha}} - t\sqrt{\gamma\alpha}]$$

$$a(t) = \alpha v^2 + \gamma$$

$$h(t) = \frac{1}{2\alpha}[\ln(\alpha v_0^2 + \gamma) - \ln(\alpha v^2 + \gamma)]$$

Equation 20

These analytical solutions can be used to check the accuracy of the numerical code. According to our investigation, the first formula in Equation 20 can only applied to condition when $k\pi - \tan^{-1}(v_0\sqrt{\frac{\alpha}{\gamma}}) < \frac{1}{v_0}\sqrt{\frac{\gamma}{\alpha}} < k\pi$ and k is a positive integer.
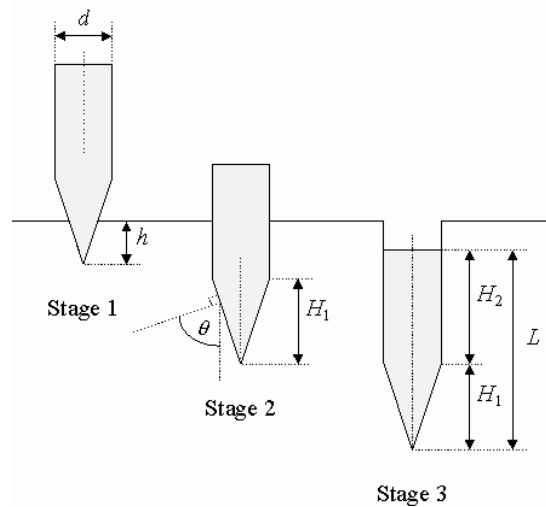
Figure 44: Three stages of penetration

In addition to models based on the deceleration equation (Equation 14), some recent physical models (Yew & Stirbis 1978; Forrestal & Luk 1992) often use a cavity expansion technique to model the forces. They consider axi-symmetric elastic deformation, Mohr-Coulomb failure and plastic deformation of independent discs of target material as the penetrator moves through them, opening a circular void in the material.

IV.5.3.   Numerical models

Beyond the simple algebraic/analytic models of penetration, various levels of numerical sophistication can be applied to penetration models – at one end of the spectrum the SAMPLL code, developed by Young to apply his empirical penetration equations stepwise to layers, is a trivial example. At the other end of the complexity spectrum are full two and three dimensional finite element models and smooth particle hydro-codes (see [Byers et al. 1978]). Even a decade ago, Heuze [Heuze 1989] provided a list of around 50 codes used in impact studies, although many of these were (and remain) restricted in access.
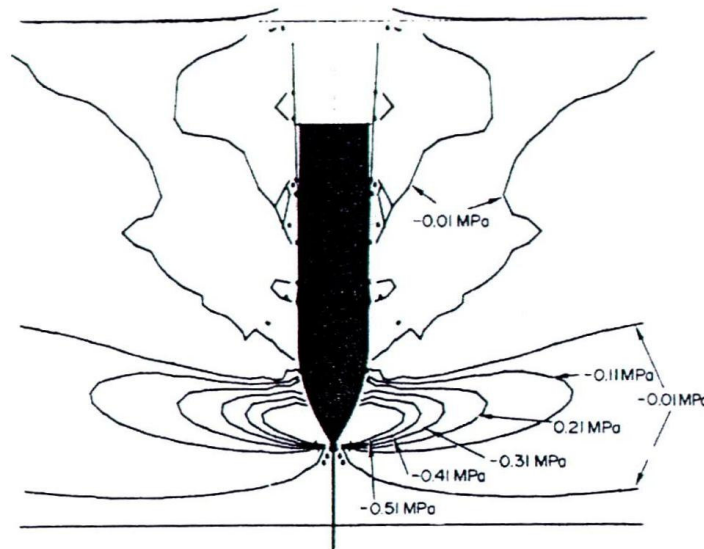
Figure 45: 2D axi-symmetric finite element model

V.   OVERALL SYSTEM-LEVEL DESIGN

1.   PRELIMINARY SYSTEM DESIGN

An Integrated System Model has been developed to assess an initial design of the micro-penetrator released from a parent spacecraft orbiting around the NEO 1996 FG3. First estimates indicate a spacecraft with an all-up mass of ~10 kg including a 10% system level dry mass margin and appropriate sub-system maturity margins.

The Integrated System Model provides an important tool in performing the initial assessment of the penetrator design, and would be evolved in the course of the Study. The System Model is a programme that captures the behaviour of each component part of the system and links them together to ensure that the design at any stage is coherent; i.e. the inputs of one part of the design are the outputs of another. The System Model begins simply and evolves as the understanding of the different parts of the system develops and is available to all of the participants in the project representing the "current state" of the design. It allows the design specialists to work on their part of the system and develop trade-off relationships without having to know whether that is *exactly* the correct design point. The System Model includes mass, power and data budgets. A particularly powerful application is the ability to look at alternative designs by generating parallel versions of the original model and modifying it as appropriate. This ensures that the alternative designs are compared on a "like for like" basis.

There are a number of key drivers for the mission, in particular, instrument and subsystem accommodation, propulsion capability, penetrator guidance and stabilisation, battery sizing for the drill, thermal, structural integrity and communications. As aforementioned in Section IV, the micro-penetrator will carry a biomarker chip, seismometer, accelerometer and thermometer. A small camera (or stereo imager) to provide descent and close-up surface information about the landing site area is not required, as the orbiter is only 3 km above the surface. These instruments provide a "reference payload" for the penetrator with a target mass of less than 10 kg. Until the performance of the overall mission has been determined, it is not easy to determine whether cost or mass will be the critical performance parameter for the penetrator. However, it is clear that the penetrator will be a simple, low cost nano-spacecraft (<10 kg) carried by the primary spacecraft. The penetrator design is particularly influenced by the fact that it must contain a biomimetic drill and biomarker chip, and also a solid motor and be thus stabilised.

2.   FLIGHT DYNAMICS, DEPLOYMENT, TARGETING & AOCS/GNC

The penetrator envisaged is a nano-spacecraft, not too dissimilar to a missile, carried into orbit about the asteroid by the primary spacecraft before release. On-board cold-gas propulsion could first of all separate the penetrator from the primary spacecraft and place it into a controlled orbit about the asteroid (alternatives could include spring loaded ejection). For a 1.5 km diameter asteroid at 3000 m altitude, the orbital velocity is only about 0.2 m/s with an orbital period of about 32 hours. Further on-board

propulsion is used to remove the orbital velocity from the penetrator, where the time for a fall under gravity from a 'standing start' at this altitude is 5.5 hours, and the impact velocity just 0.57 m/s. This is very low and insufficient velocity to impact the asteroid and penetrate the regolith to a desired depth.

A larger difference in relative velocity between the asteroid and penetrator is required, for the penetrator to thus penetrate the regolith to a desired depth. The orbiter is assumed to rendezvous with the NEO from a very gradual orbital insertion using ion propulsion. This means that detachment of the penetrator prior to orbital insertion is not possible to provide an impact DeltaV, as can sometimes be achieved with an impulsive chemical insertion. Therefore some on-board propellant is required to increase the velocity of the penetrator to 136 m/s, which will be sufficient to impact the asteroid and penetrate the regolith to a desired depth of 0.5 m (including a 20% depth margin, i.e. down to 0.6 m). As a relatively high acceleration is required due to the short distance to travel, a small solid motor is envisaged, such as a derivative of the Marc 36A1 by Atlantic Research. As a solid motor is used, some additional propulsion is also required to spin-up and control the penetrator on its trajectory. Active control, rather than spin stabilisation requires too high a thrust for the small propulsion system for control. A penetrator spin of 15.6 rad/s, limits the nutation angle (and hence the deviation from the impact normal) to 5%. After detachment from the main spacecraft, the penetrator is assumed to be pointing in the wrong direction (away from the asteroid), with residual rotation. It is more efficient to correct this first and then spin-up the spacecraft than vice versa. The penetrator solid motor can then be ignited.

Attitude control has initially assumed a low mass (only 65g), 3-axis MEMS Inertial Measurement Unit (IMU) prototype system (inc. MEMS gyros and accelerometers) built by EADS (see Figure 46), with a simple processor (like that on the Canadian picosatellite, CAN X2), and a cold gas (N_2O) reaction control system. The IMU micro-pack demonstrates the performance and the high-density integration possibilities of current state-of-the-art European MOTS (MEMS of the shelves) inertial sensor devices. The inertial measurement unit (IMU) combines 3 orthogonal accelerometers and angular rate sensors and a global temperature sensor. The acceleration sensors (VTI) have a resolution better than 6mg, whilst the gyro (BAe CRS 03) has a measurement range of 100°/s and a resolution of 0.05°/s (10Hz bandwidth).

An additional small propulsion system is required for control, though the amount of additional propellant required for control is low, and the thrust levels required are small. (On the surface a 10kg spacecraft weighs just 2.7mN.) On the SSTL SNAP-1 nano-satellite, nitrous oxide was used as a propellant, with the supercritical fluid using the loading pipe as the propellant store. The SNAP-1 propulsion system is taken as the baseline for this study, however the mission provides an opportunity for the Micro Propulsion Cold Gas Thrusters in development at Uppsala, or other similar systems.

The very fast rate of the descent trajectory (few minutes) means that there is no time for Ground Control to monitor the penetrator and adjust the landing point using the onboard camera for navigation.

Table 7: EADS IMU specifications

Area	Specification:
Technology:	Housing: synthetic / PCB: FR4
Size:	40 x 40 x 65mm^3
Mass:	65g
Power consumption:	2.56W$_{power-up}$ 1.18W$_{typical}$
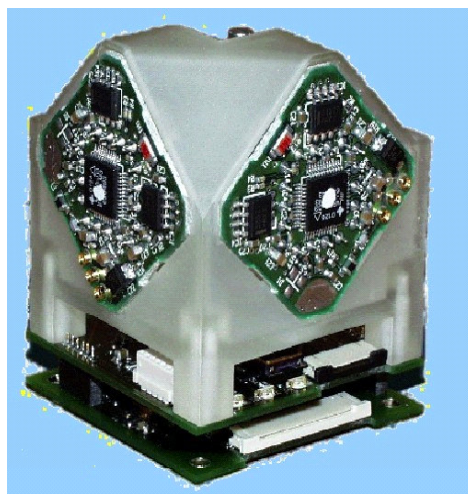
Figure 46: The EADS IMU demonstrator with MEMS technology

3. STRUCTURES & MATERIAL

The penetrator forebody must cope with a very high shock environment upon impact, of about 2400 g. Similarly the aftbody must be robust enough to absorb the shock to avoid damage to the subsystems. The forebody structure is assumed to be a shell composed of Titanium, which has the advantage of having high yield strength, and the ability to deform before buckling, rather than Carbon Fiber-Reinforced Plastics (CFRP) that has a sudden cut-off at buckling. Currently a simple 4mm thick tube is assumed for the outer structure. For extra impact protection at the nose tip, this could be fanned out to be thicker. Detailed assessment of the aftbody structure is more complex and beyond the scope of this study, however a parametric estimate of the structure mass assumes it to be 20% of the overall aftbody mass. Extensive use of crushable Honeycomb is envisaged to be able to cushion the shocks from the impact. Plates with hardware attached, are assumed to be thick enough to avoid buckling through critical bending.

4.   THERMAL & ENVIRONMENTS

Keeping the penetrator functionally compatible with the thermal environment is very important. We initially assume that the penetrator external temperature limits are -20°C to 60°C, although some susbsystems can tolerate temperatures outside this range (e.g. chosen batteries can operate up to 150°C, whilst other alternatives can operate down to -60°C). The orbit of the asteroid provides two extremes at perihelion (hot) and aphelion (cold).

Table 8: The orbit of 1996 FG3 provides two thermal extremes

NEO Name	1996 FG3	
Orbit Apohelion	1.423	AU
Orbit Perihelion	0.6853	AU
Inclination	1.99	Deg
Semi-major axis	1.05415	AU

Also asteroid eclipses can provide cold extremes, where no solar illumination occurs. where the asteroid 'day' is 3.6 hours. In addition, the mother spacecraft may shield out the sun during the pre-release period, where the penetrator is connected to the spacecraft. OSR radiator material is assumed to wrap the penetrator external body, which must keep the penetrator cool enough in sunlight. On the other hand, there must be enough dissipation in eclipse otherwise heaters would be required.

The penetrator experiences four thermal main phases during the mission:

- Pre-release. Here we do not know whether the penetrator will be illuminated or in eclipse, so we must assume both. We assume an electrical and thermal link to the main spacecraft

- Post-release up to moment of impact. Here again we do not know whether the penetrator will be illuminated or in darkness, so we must assume both. Both orbital extremes have been accounted for. No heater power is required, as the penetrator dissipation is high enough in eclipse.

- Immediately after Impact. Some heat will be created due to the impact, however this is beyond the scope of the study

- Post-impact

  o On surface. Here we assume the penetrator aftbody will operate in day and night. There will be some coupling to the asteroid, but this will depend on the amount of insulation used. A quick thermal assessment shows that a small heater is required to maintain the temperature of the aftbody above lower limits. This has a worst case value of 5.3W at aphelion. Detailed assessment of this is beyond the scope of the study

o Underground. Just below the surface, the asteroid temperature not vary too much diurnally and will be approximately the average temperature of the asteroid., because of the relatively rapid spin rate of the asteroid. In order to lose heat, the forebody must be thermally well coupled to the asteroid. This can be achieved through the metal (Titanium) structure. The forebody will therefore be approximately the same temperature as the average asteroid temperature (-17.5°C in aphelion to 94.3°C in perihelion). Therefore heaters are not necessary, however as the forebody is quite hot in perihelion, then some additional thermal blankets would be required for susceptible components. A detailed assessment of this is beyond the scope of the study

Other environments, not studied in detail due to limited scope:

- Charging due to eclipse
- Radiation

5. OPERATIONAL TIMELINE

The total mission duration for the penetrator after release is 8.7 hours. Table 9 shows the operational timeline after release of the penetrator. Pre-release period is TBD, but is expected to be several years. Battery storage life of 4 years is assumed

Table 9: Penetrator Operational timeline

Kill Orbital velocity	308	[sec]
Re-orientation then Spin-up	0.61	[hours]
Time from ignition to impact	19	[sec]
Penetration duration	1	[sec]
Drilling period	7.11	[hours]
Sampling period	1	[hours]
Total Mission Duration	**8.72**	**[hours]**

6. POWER AND ELECTRONICS

The total energy requirement is 137 W-hr. At times the penetrator will be in shadow (the 1996 FG3 asteroid rotates in about 3.6 hours, i.e. ~2 diurnal cycles), and a simple solar array would have to be

backed up by batteries. The penetrator has a configuration that is not well suited to solar arrays, because it is relatively long and thin with limited solar capture area. Therefore a primary LiSOCl2 battery system has been selected as the baseline for simplicity and cost. This is composed of 8 Tadiran TL-6526 batteries in 4 vertical stacks around the central solid motor.

Should an energy requirement have been required that demanded an unfeasibly large primary LiSOCl2 battery system, then body-mounted cells could have been mounted to the penetrator aftbody to at least provide some energy. An unfolding 'umbrella' solar array configuration was suggested, which would protrude out of the back of the aftbody. However this was rejected, as it would have been in the same location as the solid motor system. In any case a primary LiSOCl2 battery system is sufficient as a stand-alone power source.

7.   DATA HANDLING & COMMUNICATION

Due to the short ranges involved, communications between the penetrator and the parent spacecraft can be by a low power, omni directional link. Several miniature communications transceivers have been put together by the microsatellite community by modifying commercial, off the shelf systems, including systems for the SSDL Sapphire, the USU ION-F, and SSTL's SNAP-1 satellites. The USU system is a TEKK-KS960L dual heterodyne transceiver operating at 4550 MHz and a mass less than 0.45 kg. The Can-X2 cubesat has a communications system weighing just 0.1kg. A similar approach would be expected to be effective for the penetrator.

Link budgets for the communications between the penetrator and the parent spacecraft are shown in

Table 10. The link between the spacecraft and the penetrator is a simple, low power UHF system. A 0.6m Medium Gain Antenna on the parent spacecraft is assumed (as with the APIES study). The combination of low data rate and short link distance means that there is a very large margin on the received data.

As the penetrator is not always in view of the mother spacecraft, there will be blackout phases. In additional there is a phasing relationship between the rotation period of the asteroid (3.6 hours) and the orbital period of the asteroid (32.2 hours), which determines whether the penetrator will be in view of the spacecraft when taking measurements. With the current timeline, the penetrator will not quite be in view of the spacecraft, immediately after drilling, and must either wait a short time (~5 minutes) to take measurements before the spacecraft rises above the horizon, or buffer the data, until the spacecraft is in view.

Table 10 Uplink Capabilities of penetrator

	Inter-spacecraft Link	Units
Frequency	0.45	GHz
Transmitter power	0.1	watt
Max Transmission data rate	2×10^4	bps
Antenna gain	0	dB
Line loss	-0.5	dB
EIRP	-10.5	dB
Maximum path length	3.35	km
Space loss	-96.02	dB
Pr/Pol loss	-0.5	dB
Receiver gain	6.43	dB
System noise temperature	1783	K
Receiver G/T	-26.1	dB/K
Eb/No	52.49	dB
C/N Ratio	95.5	
Bit Error Rate	$1_{10}-5$	
Required Eb/No	13.3	dB
Coding	FSK	
Implementation loss	-1.26	dB
Margin	37.93	dB

8.   PENETRATOR BUDGETS

V.8.1.   Mass budget

Refer to Table 11.

Table 11: The Penetrator mass budget requirements

	Mass [kg]	Margin	Budget [kg]	Mass with Margin
Instruments	2.03	10%		**2.2**
Biomarker chip (new version)	1.00	10%	1.10	
Seismometer	0.20	10%	0.22	
Accelerometer	0.03	10%	0.03	
Thermometer	0.30	10%	0.33	
Drilling & Sampling subsystem	0.50	10%	0.55	
Other	0.00	10%	0.00	
Solid Propulsion	1.04	10%		**1.1**
marc 36A1 variant	1.04	10%	1.15	
N2O Propulsion	0.74	8%		**0.8**
Thrusters	0.13	5%	0.13	
Storage pipe	0.12	20%	0.14	
N/c Pyro (1)	0.12	5%	0.13	
Fill & Drain	0.05	5%	0.05	
Pressure Transducer	0.23	5%	0.24	
Armature	0.10	10%	0.11	
Avionics	0.17	14%		**0.2**
EADS MEMS IMU	0.07	20%	0.08	
Processor/OBC	0.10	10%	0.11	
Communications	0.19	20%	0.23	**0.2**
Thermal Heaters	0.01	20%	0.02	**0.0**
Power	1.23	13%		**1.4**
Battery	0.59	10%	0.64	
DC/DC Converters	0.15	5%	0.16	
Harness	0.49	20%	0.59	
Structure & Mechanisms	1.97	20%		**2.4**
Forebody Structure	0.58	20%	0.69	
Aftbody structure	1.39	20%	1.67	
Total Dry Mass	**7.36**	**14%**	**8.37**	**8.4**
Total Dry Mass with Margin		**10%**		**9.2**
Propellant	0.56	24%		**0.7**
Solid Propellant	0.53	20%	0.64	
N2O Propellant	0.03	100%	0.06	
Total Wet Mass	**9.88**		**9.88**	**9.9**

V.8.2. Power budget

Refer to Table 12.

Table 12: The penetrator power requirements

Unit	Power Modes (W)		
	Pre-impact	**Drilling**	**Measuring**
EADS MEMS IMU	2.6	0	0
Processor/OBC	0.3	0.25	0.25
Communications	0.3	0.31	0.31
DC/DC Converters	3.0	2.9	2.7
Prop solenoid valves	10.0	0.0	0.0
Thermal Heaters	0.0	5.3	5.3
Biomarker chip (new version)	0	0	5.0
Seismometer	0	0.1	0.1
Accelerometer	0.0	0	0.0
Thermometer	0	0.8	0.8
Drilling & Sampling subsystem	0	6.0	0.0
Other	0.0	0	0
Totals	**16**	**16**	**14**

V.8.3. Data rate budget

Refer to Table 13.

Table 13: The penetrator data requirements

Unit	Data rate Modes (bps)		
	Pre-impact	Drilling	Measuring
EADS MEMS IMU	20000		
Processor/OBC	0.0		
Communications			
DC/DC Converters			
Prop solenoid valves			
Thermal Heaters			
Biomarker chip (new version)			400.0
Seismometer			0.3
Accelerometer	0.5		
Thermometer		16.7	16.7
Drilling & Sampling subsystem			
Other	0		
Totals	**20000**	**17**	**417**

9.   DISCUSSION ON USING MEMS TECHNOLOGY

In WP3 there was a lengthy discussion about the use of MEMS technology and the benefits that it can offer. For a mass-critical science mission such as this, the potential mass reduction that MEMS can offer is extremely attractive. In our Strawman Penetrator, we already have three MEMS devices in the Biomarker Chip, seismometer and the EADS IMU. However, there are several other possibilities for using MEMS.

For instance, EADS are already developing packaging techniques to integrate sensors and subsystems into Ceramic 3d Microsystems (called 'micropacks', see Figure 47). The size of the micropack will be approximately a mere $20x25x25mm^3$, with power consumption of less than 100mW and of mass just 25g (see Figure 48), and is almost like a small spacecraft in its own right. The micropack consists of 5 ceramic layers, consisting an atmospheric sensor unit, acceleration sensor unit, power supply unit, data handling unit (a Texas Instruments MSP430 micro controller), or a chipsize RF transceiver unit

laminated into the ceramic (an interesting new approach). Each module has a standardized interface, which ultimately combines with other modules to form a system platform. Indeed, several of the current functions in the micropack can meet the needs of the penetrator. For example, a MEMS temperature sensor is integrated into the atmospheric sensor unit. These temperature sensors currently have a measurement range of -40°C to 123.8°C, with a ±0.04°C temperature resolution capability. The S-band transceiver unit meanwhile, certainly has the capability to be used for a mission such as this, where the data rates and the link distance are very low. In fact it is ultimately planned to incorporate the IMU functions of the previous EADS IMU, for greater system integration and miniaturization capability.

Another suggestion is to merge the functions of the scientific and IMU accelerometers (which area already MEMS), or even merge the accelerometer and seismometer functionality, as they are essentially the same device, measuring different frequency ranges.

Finally, MEMS thruster systems could be a mass-efficient alternative to the SSTL N_2O cold gas system, for Secondary Propulsion systems (for control),

As a brief summary, use of these potential MEMS devices and their denser packaging, can lead to substantial savings on the penetrator wet mass.
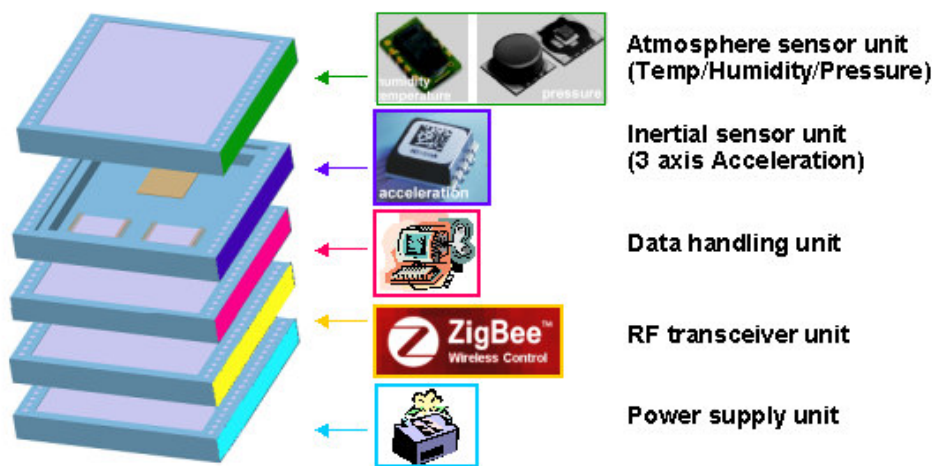
Figure 47: EADS 25g Micropack concept, with MEMS temperature sensors
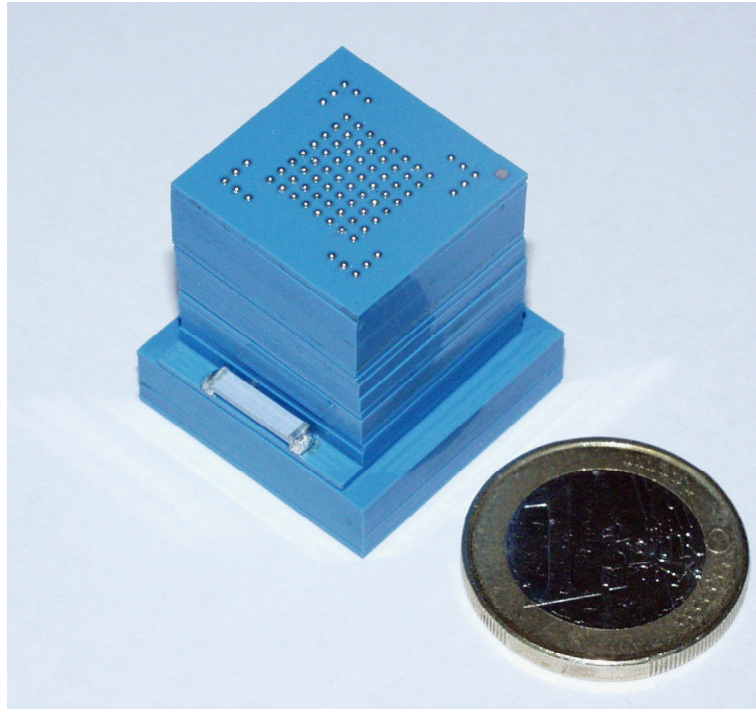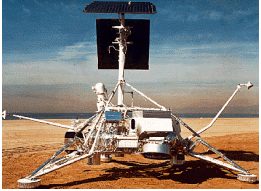
Figure 48: The EADS Micropack next to a 1 Euro coin

VI.   CONCLUSIONS

Drawn inspiration from nature, this case study has proposed a biomimetic drill based on working mechanism of wood wasp ovipositor to sample planetary subsurface material. One of the major limitations of sampling in low gravity environments (such as Mars, asteroids, etc) is the need for high axial force when using conventional drills. The biomimetic drill is designed to address this limitation by applying a novel concept of reciprocating motion. It is lightweight (0.5 kg), driven at low power (3 W), and able to drill deep (1 m). Tests have shown that the reciprocating motion can provide comparable drilling efficiency in terms of power consumption and drilling speed without using external force. Given an asteroid mission scenario, this study has designed the biomimetic drill within a micro-penetrator (overall mass < 10 kg) platform. A complete system design of the micro-penetrator has also been included in this study, which fulfils the design requirement.
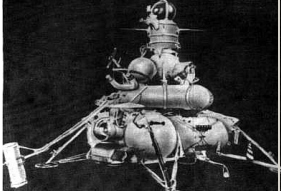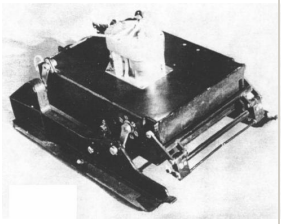
The overall penetration/drilling/sampling system can provide a small, light and energy efficient solution to *in situ* extraterrestrial studies, which is crucial for space engineering. Such a biomimetic drill/micro-penetrator can be used for exploration of terrestrial-type planets or other small bodies of the solar system with the minimum of modifications.

VII. APPENDIX A: SPACE MISSIONS INVOLVING AUTOMATED PENETRATION, DRILLING AND SAMPLING ACTIVITIES

Country	Launch date	Mission/ Lander name	Sample return?	Landing			Penetration, drilling and sampling activities	Sensor suite
				Target	Date	Method		
USA	30/05/66	**Surveyor 1**	No	Moon	02/06/66	Soft (thrusters)	Initial footpad penetrations ranging from 2.1 to 10.5 cm; soil mechanics surface sampler (carried on Surveyors 3,4 & 7) [Ball and Lorenz, 1999]	Stain gauge on each of the three legs, thus force histories recorded for footpad penetration into the lunar regolith; (other sensing devices include TV cameras, etc)
	20/09/66	Surveyor 2			Crashed 23/09/66			
	17/04/67	Surveyor 3			20/04/67			
	14/07/67	Surveyor 4			Radio contract lost 17/07/67			
	08/09/67	Surveyor 5			11/09/67			
	07/11/67	Surveyor 6			10/11/67			
	07/01/68	Surveyor 7			10/01/68			

USSR	12/09/70	**Luna 16**	Yes (101g)	Moon	20/09/70	Soft (thrusters)	Extendable arm with a drilling rig (penetrated 35cm for Luna 16); cylindrical soil sample container [http://nssdc.gsfc.nasa.gov/planetary/lunar/lunarussr.html]	Radiation and temperature monitors
	14/02/72	Luna 20	Yes (30g)		21/02/72			
	14/08/76	Luna 24	Yes (107.1g)		18/08/76			
USSR	19/05/71	Mars 2/ **PROP-M**	No	Mars	27/11/71 Crash landed	Soft (aerobraking, parachute, retro-rockets)	Penetrator hammered into soil gradually [Ball and Lorenz, 1999]	Mechanical properties soil sensors

	28/05/71	Mars 3/PROP-M			02/12/71 Instrument failure after landing		
	05/08/73	Mars 6/ PROP-M			12/03/74 No data returned after landing		
	09/08/73	Mars 7/ PROP-M			Missed planet		
USSR	09/09/78	Venera 11/ **PROP-V**	No	Venus	25/12/78 No data returned	Soft (Aerobraking disc, parachute)	Penetrator consisted of a "rotodynamic punch" deployed into the surface by a spring-loaded arm [Ball and Lorenz, 1999]	Penetrometer to measure electrical resistance of the ground, penetrated depth, the time taken to reach a particular depth; Temperature and pressure sensors; (other sensing devices include camera, spectrometer and seismometer to conduct investigations on the surface)

	14/09/78	Venera 12/ PROP-V			21/12/78 No data returned			
	30/10/81	Venera 13/ PROP-V			01/03/82			
	04/11/81	Venera 14/ PROP-V			05/03/82			
	15/12/84	VeGa 1			11/06/85 No data returned			
	21/12/84	VeGa 2			15/06/85			
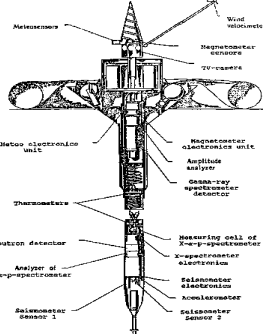
USSR	07/07/88	Phobos 1/ DAS					The DAS Lander has harpoon-like anchor shot into the regolith upon touchdown to reach a depth of 1-10m [Ball and Lorenz, 1999]	Penetrometer with temperature sensors and accelerometer; (other sensing devices include panoramic stereo TV system, seismometer, magnetometer, X-ray fluorescence spectrometer, alpha particle scattering device)
	12/07/88	Phobos2/ **DAS, PROP-F Hopper**	No	Phobos	Contact lost & never deployed	Soft (fall & hold-down thrusters)	PROP-F has a penetrometer	PROP-F's penetrometer to measure ground parameters and a small sample of regolith through tip of the penetrometer; (other sensing devices include a x-ray fluorescence-spectrometer, a dynamometer, a magnetometer, a Gravimeter)

Russian	16/11/96	Mars 96/ **Penetrators** (2) 	No	Mars	Launch failure	Impact penetration (inflatable "airbag" braking device)	Forebody to penetrate 4-6 m into the Martian ground [Surkov & Kremnev, 1998]	Accelerometer to measure penetrator position and mechanical characteristics of the surface rocks; (other sensing devices include TV camera, spectrometers, thermoprobes, seismometer and magnetometer, etc)
USA/ Europe	15/10/97	Cassini/ **Huygens probe** 	No	Titan	14/01/05	Impact penetration (parachute)	Penetration impact to be characterized by accelerometer	Accelerometer (other sensing devices include spectrometers, magnetometer, etc) [Lorenz et al., 1999]
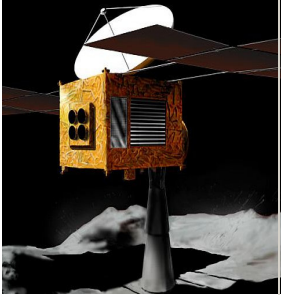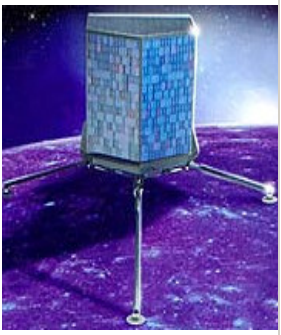
USA	03/01/99	DeepSpace2/ **Mars Microprobes** (2)	No	Mars	03/12/99 Contact lost after landing	Impact penetration (through aeroshell)	Forebody to penetrate 0.3-1 m into the surface; a small drill with an auger and sample collection bit to be pushed into the surrounding soil by two springs and to bring approximately 0.1 g of sample into water sample cup to be examined for the presence of ice	Accelerometers; pressure and temperature sensors [Smrekar et al., 1999]
Europe	02/06/03	Mars Express/**Beagle 2 Lander**	No	Mars	Contact lost	Soft (Airbags)	Cylindrical mole to crawl across the surface and burrow into the ground underneath a rock, to be wound back to deliver the sample to the payload instrument, then to redeployment to obtain further samples.	Accelerometers; thermal sensors; (other sensing devices include spectrometer, etc) [Kochan et al., 1999]
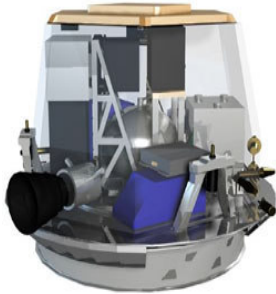
Japan	09/05/03	**Hayabusa (Muses-c)**	Yes (1g)	Asteroid 1998 SF36	2005	Soft (target plate release, fall, hovering & thruster)	To shoot projectile and fragment catcher	Sensing devices include radars, cameras (selected); spectrometer, thermometer, magnetometer (optional) [Kawaguchi et al., 1996]
Europe	02/03/04	Rosetta/ **Philae Lander**	Yes	Comet Churyumov-Gerasimenko	2014	Soft (fall, anchoring & hold-down thruster)	Anchoring harpoon to be fired into the surface; a rotary drill (SD2) to drill more than 20 cm into surface, collects samples and deliver them to different ovens or for microscope inspection	Accelerometer (ANC-M), temperature sensor (ANC-T) (housed in the anchoring projectile) and depth sensor (PEN-M) [Thiel et al. 1999]

USA	12/01/05	Deep Impact/ **Copper Impactor**	No	Comet Tempel 1	~07/2005	Impact Penetration	The impactor to form a crater roughly 25 meters deep and 100 meters wide, ejecting material from the interior of the nucleus into space and vaporizing the impactor and much of the ejecta	Imaging camera, infrared spectrometer [http://deepimpact.jpl.nasa.gov]
Japan	≥2005	Lunar-A/**Penetrators** (2)	No	Moon	≥2005	Impact Penetration (free fall, side-jet)	To penetrate 1~3 m into soil	Accelerometer; (other possible sensing devices include seismometer, heat flow probe, tiltmeter) [Mizutani et al. 1999; http://nssdc.gsfc.nasa.gov/database/MasterCatalog?sc=LUNAR-A]

VIII. APPENDIX B: ABOUT ASTEROIDS

1.   WHAT ARE ASTEROIDS?

Asteroids are rocky and metallic objects that orbit the Sun but are too small to be considered planets. They are known as *minor planets*. On the first day of January 1801, Giuseppe Piazzi discovered an object which he first thought was a new comet. But after its orbit was better determined it was clear that it was not a comet but more like a small planet. Piazzi named it Ceres, after the Sicilian goddess of grain. Three other small bodies were discovered in the next few years (Pallas, Vesta, and Juno). By the end of the 19th century there were several hundred. Several hundred thousand asteroids have been discovered and given provisional designations so far. Thousands more are discovered each year. Asteroids range in size from Ceres, which has a diameter of about 1000 km, down to the size of pebbles. There are undoubtedly hundreds of thousands more that are too small to be seen from the Earth. There are 26 known asteroids larger than 200 km in diameter. Our census of the largest ones is now fairly complete: we probably know 99% of the asteroids larger than 100 km in diameter. Of those in the 10 to 100 km range we have cataloged about half. But we know very few of the smaller ones; there are probably considerably more than a million asteroids in the 1 km range. More likely, asteroids are material that never coalesced into a planet. In fact, if the estimated total mass of all asteroids were gathered into a single object, the object would be less than 1,500 km (932 miles) across - less than half the diameter of our Moon, and its mass is less than that of the Moon.

Asteroids have been found inside Earth's orbit to beyond Saturn's orbit. Between the main concentrations of asteroids in the main belt are relatively empty regions known as the *Kirkwood gaps*. These are regions where an object's orbital period would be a simple fraction of that of Jupiter. An object in such an orbit is very likely to be accelerated by Jupiter into a different orbit. Asteroids can be categorized into three groups by their position in the solar system:

- **Main-Belt Asteroids (MBAs)**: most asteroids are contained within a *main belt* that exists in the warmer inner solar system between the orbits of Mars and Jupiter roughly 2 - 4 AU[4] from the Sun (see Figure 49); further divided into subgroups: Hungarias, Floras, Phocaea, Koronis, Eos, Themis, Cybeles and Hildas (named after the main asteroid in the group).

- **Near-Earth Asteroids (NEAs)**: these asteroids closely approach the Earth (like Hermes had closest approach of 777,000 km), some have orbits that cross Earth's path, and some have even hit the Earth in times past. One of the best-preserved examples is Barringer Meteor Crater near Winslow, Arizona.

---

[4] AU, which stands for "astronomical unit", is a unit for measuring distance. One AU is the average distance from the Sun's center to the Earth's center. It is equal to 149,597,871 km (92,955,807 miles).

- **Trojans**: located near Jupiter's Lagrange points (60 degrees ahead and behind Jupiter in its orbit). Several hundred such asteroids are now known; it is estimated that there may be a thousand or more altogether.
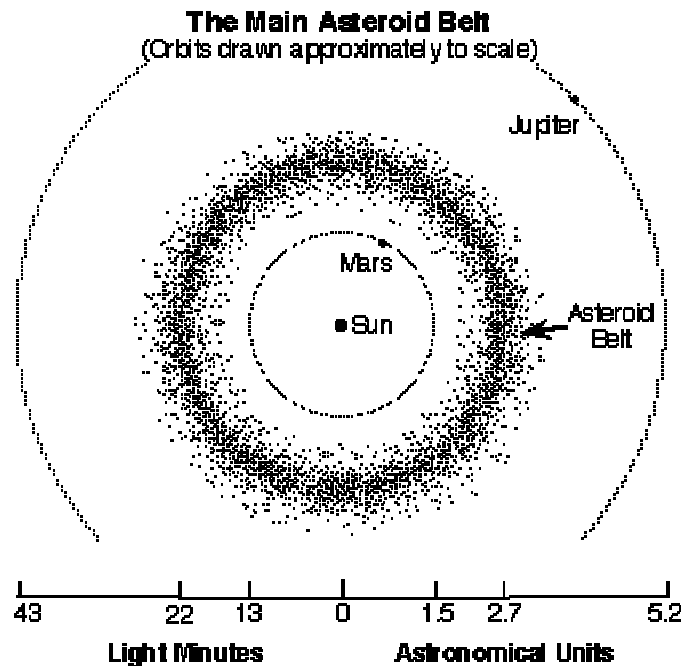
Figure 49: Main asteroid belt

Much of our understanding about asteroids composition comes from examining pieces of space debris that fall to the surface of Earth. Asteroids on a collision course with Earth are called meteoroids. When a meteoroid strikes our atmosphere at high velocity, friction causes this chunk of space matter to incinerate in a streak of light known as a meteor. If the meteoroid does not burn up completely, what's left strikes Earth's surface and is called a meteorite. Of all the meteorites examined, 92.8 percent are composed of silicate (stone), and 5.7 percent are composed of iron and nickel; the rest are a mixture of the three materials. Stony meteorites are the hardest to identify since they look very much like terrestrial rocks.

VIII.1.1. Near earth asteroids (NEAs)

More than a century has passed since the discovery of the first NEA, 433 Eros (see Figure 50), in 13 August 1898. Since then, several thousands of new objects from this population have been detected and new data on their dynamical, physical and mineralogical properties has been collected. From these data

the main differences between NEAs and MBAs can be analyzed. Observable NEAs are rather small objects, usually of the order of a few kilometres or less. MBAs of such sizes are generally not accessible to ground-based observations. Therefore, when NEAs approach the Earth (at distances which can be as small as 0.01~0.02 AU and sometimes less) they give a unique chance to study objects of such small sizes. Some of them possibly represent primordial matter, which has preserved a record of the earliest stages of the solar system evolution, while the majorities are fragments coming from catastrophic collisions that occurred in the asteroid main belt and could provide "a look" at the interior of their much larger parent bodies.

Figure 50: Eros' 6-panel rotation images

VIII.1.1.1. NEA groups & populations

In terms of orbital elements, NEAs are asteroids with perihelion distance *q* less than 1.3 AU. NEAs have been nudged by the gravitational attraction of nearby planets into orbits that allow them to enter the Earth's neighborhood. NEAs are further divided into three groups (Aten, Apollo, Amor) according to their perihelion distance (q), aphelion distance (Q) and their semi-major axes (a) as follows:

Table 14: NEA groups

Group	Description	Definition
NEAs	Near-Earth Asteroids	q<1.3 AU
Atens	Earth-crossing NEAs with semi-major axes smaller than Earth's (named after asteroid 2062 Aten).	a<1.0 AU, Q>0.983 AU
Apollos	Earth-crossing NEAs with semi-major axes larger than Earth's (named after asteroid 1862 Apollo).	a>1.0 AU, q<1.017 AU
Amors	Earth-approaching NEAs with orbits exterior to Earth's but interior to Mars' (named after asteroid 1221 Amor).	a>1.0 AU, 1.017<q<1.3 AU
PHAs	Potentially Hazardous Asteroids: NEAs whose Minimum Orbit Intersection Distance (MOID) with the Earth is 0.05 AU or less and whose absolute magnitude[5] (H) is 22.0 or brighter.	MOID ≤ 0.05 AU, H ≤ 22.0

Potentially Hazardous Asteroids (PHAs) are currently defined based on parameters that measure the asteroid's potential to make threatening close approaches to the Earth. Specifically, all asteroids with an Earth MOID of 0.05 AU or less and an H of 22.0 or less are considered PHAs. In other words, asteroids that can't get any closer to the Earth (*i.e.* MOID) than 0.05 AU (roughly 7,480,000 km or 4,650,000 miles) or are smaller than about 150 m (500 ft) in diameter (i.e. H = 22.0 with assumed albedo[6] of 13%) are not considered PHAs. This ``potential'' to make close Earth approaches does not mean a PHA will impact the Earth. It only means there is a possibility for such a threat. By monitoring these PHAs and updating their orbits as new observations become available, we can better predict the close-approach statistics and thus their Earth-impact threat. By January 2005, there are 655 known PHAs.

The population of NEAs can be approximated by a power law [Rabinowitz, et al 1994], which reflects a general exponential increase of the number of asteroids as we go to smaller sizes:

---

[5] Absolute magnitude is the visual magnitude an observer would record if the asteroid were placed 1 AU away, and 1 AU from the Sun and at a zero phase angle

[6] Albedo: reflectivity of an object; ratio of reflected light to incident light.

$$n(> D) \propto D^{-2} \quad \text{for} \quad D > 0.07\text{km}$$

$$n(> D) \propto D^{-3.5} \quad \text{for} \quad 0.07 > D > 0.01\text{km}$$

Equation 21

where n is the number of asteroids larger than a given diameter D, k is the constant and b is the power law exponent. The estimate of the total number of Earth crossing asteroids (ECAs), i.e. Atens, Apollos and Earth-crossing Amors, gives about 20 asteroids larger than 5 km in diameter, 1500 larger than 1 km and about 135,000 larger than 100 m [Rabinowitz, et al 1994]. The total number of NEAs (not only ECAs) is approximately 1.25 times larger. ECA population consists of 10% of Atens, 65% of Apollos and 25% of Earth crossing Amors [Morrison 1992]. One of the most recent estimates gives an overall number of km-size NEAs of the order of 2000 and more than one million of 100 m sized bodies [Menichella, et al 1996].

VIII.1.1.2. NEA discovery statistics

Discovery completeness of NEAs naturally depends on asteroid absolute magnitude H, hence on diameter and albedo. According to Rabinowitz *et al.* (1994), discovery is thought to be complete up to H = 13.2 mag. In term of size, this means that all NEAs larger than 12 km in the case of low-albedo asteroids (such as C-type), and larger than 6 km for moderate-albedo objects (such as S-type) have been detected. About 35% of NEAs brighter than 15.0 mag (6 km and 3 km in size, respectively) also should have been discovered. But only about 15% of Earth-crossers brighter than 16.0 mag (4 km and 2 km) and only about 7% of objects with diameters of 2 km and 1 km are known today. As it was already mentioned, this is the most critical deficiency to be solved in the framework of the asteroid hazard problem.

The two tables below show the number of NEAs discovered by each of the predominant search programs within a year interval from 1995 through 2003, i.e.

- Lincoln Near-Earth Asteroid Research (LINEAR)

- Near-Earth Asteroid Tracking (NEAT)

- Spacewatch

- Lowell Observatory Near-Earth Object Search (LONEOS)

- Catalina Sky Survey

- Japanese Spaceguard Association (JSGA)

- Asiago DLR Asteroid Survey (ADAS)

Table 15 shows statistics for all NEAs while Table 16 shows statistics for only large NEAs. In this context, "large" is defined as NEAs with H of 18.0 or brighter. This roughly corresponds to 1 km diameter and larger NEAs.

Table 15: NEAs discovered by site

Year	LINEAR (704)	NEAT (566,608,644)	Spacewatch (691,291)	LONEOS (699)	Catalina (703,E12)	Other	Cumulative Total
1995	0	0	26	0	0	6	347
1996	1	10	28	0	0	6	392
1997	17	11	14	0	0	11	445
1998	135	11	36	7	3	13	650
1999	161	0	19	14	30	5	879
2000	258	15	26	38	13	12	1241
2001	277	92	22	42	0	4	1678
2002	286	144	22	21	1	11	2163
2003	235	68	56	54	8	17	2601
2004	202	26	70	39	82	11	3131
2005*	0	0	0	0	1	0	3132

VIII.1.2. Asteroids taxonomic classifications

Asteroids are classified into a number of types according to their spectra (and hence their chemical composition) and albedo. Because of biases involved in the observations (e.g. the dark C-types are harder to see), the percentages below may not be representative of the true distribution of asteroids:

- **C-type**, includes more than 75% of known asteroids: extremely dark; similar to carbonaceous chondrite meteorites; approximately the same chemical composition as the Sun minus hydrogen, helium and other volatiles;

- **S-type**, 17%: relatively bright; metallic nickel-iron mixed with iron- and magnesium-silicates;

- **M-type**, most of the rest: bright; pure nickel-iron;

Table 16: Large NEAs discovered by site

Year	LINEAR (704)	NEAT (566,608,644)	Spacewatch (691,291)	LONEOS (699)	Catalina (703,E12)	Other	Cumulative Total
1995	0	0	7	0	0	3	196
1996	0	4	2	0	0	0	202
1997	3	5	4	0	0	3	217
1998	34	6	3	4	0	5	269
1999	48	0	2	7	8	2	336
2000	78	4	4	8	5	5	440
2001	60	20	0	10	0	1	531
2002	64	22	2	4	0	4	627
2003	40	10	3	10	2	2	694
2004	28	6	1	3	16	2	750
2005[*]	0	0	0	0	1	0	751

- Incomplete half-year (based on discovery data through 03-Jan 2005)

There are also a dozen or so other rare types (see Table 17 for details [Lupishko & Martino 1998]):

Table 17: Spectral types, their features and tentative mineralogical interpretations

Class	Albedo	Brief description	Mineralogy meteorite analogues
P	< 0.06	Very dark and nearly neutral, featureless spectrum (identical to M, E classes), outer main-belt	Organics, anhydrated silicates
D	0.04-0.09	Dark and reddish, spectrum strongly increasing with wavelength, band at 2.2 μm is possible; outer main-belt	Kerogen-like organic material, anhydrated silicates
C	0.04-0.09	Flat-reddish spectrum, weak UV band, may have 3 μm band for hydrated silicates	Phyllo silicates, carbon, organics, CI-CM

			chondrites
B	0.04-0.09	C-subclass, weak UV band, reflectance decreases with wavelength, may have 3 μm band	Hydrated silicates, carbon, chondrites
F	0.04-0.09	C-subclass. weak to nonexistent UV band, may have 3 pm band	The same as B-type
G	0.06-0.01	C-subclass, strong UV band < 0.04 Aim, flat vis-near IR spectrum, bands at 0.6-0.7 and 3.0 μm	Hydrated silicates phyllosilicates, carbon, chondrites
T	0.06-0.10	Broad UV-vis absorption, flat near IR spectrum	(Troilite, metal)
K	Near 0.09	S-like vis. spectrum, weak I μm band, flat reflectance at 1.1-2.5 μm. Eos family	Carbon, CV-CO chondrites, pyroxene
S	0.10-0.30	UV-vis band < 0.7 μm, 1.0 μm (and or no 2.0 μm) band, red slope in vis-near IR, significant spectral variations	Pyroxene, olivine, metal
M	0.12-0.25	Featureless and reddish spectrum, near IR variations, high radar albedo	Fe-Ni metal, enstatite
Q	0.16-0.21	Strong UV band < 0.7 μm, strong absorption (olivine, pyroxene) at 1 μm, no red slope, a rare class	Ordinary chondrites, pyroxene, olivine, Fe-Ni
A	0.17-0.35	Strong UV and 1 μm (olivine) bands, no 2.0 μm band, a rare class	Olivine achondrites, pallasites, olivine
V	0.23-0.40	Strong UV band < 0.7 μm, 1.0 and 2.0 μm bands, weak 1.5 μm feature, a rare class	Basaltic achondrites
R	0.30-0.40	Strong UV band < 0.7 μm, 1.0 and 2.0 μm bands, red slope, a rare class	Pyroxene, olivine-rich achondrites?
E	0.40-0.55	Highest albedo, featureless reddish spectrum, identical to P, M types, weak variability in near IR, inner main-belt	Enstatite achondrites, aubrites, Fe-free pyroxene

By 1998 according to [Lupishko & Martino 1998], only about 68 NEAs have been classified (latest update can be found at http://earn.dlr.de/nea/table1_new.html). Moreover, for 11 of them the classification is still ambiguous. One of the important results of NEA taxonomy, compared with that of MBAs, is a quite different relative abundance of the two most populous classes, C and S. About one half of the classified NEAs belong to the S class, while in the main-belt the low albedos asteroids (C class

and its subclasses, B, F, G) predominate. Available data show that among NEAs the number of S-type objects exceeds that of low albedo types by as much as a factor of 3. By contrast, among the MBAs the ratio is inverse, about 1:5. It is widely suspected that the observed overabundance of S-type objects in the NEA population is a result of observational selection effects. Therefore, one of the main questions of NEA taxonomy is the real ratio of C and S asteroids approaching the Earth. The limiting magnitude of an asteroid, which can be detected by a magnitude-limited survey at given geocentric and heliocentric distances, is a function of its albedo, diameter and solar phase angle. So, three principal factors determining the observational selection effects are responsible for the apparent overabundance of S-type objects among NEAs: albedo, size distribution and larger phase function darkening of C-objects with respect to S ones. Among these factors the first two are dominant.

The most numerous classes observed among NEAs are S. C and V. Five small V-type asteroids (3361, 3551, 3908, 4055 and 5143) in similar near-Earth orbits have reflectance spectra identical to the spectrum of the V-type MBA 4 Vesta [Binzel *et al.,* 1993a]. There are two M-type asteroids (3554 Amun and 6178 1986 DA) and the results of radar observations leave no doubts on their metallic content (Tedesco and Gradie, 1987; Ostro et al. 1991a). This fact seems to be very important from the point of view of possible resources in near-Earth space. There also exist representatives of the high albedo E-type (asteroid 3 103 Eger, which might be a near-Earth parent body of enstatite achondrites and aubrites), of the rather rare A-type (1951 Lick, having the composition probably identical to olivine achondrites or pallasites), and of Q-type (1862 Apollo, 6611 and possibly 1864. 2368, 4688 and 1992 LR [Binzel *et al.,* 1996]), which are believed by some authors to be the parent bodies of ordinary chondrites. The discovery of the very dark (albedo of about 0.03) and reddish D-type 3552 Don Quixote among Amor objects was unexpected because asteroids of this class are mostly located in the outer-belt and in the Trojan clouds and they likely represent the most primitive asteroids in terms of composition. Don Quixote is a rather large object (D = 19 km) and it has an unusually elongated orbit (a = 4.24 AU, e = 0.714).

The variety of taxonomic classes discovered among NEAs indicates that this population is heterogeneous in composition and origin and is continuously mixing through dynamical evolution of the orbits.

VIII.1.3. <u>Asteroids density and porosity</u>

VIII.1.3.1. Bulk density

New data from observations of asteroid mutual perturbation events, optical and radar observations of asteroid satellites, and spacecraft encounters have revolutionized our understanding of asteroid bulk density. Shown in Figure 51 and Table 18 [Britt, et al. 2002] is a summary of some published mass and volume measurements. As shown in Figure 2 in comparison with meteorite grain densities, these density values seem to make mineralogical sense. Because common geologic materials can vary by almost a

factor of four in their grain density, asteroid bulk density measurement need to be interpreted in terms of the object's mineralogy. The differentiated V-type asteroid 4 Vesta has a bulk density consistent with basaltic meteorites overlying an olivine mantle and metal-rich core. The primitive C-type asteroid 1 Ceres has a bulk density similar to primitive CI meteorites (for definitions of meteorite types see [McSween 1999]). However, the smallest of these three asteroids is an order of magnitude more massive than the next well characterized asteroids and these less massive asteroids exhibit some intriguing trends. In general, S type asteroids appear to have higher bulk densities than C-type asteroids, but the range in both groups is large. The M-type asteroid 16 Psyche, which is interpreted to have a mineralogy analogous to iron-nickel meteorites, shows a bulk density in the range of hydrated clays. This indicates either very high porosity or a misidentification of the mineralogy. In the case of 16 Psyche, in addition to spectra and albedo consistent with metal, we have radar albedo data that strongly indicates a largely metallic surface. In Table 18, the best mass and volume determinations together with their respective uncertainties have been employed to determine the given bulk densities and their associated uncertainties. For asteroids for which multiple estimates are provided for either the mass or volume, the best estimate listed in each case has been used to compute the given bulk density. (A few data gaps appear in Table 18 because some values were not available in the published literature. For example, only the bulk densities for 90 Antiope and 762 Pulcova have been published so the corresponding mass estimates are not available and we could not locate a reliable effective diameter for 24 Themis.)

VIII.1.3.2. Bulk porosity

Most asteroids appear to have bulk densities that are well below the grain density of their likely meteorite analogs. This indicates that many asteroids have significant porosity. High porosity attenuates shock propagation, strongly affecting the nature of cratering and greatly lengthening the collisional lifetimes of porous asteroids. Since the grain density of the meteorite analogs gives the density of the asteroid if it was a completely solid object, the deviation of the asteroid's bulk density from this provides an estimate the bulk porosity of the asteroid. The estimated bulk porosities of the asteroids in Figure 51 are shown in Figure 52. Figure 52 highlights the emerging structure of the asteroid belt. First, low-porosity objects are relatively rare. Aside from the three largest asteroids, the only other asteroid with an estimated porosity of less than 15% is 20 Massalia. Most asteroids have significant porosity. There is a cluster of objects around 30% porosity and a scattering of objects on the high end all the way out to 16 Psyche and 22 Kalliope with total porosities of over 70%.

VIII.1.3.3. Macroporosity

The bulk porosity is the sum of all the asteroid's porosity, including the microporosity found in meteorites as well as the large-scale macroporosity. Microporosity probably does not seriously affect the parent asteroid's internal strength since this level of small-scale porosity survives in meteorites that have survived ejection, transportation and delivery to Earth. For insight into the asteroid's internal structure, we need to extract an estimate of the asteroid's macroporosity from its bulk porosity. Subtracting the average meteorite analog microporosity from the bulk porosity of an asteroid provides a rough estimate

of the asteroid's large-scale macroporosity. Shown in Figure 53 are the estimated macroporosities for these asteroids. These data appear to divide into three rough groups:

Table 18: Asteroid bulk density measurements

| Asteroid	Class	Mass (10^{19} kg)	Diameter (km)	Bulk Density (g/cm^3)
1 Ceres	G	94.7	948.8±11.2	2.12±0.04
2 Pallas	B	21.4	532.6±6	2.71±0.11
4 Vesta	V	26.7	529±10	3.44±0.12
10 Hygeia	C	10	407.1±6.8	2.76±1.2
11 Parthenope	S	0.513	153.3±3.1	2.72±0.12
15 Eunomia	S	0.84	255.3±15.0	0.96±0.3
16 Psyche	M	1.73	253.2±4.0	2.0±0.6
20 Massalia	S	0.525	145.5±9.3	3.26±0.6
22 Kalliope	M	-	-	2.5±0.3
24 Themis	C	5.75	-	-
45 Eugenia	F	0.60	214.6±4.2	$1.2\ ^{+0.6}\ _{-0.2}$
87 Sylvia	P	1.51±0.15	260.94±13.3	1.62±0.3
90 Antiope	C	-	120.07±4.0	1.3
121 Hermione	C	0.93	209.0±4.7	1.96±0.34
243 Ida	S	0.0042±0.0006	31.4	2.6±0.5
253 Mathilde	C	0.0103±0.0004	53.02	1.3±0.2
433 Eros	S	0.00067±0.00003	17.36±1.2	2.67±0.03
704 Interamnia	F	7±3	316.6±5.2	4.4±2.1
762 Pulcova	FC	-	137.09±3.2	1.8±0.8
804 Hispania	PC	0.995±0.796	157.3±5.3	4.9±3.9
1999 KW4	-	2.16±0.43 x 10^{-7}	1.2±0.12	2.39±0.9
2000 DP107	C	$4.34\ ^{+1.91}\ _{-0.56}$ x 10^{-8}	0.8±0.15	$1.62\ ^{+1.2}\ _{-0.9}$
2000 UG11	-	$9.35\ ^{+1.87}\ _{-3.74}$ x 10^{-10}	0.23±0.03	$1.47\ ^{+0.6}\ _{-1.3}$
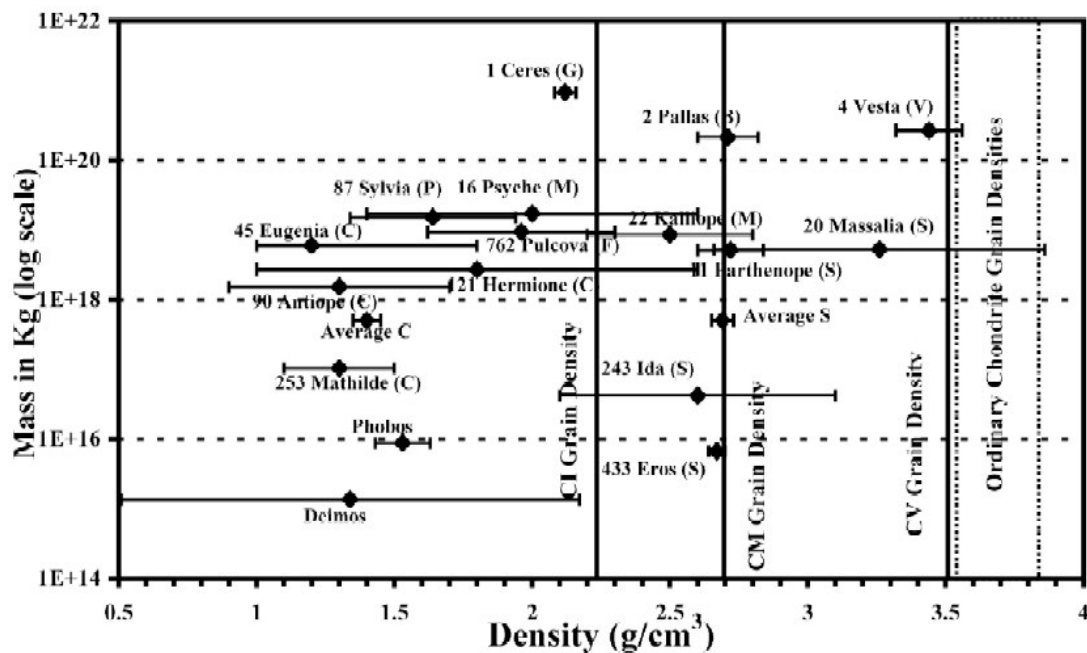
Figure 51: Bulk densities of measured asteroids with the grain densities of common meteorites for comparison (also included in the plot are the asteroid-like moons of Mars, Phobos and Deimos as well as estimates for the average C and S type asteroids)

- The first group includes asteroids that are essentially solid objects, such as the large asteroids 1 Ceres, 2 Pallas, and 4 Vesta, as well as the somewhat smaller 20 Massalia. Their bulk densities are very close to the grain densities of their analog meteorites, indicating essentially zero macroporosity. These asteroids are probably strong, coherent objects that have not been disrupted throughout solar system history. It is interesting that all three asteroids with diameters > 500 km fall in the zero macroporosity group and only one other smaller asteroid has low macroporosity. This probably indicates a very strong size selection process within the asteroid belt for survival as a coherent object and perhaps the relative rarity of coherent smaller asteroids.

- The second group includes asteroids with macroporosities around 20% that are probably heavily fractured, such as the S asteroids 433 Eros and 243 Ida as well as 762 Pulcova and 121 Hermione. These asteroids have between 15 and 25% macroporosity indicating that they have been extensively fractured. Spacecraft images of both 433 Eros and 243 Ida show numerous morphological indications of pervasive fracturing. However, this fracturing was probably not extensive enough to disrupt the object and asteroids with less than approximately 25% macroporosity probably have some measure of coherent strength. In terrestrial geology, well-sorted sedimentary rocks can have up to 30% porosity and still be coherent. However, porosities larger than about 30% usually indicates loose rubble or soils.
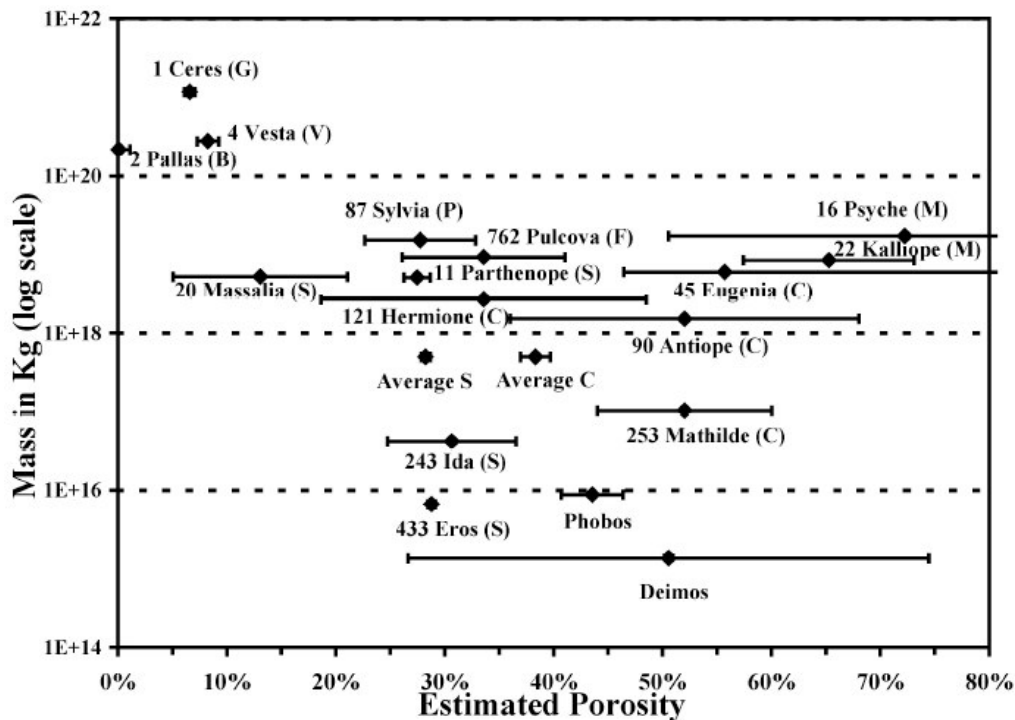
Figure 52: Bulk porosity of measured asteroids

- The third group are asteroids with greater than 30% macroporosity that are loosely consolidated "rubble pile" structures. These objects are probably pervasively fractured and may have been disrupted and reassembled by mutual gravity, some of which have more empty space than solid material. Asteroid 16 Psyche is likely the most porous object observed so far. Its reflectance spectra and radar albedo strongly indicate a metallic surface composition. Assuming an iron meteorite grain density of 7.4 g/cm^3, this would require a bulk porosity of 75%. Iron meteorites have essentially zero microporosity, so the bulk porosity in this case likely equals the macroporosity suggesting a pervasively disrupted object that has been loosely reassembled and held together by mutual gravitation.

In general, the dark, primitive asteroids seem to be more prevalent in the "rubble-pile" group while the high albedo, higher-temperature S-type asteroids seem to be more common in the "fractured" group. The average S-type bulk density falls in the fractured group while the average C-type bulk density is closer to the rubble-pile group. This may indicate that primitive asteroids are fundamentally weaker and more likely to be loosely consolidated, while the metamorphic and igneous asteroids tend to be stronger and more likely to be coherent. However, there are glaring exceptions in each group like the low-porosity P-type 87 Sylvia. Fundamentally, what these data tell us is that the collisional disruption history

of the asteroid belt is complex and probably stochastic, that mineralogy affects, but does not control macroporosity, and that most asteroids have and retain significant porosity.
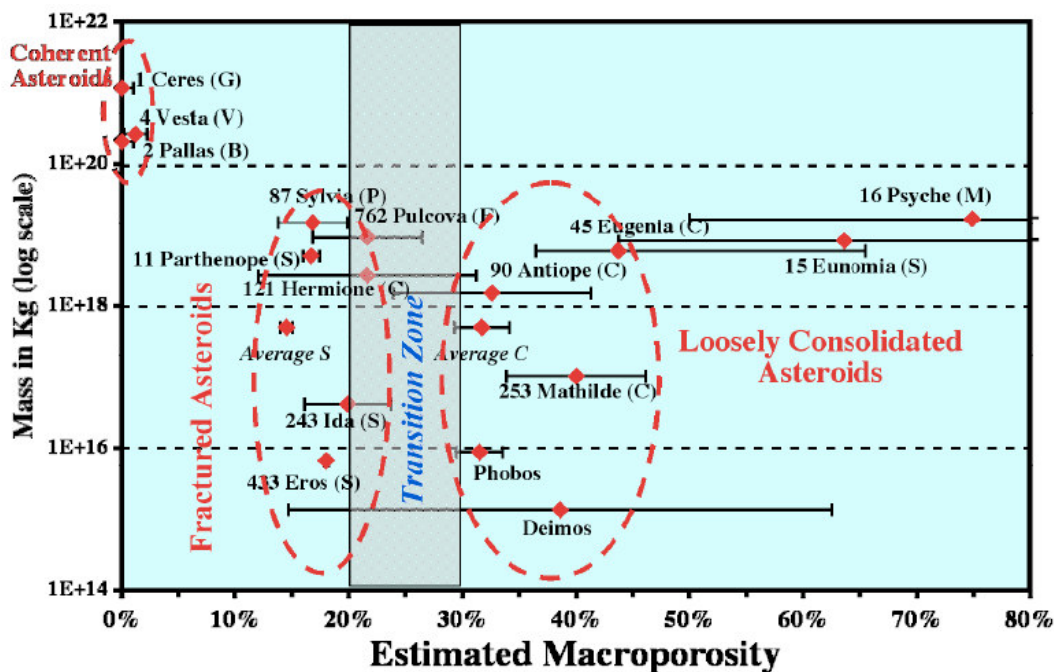

Figure 53: Macroporosity of measured asteroids

2.   WHY TO STUDY ASTEROIDS?

The scientific interest in asteroids is due largely to their status as the remnant debris from the solar system formation process some 4.6 billion years ago. From the point of view of fundamental science, the problems raised by their origin in planet crossing orbits, their life-time, their possible genetic relations with comets and meteorites, etc. are closely connected with the origin and evolution of the solar systems. Today's asteroids are the bits and pieces left over from the initial agglomeration of the inner planets that include Mercury, Venus, Earth, and Mars. If we wish to know the composition of the primordial mixture from which the planets formed, then we must determine the chemical constituents of the leftover debris from this formation process. Moreover, because some of these objects can collide with the Earth, asteroids are also important for having significantly modified the Earth's biosphere in the past. They will continue to do so in the future. Asteroids are the sources of most meteorites that have struck the Earth's surface and many of these meteorites have already been subjected to detailed chemical and physical analyses. If certain asteroids can be identified as the sources for some of the well-studied meteorites, the detailed knowledge of the meteorite's composition and structure will provide important information on the chemical mixture, and conditions from which the Earth formed 4.6 billion years ago. During the

early solar system, the carbon-based molecules and volatile materials that served as the building blocks of life may have been brought to the Earth via asteroid and comet impacts. Thus the study of asteroids is not only important for studying the primordial chemical mixture from which the Earth formed, these objects may hold the key as to how the building blocks of life were delivered to the early Earth.

Secondly, the applied aspects of asteroid studies are becoming more and more evident due to the critical importance they may have for the continuation of civilization. Asteroids are also believed to be potential sources of metals and other raw materials in near Earth space. As is evidenced from meteoritic data, some of the Earth-approaching asteroids contain volatile compounds (hydrogen, nitrogen, carbon, oxygen, organics) over 100 times more abundant than in the most volatile-rich lunar materials. Moreover, observational data suggest that there are pure metallic asteroids. The Sikhote-Alinskij meteorite (found in the far east of Siberia in 1947), consisting of 94% Fe and 6% Ni, is an indirect confirmation of this. Therefore, asteroids may offer a source of volatiles and an extraordinarily rich supply of minerals that can be exploited for the exploration and colonization of our solar system. The asteroids that are potentially the most hazardous are also the objects that could be most easily exploited for raw materials. These raw materials could be used in developing the space structures and in generating the rocket fuel that will be required to explore and colonize our solar system in the twenty-first century. By closely investigating the compositions of asteroids, intelligent choices can be made as to which ones offer the richest supplies of raw materials. It has been estimated that the mineral wealth resident in the belt of asteroids between the orbits of Mars and Jupiter would be equivalent to about 100 billion dollars for every person on Earth today.

Finally, the importance of such a research is related to the asteroid hazard problem. According to the available estimates, there are about 1500 asteroids larger than 1 km diameter and about 135,000 larger than 100 m that cross the Earth's orbit. The main problem is that the orbits of approximately 7% of the Earth-crossers larger than 1 km in diameter (and much less of the smaller ones) are known today. With an average interval of about 100 years, rocky or iron asteroids larger than about 50 m would be expected to reach the Earth's surface and cause local disasters or produce the tidal waves (tsunamis) that can inundate low lying coastal areas. On an average of every few hundred thousand years or so, asteroids larger than a mile could cause global disasters. In this case, the impact debris would spread throughout the Earth's atmosphere so that plant life would suffer from acid rain, partial blocking of sunlight, and from the firestorms resulting from heated impact debris raining back down upon the Earth's surface. The probability of an asteroid striking the Earth and causing serious damage is very remote but the devastating consequences of such an impact suggests we should closely study different types of asteroids to understand their compositions, structures, sizes, and future trajectories.

3. ASTEROID MISSIONS

VIII.3.1. Past missions

Before 1970s the only information obtained on asteroids was though Earth based observations. Several notable asteroids include *Toutatis*, *Castalia*, *Geographos* and *Vesta*. Astronomers studied *Toutatis*, *Geographos* and *Castalia* using Earth-based radar observations during close approaches to the Earth. *Vesta* was observed by the Hubble Space Telescope.

Mars' two tiny captured asteroid moons, *Phobos* and *Deimos*, were the first asteroids seen close up, as part of the exploration of Mars. These moons were best analyzed by the American Viking mission in the 1970s using a telescopic lens. These two moons did not form alongside Mars but were captured by Mars' gravity later in the history of the solar system. Scientists have deduced that both *Phobos* and *Deimos* are closest to the C1 and C2 carbonaceous chondrite classes of materials.

Then on October 1991 asteroid *951 Gaspra* was visited by the Galileo spacecraft and became the first asteroid to have hi-resolution images taken of it. Again on August 1993 Galileo made a close encounter with asteroid *243 Ida*. This was the second asteroid to be visited by spacecraft. Both *Gaspra* and *Ida* are classified as S-type asteroids composed of metal rich silicates and free metal granules.

The Clementine 1 probe by USA is best known for being the probe that successfully mapped the Moon with 4 cameras over the period February through May 1994 and first discovered water at the Moon's poles. What is less known is that Clementine headed off for a rendezvous with near-Earth asteroid *Geographos*, which makes a very close approach to Earth periodically. Unfortunately, Clementine 1 failed en-route to *Geographos*. A software bug in its star tracking navigation system misled the probe to think it was improperly oriented. It went on spending all its fuel in endless reorientation attempts, and by the time mission controllers on the ground were notified, it was out of fuel and could no longer rendezvous with *Geographos*.

On June 27, 1997 the spacecraft Near Earth Asteroid Rendezvous (NEAR) made a high-speed close encounter with asteroid *253 Mathilde*. This encounter gave scientists the first close-up look of a carbon rich C-type asteroid. This visit was unique because NEAR was not designed for flyby encounters. NEAR is an orbiter destined for asteroid *Eros*, which is a large elongated asteroid and is more economically accessible than other large asteroids. NEAR arrived at the asteroid on Valentine's Day in the year 2000, and continued studying the asteroid for approximately a year. In the end, NEAR landed on the asteroid in 2001, even though it was not designed to land. The mission was a resounding success.

Asteroid *9969 Braille* became the target of NASA's Deep Space 1 spacecraft on July 29, 1999 when the spacecraft flew within an estimated 26 km of the asteroid. The spacecraft's infrared sensor confirmed that the small asteroid is similar to *Vesta*, a rare type of asteroid and one of the largest bodies in the main asteroid belt. Apart from flyby findings, project scientists have determined that in about 4,000 years *Braille* will join the hundreds of other asteroids that drift in and out of Earth's orbit.

NASA's Stardust spacecraft successfully completed a close flyby of asteroid *Annefrank* on November 2, 2002. *Annefrank* is typical for asteroids found in the inner asteroid belt, just beyond the orbit of Mars. Stardust's main camera captured images, but the asteroid's relatively small size (8 km across) and the spacecraft's distance (about 3,300 km) resulted that the images were not very detailed.

VIII.3.2. Present missions

On May 9, 2003, the unmanned Muses-C was lifted off by Japanese rocket to make three brief touch-and-go contacts with *1998 SF36*, a tiny asteroid some 290 million km away from Earth. It is the world's first probe designed to bring back samples from the surface of an asteroid, a journey that will take four years and cover nearly 600 million km. It will then bring back a gram or so of the football-shaped asteroid's surface. It will take the 500 kg Muses-C about two years to get there, but the asteroid is among the Earth's closest neighbours.

European Space Agency's comet-chasing satellite Rosetta was successfully placed into orbit on 02 March 2004. It will spend 10 years on a roundabout voyage that will include three velocity-boosting flybys of Earth and one of Mars, as well as plan to flyby two asteroids *2867 Steins* and *21 Lutetia* in 2008 and 2010 respectively. Its final objective in 2014 is to place itself in low orbit around the comet *Churyumov-Gerasimenko*, a 4-kilometer-diameter body that at that point will be 675 million km from the sun. Rosetta will spend six months examining the comet before selecting a landing spot for the small 100-kilogram Philae Lander. Then both Rosetta and Philae will travel with *Churyumov-Gerasimenko* as it moves toward the centre of the solar system. The two spacecraft will have front-row seats as the comet, heated by the sun, sheds its icy outer layer and produces the "tail" for which comets have been held in awe by humans for centuries.

VIII.3.3. Future missions

The Dawn mission to be launched in May 2006, will orbit two asteroids on a single voyage. It will study *Vesta* beginning in July 2010, and *Ceres* beginning in August 2014. *Ceres* and *Vesta* evolved under radically different circumstances in different parts of the solar system more than 4.6 billion years ago. By observing both protoplanets with the same set of instruments, Dawn will provide new insight into the formation and evolution of our solar system.

<u>Near Earth Asteroid Prospector</u> (NEAP) is SpaceDev's first conceived commercial deep-space mission. The mission could be the first deep-space mission defined and executed by a non-governmental entity. NEAP is designed to carry a mix of science, entertainment, engineering and "novelty" payloads as multiple attached and ejectable packages. NEAP could be ready to launch in as little as 3-5 years, choosing from many different potential target objects. When the mission was first conceived in early 1997, only about 400 NEA targets had been discovered. That number is now about 1,000 providing many more options than previously available.

IX.   APPENDIX C: ANALYSIS ON SAWING & MACHINING

1.   NOTATION

F – Friction Force on Tool

N – Normal Force on Tool

Fn – Normal Force on Shear Line

Fs – Force along Shear Line

Fx – Horizontal Force to Remove Chip

Fy – Vertical Force to Remove Chip

R – Resultant Force

Fm – Resultant Momentum Force

β – Angle of Friction

ϕ – Shear Angle

α – Tool Rake Angle

t – Depth of Cut

b – Width of Cut

d – Hole Diameter

s – Feed or Stroke Length

As – Area of Shear Plane

V – Cutting Velocity Parallel to Fx

Vc – Chip Velocity relative to the Tool

Vs – Shear Velocity, i.e. "Chip Velocity" relative to Workpiece

Q – Material Removal Rate

T – Surface Energy of the Substrate Material

2.   ORTHOGONAL CUTTING

Orthogonal cutting is the most widely used model to investigate the cutting process. Figure 54 shows diagrams of the model and assumptions on which this 2-D model is based on include:

- Orthogonal cutting edge of tool is straight & perpendicular to the direction of motion.

- Tool (or workpiece) moves at a uniform velocity V.

- Constant cut depth.

- The shear surface is a plane extending upward from the cutting edge.

- A continuous chip is formed.

- Tool is perfectly sharp & the chip does not flow to either side.

The Aim at this stage is to analyse the cutting process based on the above model to predict the cutting forces, as that will aid in generating the cutting process power consumption and specific cutting energy. Fx and Fy are to be determined experimentally, as in Section II.4. From Figure 54, it follows that:

$$Fs = Fx \cos\phi - Fy \sin\phi$$
$$Fn = Fy \cos\phi + Fx \sin\phi = Fs \tan(\phi + \beta - \alpha)$$

Equation 22

Similarly;

$$F = Fx \sin\alpha + Fy \cos\alpha$$
$$N = Fx \cos\alpha - Fy \sin\alpha$$

Equation 23

Coefficient of friction on the tool face, μ is given by:

$$\mu = \tan\beta$$
$$\mu = \frac{F}{N} = \frac{Fx \sin\alpha + Fy \cos\alpha}{Fx \cos\alpha - Fy \sin\alpha} = \frac{Fy + Fx \tan\alpha}{Fx - Fy \tan\alpha}$$
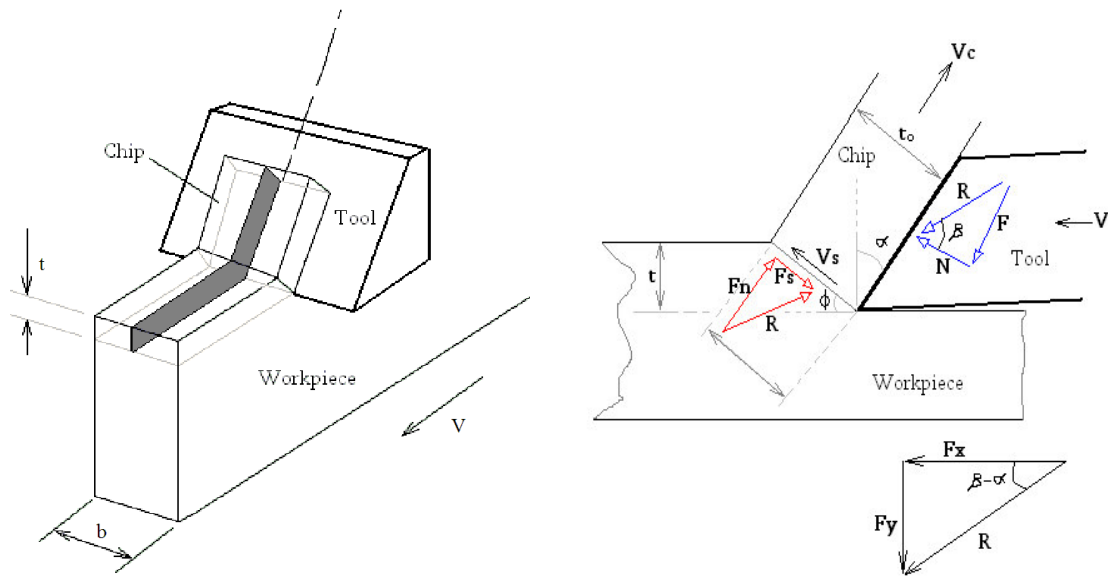
Equation 24

Figure 54: Orthogonal cutting model

3.   MERCHANT HYPOTHESIS

The merchant hypothesis states that, the shear angle adjusts itself such that the work done that is required to remove chip is minimum. From Figure 55, it follows that:

$$Fx = R \cos (\beta - \alpha)$$

$$R = \frac{Fs}{\cos(\phi + \beta - \alpha)}$$

Equation 25

Assuming a chip of unit width & shear yield stress of ζ, then

$$Fs = \zeta . \text{Shear Area (As)} = \frac{\zeta t}{\sin \phi}$$

Equation 26

Inserting Equation 26 into Equation 25 gives:

$$Fs = \frac{\zeta t}{\sin\phi} \frac{\cos(\beta - \alpha)}{\cos(\phi + \beta - \alpha)}$$
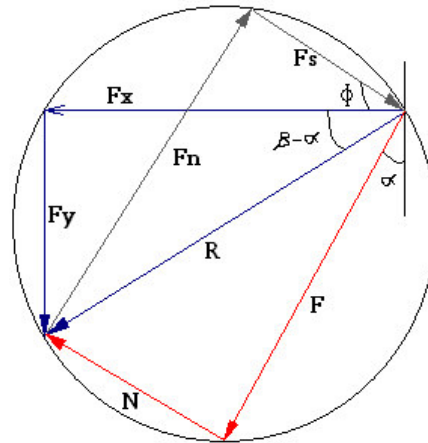
<div align="right">**Equation 27**</div>

Figure 55: Forces diagram

Minimum work done required to remove chip can be obtained by minimizing Equation 27 with respect to ϕ considering that $f(\phi) = \sin\phi \cos(\phi + \beta - \alpha)$. Fx is minimized when $f(\phi)$ is at its maximum, i.e. $\frac{\partial f(\phi)}{\partial \phi} = -\sin\phi \sin(\phi + \beta - \alpha) + \cos\phi \cos(\phi + \beta - \alpha) = 0$. Therefore, we have

$$\phi = \frac{\pi}{4} - \frac{\beta - \alpha}{2}$$

<div align="right">**Equation 28**</div>

4.   SHEAR STRESS

Shear stress components Fs and Fn are crucial as they determine the mean shear & normal stress on the shear plane.

$$\zeta = \frac{Fs}{As} \quad \text{and} \quad As = \frac{b\,t}{\sin\phi}$$

<div align="right">**Equation 29**</div>

Hence:

$$\zeta = \frac{(Fx \cos\phi - Fy \sin\phi) \sin\phi}{b.t}$$

Equation 30

Similarly;

$$\sigma = \frac{Fn}{As} = \frac{(Fy \cos\phi + Fx \sin\phi) \sin\phi}{b.t}$$

Equation 31

5. SHEAR STRAIN

Shear Strain γ is defined as:

$$\gamma = \frac{\Delta S}{\Delta Y}$$

Equation 32

From Figure 56 above:

$$\gamma = \frac{\Delta S}{\Delta Y} = \frac{AB'}{CD} = \frac{AD}{CD} + \frac{DB'}{CD} = \tan(\phi - \alpha) + \cot\phi = \frac{\cos\alpha}{\sin\phi\cos(\phi - \alpha)}$$

Equation 33

6. SHEAR ANGLE

The shear angle can be obtained using Equation 28, once the friction and rake angles are known. Alternatively a more accurate approach is via using the cutting ratio (r), ratio of depth of cut (t) to the chip thickness (tc), both of which can be measured directly:

$$r = \frac{t}{tc} = \frac{AB \sin\phi}{AB\cos(\phi - \alpha)}$$

which gives

$$\tan\phi = \frac{r\cos\alpha}{1 - r\sin\alpha}$$

Equation 34

Knowing the parameters in Equation 34, photomicrography tables can be used to give the shear angle ϕ.
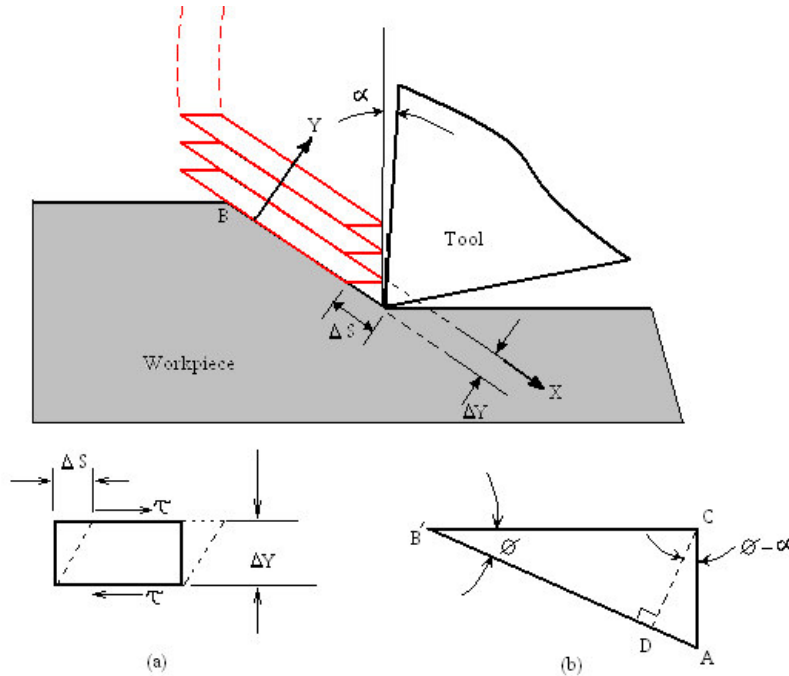

Figure 56: Determination of shear strain: (a) Shear strain in general; (b) Shear strain in cutting
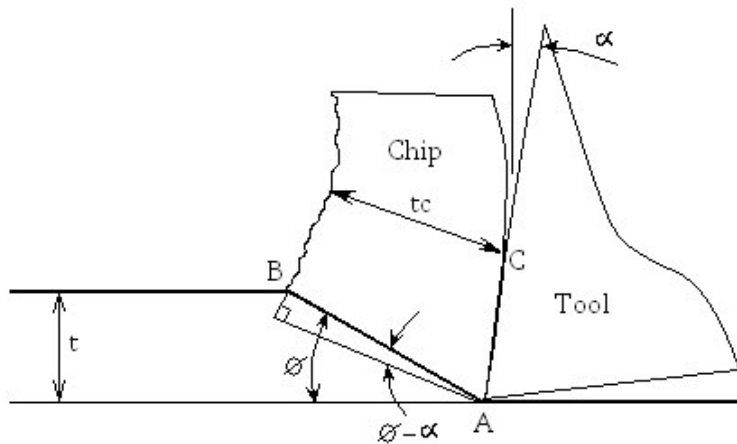

Figure 57: Diagram for deriving relationship between shear angle and cutting ratio

7.   VELOCITY RELATIONS

Figure 58 shows a diagram of the cutting velocities involved in the orthogonal process, where

$$Vc = \frac{\sin\phi \, V}{\cos(\phi - \alpha)} = rV \quad \text{and} \quad Vs = \frac{\cos\phi \, V}{\cos(\phi - \alpha)}$$
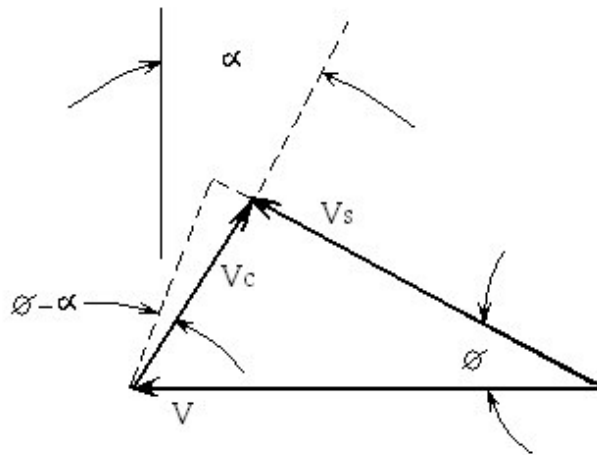
Equation 35

Figure 58: Diagram of cutting velocities

8.   MATERIAL REMOVAL RATE

Material removal rate Q (m^3/sec) is given by:

$$Q = b \, t \, V$$

Equation 36

where b is width of cut, t is depth of cut, and V is cutting speed.

Assuming the drilling hole is approximately 1-m-long and 3-cm-diameter, which gives the total hole volume Vol = π x $(0.03/2)^2$ x 1 = 7.069 x 10^{-4} m^3. Vol/Q therefore gives drilling time. Assuming b = 0.002 m and t = 0.002 m for the drill, average cutting force of 28 N, drilling time for a hole of 7.069 x 10^{-4} m^3 is given in Table 19 at a range of input power from 0.1 W to 5 W. Figure 59 further illustrates the drilling times for different hole dimensions. It's not surprising that big holes take longer time to drill. The time differences decrease as the power goes up.

Table 19: Drilling time based on theoretical calculation

| Power (W)	V (m/s)	Q (m³/s)	Drilling Time (min)
0.1	0.003571429	1.42857E-08	824.6680716
0.2	0.007142857	2.85714E-08	412.3340358
0.4	0.014285714	5.71429E-08	206.1670179
0.6	0.021428571	8.57143E-08	137.4446786
0.8	0.028571429	1.14286E-07	103.0835089
1.0	0.035714286	1.42857E-07	82.46680716
1.4	0.05	0.0000002	58.90486225
1.6	0.057142857	2.28571E-07	51.54175447
1.8	0.064285714	2.57143E-07	45.81489286
2.0	0.071428571	2.85714E-07	41.23340358
2.2	0.078571429	3.14286E-07	37.48491234
2.4	0.085714286	3.42857E-07	34.36116965
2.6	0.092857143	3.71429E-07	31.71800275
2.8	0.1	0.0000004	29.45243113
3.0	0.107142857	4.28571E-07	27.48893572
3.2	0.114285714	4.57143E-07	25.77087724
3.4	0.121428571	4.85714E-07	24.25494328
3.6	0.128571429	5.14286E-07	22.90744643
3.8	0.135714286	5.42857E-07	21.70179136
4.0	0.142857143	5.71429E-07	20.61670179
4.2	0.15	0.0000006	19.63495408
4.4	0.157142857	6.28571E-07	18.74245617
4.6	0.164285714	6.57143E-07	17.92756677
4.8	0.171428571	6.85714E-07	17.18058482
5.0	0.178571429	7.14286E-07	16.49336143
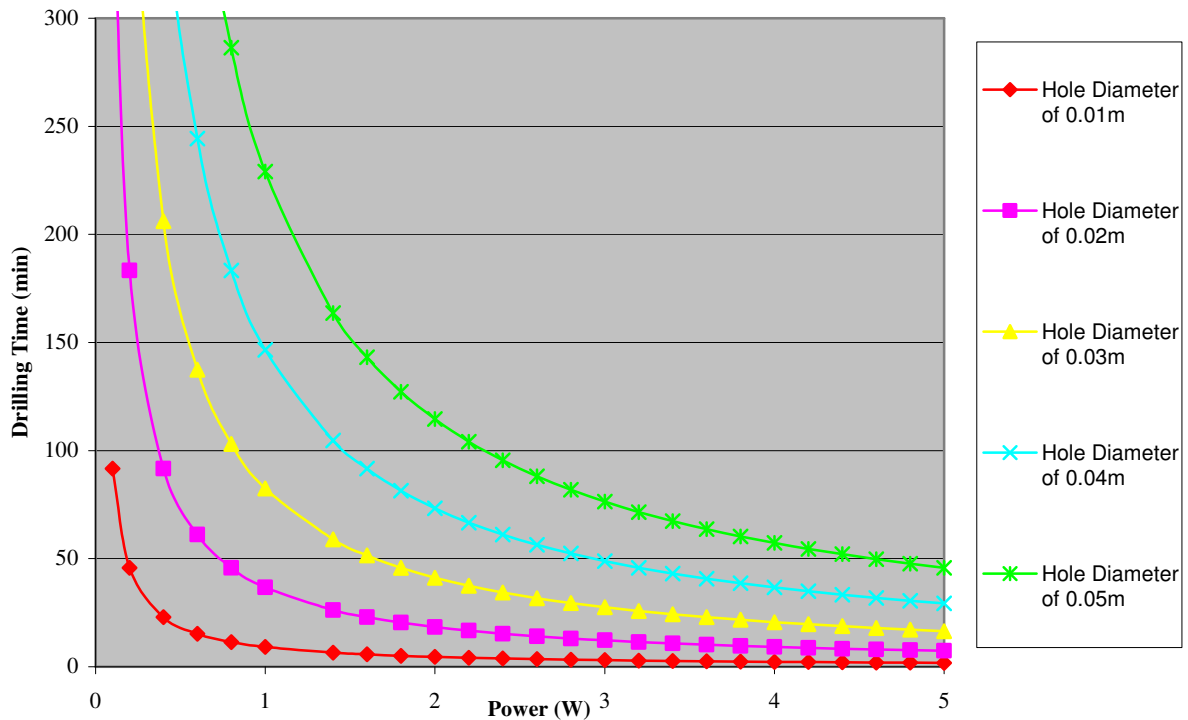
Figure 59: Drilling time versus power based on theoretical calculation

9. ENERGY CONSUMPTION

Total energy consumed per unit time is given by:

$$U = F_x V$$

Equation 37

Total energy per unit Volume of material is given by:

$$u = \frac{U}{V\,b\,t} = \frac{F_x}{b\,t}$$

Equation 38

Total energy per unit volume is consumed in different ways:

1. Shear energy per unit volume (us) on the shear plane.

$$us = \frac{Fs\ Vs}{V\ b\ t} = \zeta\ \frac{Vs}{V\sin\phi}$$

Equation 39

2. Friction energy per unit volume (uf) on tool face.

$$uf = \frac{F\ Vs}{V\ b\ t} \quad or \quad uf = \frac{F\ r}{b\ t}$$

Equation 40

3. Surface energy per unit volume (uA) as new surfaces are formed in cutting.

$$uA = \frac{T\ 2\ V\ b}{V\ b\ t} = \frac{2\ T}{t}$$

Equation 41

where factor of 2 is due to 2 surfaces are generated simultaneously when a cut is made

4. Momentum energy per unit volume (um) due to momentum change associated with the material as it crosses the shear plane.

$$um = \frac{Fm\ Vs}{V\ b\ t}$$

Equation 42

Experimental work by [Merchant, 1945; Piispanen, 1948] has showed the surface energy & momentum energy per unit volume are negligible relative to the other forms of energy. Therefore the total energy per unit volume of substrate material is given by:

$$u = us + uf$$

Equation 43